MECHANISTIC INVESTIGATIONS OF ETHENE DIMERIZATION AND OLIGOMERIZATION CATALYZED BY NICKEL-CONTAINING ZEOTYPES

by

Ravi Joshi

A Dissertation

Submitted to the Faculty of Purdue University

In Partial Fulfillment of the Requirements for the degree of

Doctor of Philosophy

Davidson School of Chemical Engineering

West Lafayette, Indiana

August 2019

THE PURDUE UNIVERSITY GRADUATE SCHOOL
STATEMENT OF COMMITTEE APPROVAL

Dr. Rajamani Gounder, Chair
Davidson School of Chemical Engineering
Dr. Christopher Uyeda
Department of Chemistry
Dr. Fabio H. Ribeiro
Davidson School of Chemical Engineering
Dr. Jeffrey P. Greeley
Davidson School of Chemical Engineering
Dr. Jeffrey T. Miller
Davidson School of Chemical Engineering

Approved by:

Dr. John Morgan
Head of the Graduate Program

To my mother and brother; whose incessant support, love and enormous sacrifices have made this possible

ACKNOWLEDGMENTS

I am privileged to have Raj Gounder as my advisor, mentor and a source of inspiration to do rigorous scientific research. His wisdom, mentorship, and an intense approach to communicating scientific research have shaped me into the scientist, mentor, and communicator that I am today. I will be forever grateful for this experience and will lifelong cherish being a part of his extended family.

I would like to acknowledge Prof. Jeff Miller and Prof. Jeff Greeley for insightful technical discussions and for scientific inputs that have helped my research work. I would like to thank Prof. Fabio Ribeiro and Prof. Tom Degnan and I am deeply grateful for their mentorship, words of wisdom, and for constantly giving me the confidence to succeed.

I would like to thank all the members of Gounder Research Group for their help, support and for making each day at work much more enjoyable, during my time at Purdue. I am fortunate to have the opportunity to build the lab and a strong work-culture with Dr. John Di Iorio and Dr. Michael Cordon and especially thank them, respectively, for providing me a refuge during the polar vortex of 2014, and for teaching me to drive in the US so that I could be the 'designated driver.' I acknowledge Jason Bates, Phil Kester and Juan Carlos Vega-Vila for technical discussions along with Claire Nimlos, Laura Wilcox and Trevor Lardinois for their fun-filled companionship.

Specific acknowledgements have been made at the end of each chapter. Here, I acknowledge my mentee Arunima Saxena for her experimental contributions and for her unceasing stream of technical and scientific questions that have improved me as an experimenter and scientist. I am also thankful to Elizabeth Bickel for adopting me as a mentor and thus helping me learn new things.

I would specifically like to acknowledge Yury Zvinevich for teaching me to build and run experimental apparatus and without whose expertise it would have been impossible to build the lab and keep it running. I acknowledge the mentorship and assistance of Dr. Dhairya Mehta, Dr. Kaiwalya Sabnis, Dr. Harsh Chaudhary, and all other members of the Ribeiro-Delgass group who have helped me throughout my time at Purdue. Specifically, I thank Dr. Anuj Verma for

scintillating technical discussions that got me up to speed in the ‘zeolite world’ and Dr. Jamie Harris for being patient with my far too frequent questions to troubleshoot CO IR.

Finally, I acknowledge the unwavering support of my mother and my brother and I owe them everything that I have been able to achieve. I am also glad to have a support system consisting of my friends, Parul Verma, Sudarshan Ganesh, Abhijit Talpade, Shivani Kshirsagar, Ananya Sheth, Akancha Pandey, and others who have made my Purdue experience memorable. Thank you all.

TABLE OF CONTENTS

LIST OF TABLES

CHAPTER 2

CHAPTER 3

CHAPTER 4

APPENDIX A

LIST OF FIGURES

CHAPTER 2

CHAPTER 3

CHAPTER 4

APPENDIX A

LIST OF SCHEMES

CHAPTER 2

CHAPTER 3

APPENDIX A

ABSTRACT

Author: Joshi, Ravi. PhD
Institution: Purdue University
Degree Received: August 2019
Title: Mechanistic Investigations of Ethene Dimerization and Oligomerization Catalyzed by Nickel-Containing Zeotypes.
Committee Chair: Rajamani Gounder

Dimerization and oligomerization reactions of alkenes are promising catalytic strategies to convert light alkenes, which can be derived from light alkane hydrocarbons (ethane, propane, butane) abundant in shale gas resources, into heavier hydrocarbons used as chemical intermediates and transportation fuels. Nickel cations supported on aluminosilicate zeotypes (zeolites and molecular sieves) selectivity catalyze ethene dimerization over oligomerization given their mechanistic preference for chain termination over chain propagation, relative to other transition metals commonly used for alkene oligomerization and polymerization reactions. Ni-derived sites initiate dimerization catalytic cycles in the absence of external activators or co-catalysts, which are required for most homogeneous Ni complexes and Ni^{2+} cations on metal organic frameworks (MOFs) that operate according to the coordination-insertion mechanism, but are not required for homogeneous Ni complexes that operate according to the metallacycle mechanism. Efforts to probe the mechanistic details of ethene dimerization on Ni-containing zeotypes are further complicated by the presence of residual H^+ sites that form a mixture of 1-butene and 2-butene isomers in parallel acid-catalyzed pathways, as expected for the coordination-insertion mechanism but not for the metallacycle mechanism. As a result, the mechanistic origins of alkene dimerization on Ni cations have been ascribed to both the coordination-insertion and metallacycle-based cycles. Further, different Ni site structures such as exchanged Ni^{2+}, grafted Ni^{2+} and $NiOH^+$ cations are proposed as precursors to the dimerization active sites, based on analysis of kinetic data measured in different kinetic regimes and corrupted by site deactivation, leading to unclear and contradictory proposals of the effect of Ni precursor site structures on dimerization catalysis.

Dimerization of ethene (453 K) was studied on Ni cations exchanged within Beta zeotypes in the absence of externally supplied activators, by suppressing the catalytic contributions of residual H^+ sites via selective pre-poisoning with Li^+ cations and using a zincosilicate support that

contains H^+ sites of weaker acid strength than those on aluminosilicate supports. Isolated Ni^{2+} sites were predominantly present, consistent with a 1:2 Ni^{2+}:Li^+ ion-exchange stoichiometry, CO infrared spectroscopy, diffuse reflectance UV-Visible spectroscopy and *ex-situ* X-ray absorption spectroscopy. Isobutene serves a kinetic marker for alkene isomerization reactions at H^+ sites, which allows distinguishing regimes in which 2-butene isomers formed at Ni sites alone, or from Ni sites and H^+ sites in parallel. 1-butene and 2-butenes formed at Ni sites were not equilibrated and their distribution was invariant with ethene site-time, revealing the primary nature of butene double-bond isomerization at Ni sites as expected from the coordination-insertion mechanism. *In-situ* X-ray absorption spectroscopy showed that the Ni oxidation state was 2+ during dimerization, also consistent with the coordination-insertion mechanism. Moreover, butene site-time yields measured at dilute ethene pressures (<0.4 kPa) increased with time-on-stream (activation transient) during initial reaction times, and this activation transient was eliminated at higher ethene pressures ($\geq$ 0.4 kPa) and while co-feeding H_2. These observations are consistent with the *in-situ* formation of $[Ni(II)\text{-}H]^+$ intermediates involved in the coordination-insertion mechanism, as verified by H/D isotopic scrambling and H_2-D_2 exchange experiments that quantified the number of $[Ni(II)\text{-}H]^+$ intermediates formed.

The prevalence of the coordination-insertion cycles at Ni^{2+} cations provides a framework to interpret the kinetic consequences of the structure of Ni^{2+} sites that are precursors to the dimerization active sites. Beta zeotypes predominantly containing either exchanged Ni^{2+} cations or grafted Ni^{2+} cations show noteworthy differences for ethene dimerization catalysis. The deactivation transients for butene site-time yields on exchanged Ni^{2+} cations indicate two sites are involved in each deactivation event, while those for grafted Ni^{2+} cations indicate involvement of a single site. The site-time yields of butenes extrapolated to initial time, and then further extrapolated to zero ethene site-time, rigorously determined initial ethene dimerization rates (453 K, per Ni) that showed a first-order dependence in ethene pressure (0.05-1 kPa). This kinetic dependence implies the β-agostic $[Ni(II)\text{-ethyl}]^+$ complex to be the most abundant reactive intermediate for the Beta zeolites containing exchanged and grafted Ni^{2+} cations. Further, the apparent first-order dimerization rate constant was two orders of magnitude higher for exchanged Ni^{2+} cations than for grafted Ni^{2+} cations, reflecting differences in ethene adsorption or dimerization transition state free energies at these two types of Ni sites.

The presence of residual H^+ sites on aluminosilicate zeotypes, in addition to the Ni^{2+} sites, causes formation of saturated hydrocarbons and oligomers that are heavier than butenes and those containing odd numbers of carbon atoms. The reaction pathways on Ni^{2+} and H^+ sites are systematically probed on a model Ni-exchanged Beta catalyst that forms a 1:1 composition of these sites *in-situ*. The quantitative determination of apparent deactivation orders for the decay of product space-time yields provides insights into the site origins of the products formed. Further, Delplot analysis systematically identifies the primary and secondary products in the reaction network. This strategy shows linear butene isomers to be primary products formed at Ni^{2+}-derived sites, while isobutene is formed as a secondary product by skeletal isomerization at H^+ sites. In addition, propene is formed as a secondary product, purportedly by cross-metathesis between linear butene isomers and the reactant ethene at Ni^{2+}-derived sites. Also, ethane is a secondary product that forms by hydrogenation of ethene at H^+ sites, with the requisite H_2 generated *in-situ* likely by dehydrogenation and aromatization of ethene at H^+ sites.

The predominance of the coordination-insertion mechanism at Ni^{2+}-derived sites implies kinetic factors influence isomer distributions within the dimer products, providing an opportunity to influence the selectivity toward linear and terminal alkene products of dimerization. In the case of bifunctional materials, reaction pathways on the Ni^{2+} and H^+ sites dictate the interplay between kinetically-controlled product selectivity at Ni sites and thermodynamic preference of product isomers formed at the H^+ sites. In summary, through synthesis of control catalytic materials and rigorous treatment of transient kinetic data, this work presents a detailed mechanistic understanding of the reaction pathways at the Ni^{2+} and H^+ sites, stipulating design parameters that have predictable consequences on the product composition of alkene dimerization and oligomerization.

1. INTRODUCTION

The oligomerization of alkenes is selectively catalyzed by homogeneous organometallic complexes of Ti, Ta, Zr, Cr and Ni [1-5] typically at near ambient temperatures. Among these organometallic complexes, Ni-based complexes favor chain termination over propagation [6], and thus are relatively more selective towards alkene dimerization than oligomerization. Yet, Ni complexes can form trimer and tetramer products by co-dimerization between product and reactant alkenes [7, 8] and at ratios that depend on the ligands coordinated to the Ni center [6, 9, 10]. They are used in industrial processes such as IFP Dimersol [11, 12], Shell Higher Olefins Process [9, 13], and UOP Linear-1 because of their high reactivity and relatively low cost compared to other organometallic complexes [14]. These nickel complexes serve as precursors to the active sites for alkene dimerization or oligomerization and include chelated nickel compounds with a Ni-C bond [15-17], organophosphine nickel compounds [18, 19], and organohalide compounds of nickel(II). In the presence of an alkene, organophosphine Ni compounds readily form Ni-C bonds, chelated nickel compounds form a Ni-hydride or Ni-alkyl by eliminating a ligand group, while organohalide complexes require external metal-alkyl or metal-hydride compounds as an activator to initiate the catalytic cycle [6, 20]. On the other hand, such external activators are not required in the case of heterogeneous catalysts comprising nickel supported on silica-alumina [21-23], zeolites [24-33], mesoporous molecular sieves [34-41] and sulfated alumina [42-44]. These materials selectivity catalyze ethene oligomerization at mild temperatures (<523 K) and at significantly higher rates (per Ni) compared to the acid zeolites (per H^+) (e.g. ZSM-5) [45, 46]. Also, Ni^{2+} cations supported on metal organic frameworks (MOFs) selectively mediate ethene dimerization and oligomerization, however, require external activators such as modified methyl aluminoxane (MMAO) to initiate the catalytic cycle [47].

In the case of heterogeneous Ni catalysts and specifically in the case of Ni-containing zeotypes (zeolites and molecular sieves), a variety of Ni site structures are present. Studies [25, 26, 30, 34] predominantly based on ESR spectroscopy have proposed Ni^+ cations in zeolites to be the active sites, although structures such as Ni^{2+} cations are silent for standard EPR spectroscopy at conventional microwave frequencies employed in these studies [48]. In contrast, Ni^{2+} cations present as charge compensating cations are reported to be the active sites in the case of

aluminosilicate zeolites [31-33, 49]. Ni^{2+} cations grafted at silanol defects are also purported active site structures for Ni-containing siliceous mesoporous supports [50, 51]. In addition, proposed active site structures for ethene dimerization and oligomerization include $NiOH^+$ [41] and a Ni^+-H^+ species [52] supported on aluminosilicate zeolites.

These distinct proposals for Ni active site structures complicate the mechanistic studies on Ni-containing zeotype catalysts. The reaction mechanism for alkene dimerization has remained unclear on heterogeneous nickel cations, even though homogeneous organometallic complexes have been identified to follow either the metallacycle or the coordination-insertion mechanism by experimental [18, 53] and computational studies [54, 55]. In the case of Ni-containing zeotypes, the metallacycle mechanism that involves a redox cycle [3, 6] is mainly proposed for Ni^+ cations [38, 56, 57], while the non-redox coordination-insertion mechanism [6] is proposed for Ni^{2+} cations [33, 58, 59]. Also, Ni sites are expected to form terminal alkenes as products of the metallacycle mechanism [18], while they are expected to form both terminal and internal alkene isomers as products of the coordination-insertion mechanism [2, 6, 53, 60]. Thus, mechanistic debates also arise in part because of residual Brønsted acid (H^+) sites on supports such as aluminosilicates that catalyze double-bond isomerization via other pathways [61-64] to form a mixture of terminal and internal alkene dimers. Accordingly, conflicting proposals suggest the Ni cationic sites produce only the terminal alkene isomers [27, 28, 31, 38, 49, 65], while others [33, 56] suggest they also form internal alkenes. Lastly, the limited understanding on the mechanism stems from the remarkable characteristic of heterogeneous Ni cations on aluminosilicates to catalyze alkene dimerization in absence of external activators, as discussed before [21-41]. Such activators are required in the case of the coordination-insertion mechanism to convert Ni(II) metal centers into the active Ni-hydride or Ni-alkyl species [58], but are not required in the case of the metallacycle mechanism, as Ni cations themselves serve as precursors to the active sites.

This dissertation aims to examine the mechanistic details of reaction pathways occurring at the Ni and H^+ sites during the dimerization and further chain growth (oligomerization) reactions of ethene on Ni-containing zeotype materials. In doing so, it intends to determine the reaction mechanism governing ethene dimerization turnovers at Ni sites by discriminating between the two debated mechanisms (metallacycle and coordination-insertion). The Ni site structures identified by *ex-situ* characterization serve only as the precursors to the dimerization active sites, which are

formed *in-situ* in the presence of ethene and in the absence of an external activator. Catalyst deactivation is observed under the studied reaction conditions (453 K, 0.05-1 kPa ethene) and extrapolation of the product site-time and space-time yields to initial reaction time is required for more accurate normalization by the number of active sites. These initial time product yields do not reflect product formation rates due to consumption in subsequent reactions in the reaction network, and measurement are performed at varying residence times in order to extrapolate to zero residence time to rigorously determine initial ethene dimerization rates. This methodology for measuring reaction rates is underscored throughout this work.

The mechanistic origins of ethene dimerization at Ni sites are probed using Ni-containing Beta zeotype materials in Chapter 2. The catalytic contributions of residual H^+ sites are minimized by selectively exchanging them with spectator Li^+ cations and by using a zincosilicate analog of the Beta topology because it contains residual H^+ sites of weaker acid strength than such sites on aluminosilicates. Control experiments identify isobutene as a kinetic marker for butene double-bond isomerization at H^+ sites and allows discrimination between the isomerization pathways occurring at H^+ and Ni^{2+}-derived sites. The double-bond isomerization of 1-butene to 2-butene isomers occurs via a secondary reaction pathway on H^+ sites and via primary reaction pathways on Ni^{2+} sites. *In-situ* X-ray absorption measurements show the dimerization catalytic cycle to be non-redox in nature, with Ni metal centers present in a +2 oxidation state. In the absence of external activators, the butene site-time yields (453 K) show an induction period that is eliminated by co-feeding H_2 and by increasing ethene pressure, implying the formation of catalytically active $[Ni(II)\text{-}H]^+$ intermediates, which are detected and quantified by H/D scrambling and H_2-D_2 isotopic exchange experiments, respectively. The ethene-assisted activation of exchanged Ni^{2+} cations on Beta zeolites involves *in-situ* formation of H^+ sites, consistent with DFT proposals and as evidenced by trace isobutene formation [59]. Overall, the formation of $[Ni(II)\text{-}H]^+$ intermediates in the absence of external activators, the +2 oxidation state of nickel metal center during catalysis and the prevalence of a primary reaction pathway for the double-bond isomerization of 1-butene at these intermediates provide unambiguous evidence supporting the coordination-insertion mechanism.

Chapter 3 clarifies the kinetic details and the site requirements for the formation of the coordination-insertion active sites from Ni precursor site structures, such as the ion-exchanged

Ni^{2+} cations and the grafted Ni^{2+} sites. The structure of Ni precursor sites as determined by *ex-situ* characterization is unequivocally correlated to reaction kinetics by rigorously determining the initial ethene dimerization rates (per Ni, 453 K). Catalytic differences between the exchanged and grafted Ni^{2+} cations are distinguishable by analyzing the transient deactivation in butene site-time yields (per Ni), where the former exhibits hyperbolic (multi-site) deactivation and the later exhibits exponential (single-site) deactivation. The first order dimerization rate constant (per Ni, 453 K) for ethene is approximately two orders of magnitude higher at exchanged Ni^{2+} cations than at grafted Ni^{2+} cations, reflecting differences in free energies of ethene adsorption or dimerization transition state formation at these sites.

Also, the presence of H^+ sites on Ni-containing aluminosilicate zeotypes favor the formation of branched and higher molecular weight alkene oligomers and is empirically observed to correlate with increased ethene conversion [27, 31]. The reaction pathways in the oligomerization network at the Ni and H^+ sites are deconvoluted and systematically probed in Chapter 4. A Ni-exchanged Beta zeolite sample predominantly containing Ni^{2+} cations and no detectable residual H^+ sites results in generation of one H^+ site per Ni^{2+} cation during the ethene-assisted formation of the coordination-insertion active sites. The quantitative determination of the apparent deactivation order for the product space-time yields shows that propene and linear isomers of butenes are formed at Ni sites, while isobutene and ethane are formed at H^+ sites. Further, Delplot analysis discriminates between the primary and secondary products formed in the reaction network. The linear isomers of butenes are formed as primary products at the coordination-insertion active sites, while isobutene is formed as a secondary product by skeletal isomerization at H^+ sites. Ethane is also a secondary product formed by hydrogenation of ethene at H^+ sites by H_2 that is generated *in-situ* from ethene. Moreover, propene is formed as a secondary product by cross metathesis of ethene and linear isomers of butenes at the Ni^{2+}-derived sites. These findings clarify the site origins and the mechanistic pathways for some of the oligomerization products formed on bifunctional materials containing exchanged Ni^{2+} and H^+ sites.

2. EVIDENCE FOR THE COORDINATION-INSERTION MECHANISM OF ETHENE DIMERIZATION AT NICKEL CATIONS EXCHANGED ONTO BETA MOLECULAR SIEVES

2.1 Introduction

Alkene dimerization is an entry step in oligomerization and chain growth pathways to convert light alkenes into heavier hydrocarbons [5, 46] which provide routes to convert ethene derived from shale gas hydrocarbons (e.g., via ethane steam cracking [66, 67]) into chemicals and liquid fuels. Nickel supported on heterogeneous solids including silica [26, 57] silica-alumina [22, 23] zeolites [27, 30-33] mesoporous materials [34-36, 40] and sulfated alumina [42-44] are reported to catalyze ethene dimerization in the absence of externally supplied activators or co-catalysts. Such catalysts (e.g., Ni-SiO_2 [57], Ni-SBA-15 [38]) have been proposed to operate by the metallacycle mechanism, based on observations that certain homogeneous complexes (e.g., Ni organophosphines [18, 19]) also do not require an external initiator and are able to dimerize alkenes by metallacycle-based cycles. In contrast, when co-catalysts (e.g., modified methyl aluminoxane (MMAO)) are used with other classes of Ni-based heterogeneous solids, such as Ni^{2+} cations supported onto metal organic frameworks (e.g., Ni-MFU-4l [58]), ethene dimerization is reported to be catalyzed by the coordination-insertion mechanism (i.e., Cossee-Arlman, degenerate polymerization), as originally proposed for alkene polymerization by Ziegler-Natta catalysts [68-70]. This behavior resembles that of homogeneous α-diimine Ni complexes [6, 20] which catalyze alkene dimerization once external activators (e.g., alkyl aluminum or boron compounds) [60, 71, 72] are added as initiators to form metal-alkyl species [53]. Such activators are also reported to enhance reaction rates but are not required to initiate the coordination-insertion catalytic cycle in the case of certain methallyl Ni catalysts [73] and SHOP (Shell Higher Olefin Process) catalysts [74] because these form Ni-hydride structures [73] *in-situ* via elimination of ligands bound to the Ni center. Recently, however, isolated Ni^{2+} cations grafted at silanol defects in Beta zeolites were proposed to catalyze coordination-insertion dimerization via Ni-ethenyl-hydride intermediates, without an externally supplied activator [51].

Mechanistic studies on Ni-based heterogeneous catalysts are complicated, in part because residual Brønsted acid (H^+) sites on supports also catalyze alkene dimerization and isomerization

[61-64] to form a mixture of terminal and internal alkene isomers, and in part because Ni^{+} sites ($Ni\text{-}SiO_2$ [57], Ni-MCM-41 [75], Ni-X [26] and Ni-Y [25]), Ni^{2+} sites (Ni-MCM-41 [49], Ni-Beta [31, 33], Ni-X [32]) and $NiOH^{+}$ sites (Ni-MCM-41 [41]) have been purported as candidate precursors to the Ni active sites. Terminal alkene products of ethene oligomerization on Ni-exchanged aluminosilicates (e.g., Y [28], MCM-22 [27], MCM-36 [27], MCM-41 [49, 65], SBA-15 [38], Beta [31, 76]) have been proposed to form at Ni^{+} cations, while internal alkene isomers have been ascribed to contributions of secondary isomerization at residual H^{+} sites. Yet, for ethene oligomerization (393 K, 25 bar C_2H_4) on Ni-exchanged Beta [33], both terminal and internal alkenes have been proposed to be formed as primary products at Ni^{2+} sites, based on observations that yields of both products increased linearly with conversion [33].

Here, we study the mechanistic details of ethene dimerization (453 K) at Ni^{2+} cations exchanged onto aluminosilicate Beta zeolites, in the absence of co-catalysts or externally supplied activators, to provide unambiguous evidence supporting the coordination-insertion mechanism. The catalytic contributions of residual Brønsted acid sites on aluminosilicate supports were suppressed by selective pre-poisoning with spectator alkali cations (Li^{+}) or base titrants (NH_4^{+}), and by weakening their acid strength by using zincosilicate supports. Isobutene, the skeletal isomer of dimer products, serves as a kinetic marker for the presence of H^{+} sites during reaction, and its disappearance after deactivation of residual H^{+} sites allows identifying butene isomers formed as primary products at Ni-derived active sites. Butenes site-time yields show an activation transient during initial reaction times at dilute ethene pressures (<0.4 kPa), which disappears at higher ethene pressures (>0.4 kPa) or in the presence of co-fed H_2 (5 kPa). These data implicate the formation of $[Ni(II)\text{-}H]^{+}$ intermediates, whose presence is detected by H/D isotopic scrambling and H_2-D_2 exchange experiments. Taken together, the presence of $[Ni(II)\text{-}H]^{+}$ intermediates formed in the absence of externally supplied activators, the prevalence of a Ni^{2+} oxidation state by *in situ* X-ray absorption spectroscopy, and the formation of linear butenes as primary products provide the requisite evidence supporting the coordination-insertion mechanism for ethene dimerization.

2.2 Experimental Methods

2.2.1 Synthesis of catalysts and control samples

Samples are referred to as X-Y-[M]Beta, where X and Y denote the extraframework cations present and M denotes the framework heteroatom (either Al or Zn). The zincosilicate support, Li-[Zn]Beta, was synthesized using a hydrothermal synthesis procedure reported by Takewaki and others [77] 0.99 g of zinc acetate dihydrate (Sigma Aldrich, 99.9% pure) and 0.316 g of lithium hydroxide monohydrate (Sigma Aldrich, 99.95% pure) were added to 46.73 g of ultrapure water (18.2 MΩ-cm) and 22.87 g of tetraethylammonium hydroxide (Sigma Aldrich, 40% (w/w)). The mixture was stirred for about 0.25 hours until all the solids were completely dissolved. 22.87 g of colloidal silica (Sigma Aldrich, 40% (w/w)) were then added to the mixture and it was stirred for 2 hours. The final synthesis gel mixture had the following molar composition: 0.65 TEAOH/SiO_2/0.05 $LiOH.H_2O$/0.03 $Zn(CH_3COO)_2.2H_2O$/30 H_2O. The gel was then transferred to Teflon-lined, stainless steel autoclaves and was heated statically at 413 K for 138 hours in a forced convection oven. The product was collected by centrifugation, washed with ultrapure water and acetone, and then dried overnight in an oven at 363 K.

The Ni-Li-[Zn]Beta sample was synthesized by nickel exchange of the Li-[Zn]Beta support using a template ion exchange procedure.[50, 78, 79] Nickel exchange was carried out at 348 K for 5 hours using 100 mL of aqueous 0.1 M $Ni(NO_3)_2$ (Sigma Aldrich, 99.999%) solution per 1 g of solid catalyst. The pH of the exchange solution was adjusted to 7 at the start using 0.1 N NaOH (Sigma Aldrich, 99.99%). The exchanged product was collected by centrifugation and washed with ultrapure water. The washed catalyst was dried at ambient temperature in flowing air. The organic template and residual nitrates were removed by treatment in flowing dry air (20 $cm^3\ s^{-1}$ g-cat^{-1}, 99.999% UHP, Matheson Tri-Gas) at 853 K (0.0167 K s^{-1}) for 10 hours, in a muffle furnace (Nabertherm LE 6/11/P300).

The Ni-H-[Al]Beta sample was synthesized starting from a commercial NH_4-[Al]Beta support (Zeolyst International, CP814E Lot# 2493-65). The NH_4-[Al]Beta was first converted into H-[Al]Beta by treatment in flowing dry air (1.67 $cm^3\ s^{-1}$ g-cat^{-1}, 99.999 % UHP, Matheson Tri-Gas) at 773 K (0.0167 K s^{-1}) for 4 hours. H-[Al]Beta was subjected to nickel exchange at 348 K for 16 hours using 100 mL of aqueous 0.3 M $Ni(NO_3)_2$ (Sigma Aldrich, 99.999%) solution per gram of solid catalyst. The product was collected by centrifugation and washed with ultrapure

water. The washed catalyst was dried at ambient temperature in flowing air. Residual nitrates were removed by treatment in flowing dry air (20 cm^3 s^{-1} g-cat^{-1}, 99.999 % UHP, Matheson Tri-Gas) at 773 K (0.0167 K s^{-1}) for 4 hours, in the muffle furnace.

The Ni-Li-[Al]Beta was also synthesized starting from commercial NH_4-[Al]Beta support (Zeolyst International, CP814E Lot: 2493-65). The NH_4-[Al]Beta was first converted into H-[Al]Beta as described above. H-[Al]Beta was subjected to lithium exchange at ambient temperature for 24 h using 100 mL of aqueous $LiNO_3$ (Sigma Aldrich, reagent grade) solution per gram of catalyst. The pH was periodically adjusted to ~7 using a 0.1 M LiOH (Sigma Aldrich, 99.995%) solution. The resulting Li-[Al]Beta was collected by centrifugation, washed with ultrapure water, dried overnight in an oven (363 K) and treated in flowing dry air (20 cm^3 s^{-1} g-cat^{-1}, 99.999 % UHP, Matheson Tri-Gas) at 773 K (0.0167 K s^{-1}) for 4 hours, in the muffle furnace. The dried Li-[Al]Beta was further subjected to nickel and lithium co-cation exchange at ambient temperature for 24 h using a solution comprising of 0.04 M $Ni(NO_3)_2$ and 0.84 M $LiNO_3$. 100 mL of this solution was used per gram of Li-[Al]Beta and the pH was periodically adjusted to ~7 using 0.1 M LiOH solution. The final product Ni-Li-[Al]Beta was collected, washed, dried and treated in flowing dry air by procedures identical to those for Ni-H-[Al]Beta.

2.2.2 Characterization

Detailed experimental procedures for X-ray diffraction (XRD), N_2 adsorption, thermogravimetric (TGA) and differential scanning calorimetry (DSC) analysis, scanning electron microscopy (SEM), elemental analysis using atomic absorption spectroscopy (AAS), quantification of H^+ sites using NH_3 temperature-programmed desorption (TPD) and ^{27}Al magic angle spinning nuclear magnetic resonance (MAS NMR) can be found in Section 2.6.2.6 of the Supporting Information.

IR spectra were collected on a Nicolet 4700 spectrometer with a HgCdTe detector (MCT, cooled to 77 K by liquid N_2) in the range 4000 to 650 cm^{-1}, by averaging 64 scans at 2 cm^{-1} resolution, and taken relative to an empty cell background reference collected under static vacuum at 303 K. Samples were pressed into self-supporting wafers (0.015-0.02 g cm^{-2}) and then sealed within a custom-built quartz IR cell with CaF_2 windows encased in an alumina silicate ceramic

chamber, the design details of which can be found elsewhere [80, 81]. Wafer temperatures were measured by K-type thermocouples (Omega) within 2 mm on each side of the wafer. A custom glass vacuum manifold interfacing with the quartz IR cell was used for sample pretreatment and exposure to controlled amounts of gaseous titrants. Prior to each experiment, sample wafers were treated in flowing dry air (6.67 $cm^3\ s^{-1}\ (g_{cat})^{-1}$) purified by an FTIR purge gas generator (Parker Balston, <1 ppm CO_2, 200 K H_2O dew point) to 723 K (0.083 K s^{-1}) for 1 h, and then held under dynamic vacuum at 723 K for 1 h. The wafer was then cooled under dynamic vacuum to 423 K for adsorption experiments with pyridine (purified via three freeze-pump-thaw cycles), or to 85 K (using liquid N_2) for adsorption experiments with CO (Matheson, 99.998%). Titrants were admitted to the cell in sequential measured doses and equilibration of the sample with each dose was considered when the final pressure in the cell and transfer line did not change for 180 s. Titrant dosing was continued until saturation, when detectable features for physisorbed CO (~2133 and 2141 cm^{-1}) and gaseous pyridine (~1600 cm^{-1}) titrant were observed. For doses during sub-saturation coverages in which the final pressure was recorded as 0.0 Torr, all of the titrant introduced to the cell was assumed to adsorb on the sample wafer. The acquired IR spectra were baseline-corrected and normalized to combination and overtone modes of zeolite Si-O-Si vibrations (1750-2100 cm^{-1}).

Diffuse reflectance UV−vis spectra were recorded using a Varian Cary 5000 UV−vis−NIR Spectrophotometer attached with a Harrick Scientific Praying Mantis *in-situ* diffuse reflectance cell. Typically, 0.04−0.05 g of each sample were loaded into the cell and pressed with a microscope slide to obtain a uniform surface. Each spectrum was collected at ambient temperature from 4000 cm^{-1} to 52000 cm^{-1} (550 $cm^{-1}\ s^{-1}$) using poly(tetraflouroethylene) (PTFE, 1 μm powder, Sigma-Aldrich) as the 100% reflectance standard, and then converted to an absorption spectrum using the Kubelka-Munk (F(R)) function. The spectra were collected on samples (i) first exposed to ambient conditions, (ii) after subsequent dehydration treatment at 673 K (~0.2 K s^{-1}) for 1 h in flowing dry air (20 $cm^3\ s^{-1}\ g_{cat}^{-1}$) followed by cooling to ambient, and (iii) after subsequent hydration treatment at ambient for 0.5 h using a wet air stream (20 $cm^3\ s^{-1}\ g_{cat}^{-1}$, ~3% H_2O) obtained by bubbling dry air through a water saturator at ambient temperature.

X-Ray absorption measurements at the Ni K-edge (8.3330 keV) were performed on the bending magnet beam line of the Materials Research Collaborative Access Team (MRCAT) at the

Advanced Photon Source, Argonne National Laboratory. Photon energies were selected using a water-cooled, double-crystal Si (111) monochromator, which was detuned by approximately 50% to reduce harmonic reflections. Measurements were made in transmission mode, and data points were acquired in three separate regions: a pre-edge region (−250 to −50 eV, step size = 10 eV, dwell time = 0.25 s), the XANES region (−50 to -30 eV, step size = 5 eV, dwell time = 0.25 s and -30 to +30 eV, step size = 0.4 eV, dwell time = 0.5 s), and the EXAFS region (up to 12 $Å^{-1}$, step size = 0.05 $Å^{-1}$, dwell time = 0.5 s). The ionization chambers were optimized for the maximum current with linear response (~10^{10} photons s^{-1}) with 10% absorption in the incident ion chamber and 70% absorption in the transmission detector. The X-ray beam was 0.5 × 2.0 mm^2 and data were collected in transmission mode. A third detector in series simultaneously collected a Ni foil reference spectrum with each measurement for energy calibration. Samples were pressed into a cylindrical sample holder consisting of six wells, forming a self-supporting wafer. The sample holder was placed in a quartz reactor tube (1 in. OD, 10 in. length) sealed with Kapton windows by two Ultra-Torr fittings through which gases could be flowed. Samples were analyzed at ambient temperature in He to determine Ni structure under hydrated conditions, and at ambient temperature after treatment at 673 K for 0.5 h in flowing He (111 $cm^3\ s^{-1}\ g_{cat}^{-1}$) to determine Ni structure under dehydrated conditions. In order to determine oxidation state of Ni under reaction conditions, the dehydrated Ni-Li-[Al]Beta sample was contacted with a stream of 0.07 kPa ethene (278 $cm^3\ s^{-1}\ g_{cat}^{-1}$) obtained by diluting ethene (3% C_2H_4, 97% He, Airgas, 99.999% purity) with He (99.999 % UHP, Airgas) at 453 K for 0.25 h, and then cooled to ambient temperature to collect the spectrum in presence of ethene.

The H_2-D_2 isotopic scrambling and exchange experiments were performed using a Micromeritics Autochem II 2920 Chemisorption analyzer connected to a Residual Gas Analyzer (Model 200, Stanford Research Systems). Samples were pelleted and sieved to a particle size between 180-250 μm. About 0.015-0.020 g of each sample was loaded into a quartz U-tube reactor and supported between two quartz wool plugs. All samples (except for 1% Pt/Al_2O_3) were first treated in flowing dry air (4.2-5.5 $cm^3\ s^{-1}\ g_{cat}^{-1}$, 99.999% UHP, Matheson Tri-Gas) at 803 K (0.0167 K s^{-1}) for 5 h, and then cooled to 453 K and flushed with Ar for 0.5 h. The 1% Pt/Al_2O_3 sample was first treated in flowing 5% H_2/95% Ar (5.5 $cm^3\ s^{-1}\ g_{cat}^{-1}$, 99.999% UHP, Matheson Tri-Gas) at 673 K (0.0167 K s^{-1}) for 1 h and then cooled to 453 K. Following the treatment, signals were continuously recorded for m/z of 2 (H_2), 3 (HD), 4 (D_2), 20 (Ar^{2+}) and 40 (Ar^+). For H/D isotopic

scrambling experiments, separate gas mixtures comprising 5% H_2/95% Ar and 5% D_2/95% Ar (99.999% UHP, Matheson Tri-Gas) were combined in different relative amounts in a bypass line to measure feed H_2/D_2/Ar compositions, and then this combined gas stream was flowed over the sample (453 K, 4.2-5.5 $cm^3\ s^{-1}\ g_{cat}^{-1}$) until steady-state signals for H_2, D_2 and HD were obtained. For H/D surface exchange experiments, the sample was first held in a flowing 5% H_2/95% Ar mixture (4.2-5.5 $cm^3\ s^{-1}\ g_{cat}^{-1}$) at 453 K for 1-2 h, followed by an instantaneous switch to an inlet 5% D_2/95% Ar mixture (4.2-5.5 $cm^3\ s^{-1}\ g_{cat}^{-1}$) using a 4-port switching valve (VICI Valco). Then, the sample was held in flowing 5% D_2/95% Ar at 453 K for 1-2 h, after which the flow was switched instantaneously to the 5% H_2/95% Ar mixture. This procedure was repeated 2-3 times (Figures 2.46 and 2.48-2.51, Supporting Information), and the HD signal was quantified using a response factor relative to an Ar internal standard (m/z = 20), obtained by equilibrating H_2/D_2 mixtures (in Ar) of different composition over a 1% Pt/Al_2O_3 sample at 673 K. The 1% Pt/Al_2O_3 sample was prepared by using a procedure reported elsewhere.[82] The moles of HD formed at Ni sites on Ni-Li-[Al]Beta and Ni-Li-[Zn]Beta were estimated by subtracting the moles of HD formed in equivalent experiments performed on Li-[Al]Beta and Li-[Zn]Beta control samples, respectively (details in Section 2.6.14.6, Supporting Information).

2.2.3 Measurement of product site-time yields

The site-time yields of ethene reaction products were measured in a plug-flow tubular quartz reactor at 453 K. Catalyst samples were pelleted and sieved to retain particles between 180-250 μm. The amount of sample charged to the reactor was varied between 0.002-0.050 g and samples were diluted with pure-silica Beta (Si-Beta-F) to ensure a minimum of 0.025 g of total solids in the reactor. The catalyst bed was supported in the reactor between two quartz wool plugs. Reactor temperatures were controlled using a resistively-heated three-zone furnace (Series 3210, Applied Test Systems) and Watlow controllers (EZ-Zone Series). The temperature of the catalyst bed was measured with a K-type thermocouple in direct contact with the external surface of the quartz tube and positioned at the center of the catalyst bed.

Before measurement of site-time yields, samples (0.01–0.10 g) were treated at 803 K (0.0167 K s^{-1}) in a 5% O_2/95% He mixture (16.7 $cm^3\ g_{cat}^{-1}\ s^{-1}$, 99.999%, Matheson Tri-Gas) for 4 hours followed by cooling to 453 K. During this time, the reactant mixture consisting of ethene

(1% C_2H_4, 5% Ar, 94% He, Matheson Tri-Gas, 99.999% purity) and He (Pure, Matheson Tri-Gas, 99.999% purity) was transferred to the GC-MS detector (Agilent 7890B GC; Agilent 5975C MSD) via heated lines (393 K) for calibration purposes. After cooling the catalyst bed to 453 K, it was treated in pure He flow (16.7 cm^3 g_{cat}^{-1} s^{-1}, 99.999%, Matheson Tri-Gas) for at least 0.5 h. The reactant mixture (also containing H_2, in the case of the co-feed experiments) was passed over the catalyst bed under near ambient pressures, and pressure measurements were recorded using a digital pressure transducer (PX309 series, OMEGA). Reactants and products were separated using GS-AL/KCl capillary column (0.530 mm ID × 50 m; Agilent) and detected using flame ionization detector. The products were identified using the NIST spectra library database and also verified by injecting known hydrocarbon standards. Reactants were diluted with He (99.999%, Matheson Tri-Gas) to vary the partial pressure and molar rates of ethene (0.01–1 kPa; 10^{-7}–10^{-4} (mol ethene) g^{-1} s^{-1}). In the case of small quantities of catalysts (0.002-0.01 g), they were diluted (1:10 ratio) with pure-silica Beta (Si-Beta-F), which was independently determined to be catalytically inert in the presence of ethene at 453 K. The catalysts were regenerated in between consecutive experiments, because they were observed to deactivate with time on stream. The ethene conversion was determined as the ratio of total carbon molar flow rates in products to the total carbon molar flow rates in the ethene feed. The molar selectivities were calculated as the ratio of the site-time yield of given product, to that of the total site-time yields of all detected products. The control samples, Li-[Zn]Beta and Li-[Al]Beta, showed undetectable reactivity in the presence of ethene (0.1-1 kPa) at 453 K.

2.3 Results and Discussion

2.3.1 Preparation of nickel ion-exchanged molecular sieves

All samples are referred to as X-Y-[M]Beta, where X and Y denote the extraframework cations present and M denotes the framework heteroatom (either Al or Zn). The H-[Al]Beta sample was prepared by treating an NH_4-[Al]Beta sample in flowing air at elevated temperature (773 K), and was subsequently ion-exchanged with either an aqueous $Ni(NO_3)_2$ solution or an aqueous $LiNO_3$ solution (pH ~7) to obtain the Ni-H-[Al]Beta or Li-[Al]Beta samples, respectively. The Ni-Li-[Al]Beta sample was prepared by simultaneous ion-exchange of Li-[Al]Beta with an aqueous solution containing $Ni(NO_3)_2$ and $LiNO_3$ (pH ~7). In the case of the zincosilicate materials, a

Table 2.1. Elemental composition of samples in this study.

Sample	Ni (wt. %)	Si/M	Li/M	Ni/M	H^+/M^a	(Cationic charge)/M[b]	Al_f/Al_{tot}[c]
H-[Al]Beta	-	11.0	0	0	0.65	0.65	0.78
Ni-H-[Al]Beta	1.1	11.0	0	0.20	0.25	0.65	n.d.
Li-[Al]Beta	-	11.0	1.01	0	n.d.	1.01	0.97
Ni-Li-[Al]Beta	1.6	11.0	0.50	0.26	n.d.	1.02	n.d.
Li-[Zn]Beta	-	4.5	0.45	0	n.d.	0.45	-
Ni-Li-[Zn]Beta	1.3	4.5	0.08	0.16	n.d.	0.40	-

M denotes framework metal center (Al^{3+} or Zn^{2+})
[a]measured by NH_3 TPD
[b]calculated assuming a 2:1 stoichiometry for Ni^{2+} and a 1:1 stoichiometry for H^+ and Li^+
[c]measured by ^{27}Al MAS NMR
n.d.: not determined

previously reported hydrothermal procedure [77] was used to synthesize Li-[Zn]Beta, which was then template ion-exchanged [50, 78, 79] with an aqueous $Ni(NO_3)_2$ solution to obtain the Ni-Li-[Zn]Beta sample. For all samples, X-ray diffraction patterns (Figure 2.8, Supporting Information), micropore volumes (Table 2.6, Supporting Information) determined from N_2 adsorption isotherms (77 K) (Figures 2.9 and 2.10, Supporting Information), ^{27}Al MAS NMR spectra (Figure 2.12, Supporting Information) and SEM images (Figure 2.13, Supporting Information) are reported in the Supporting Information.

Table 2.1 summarizes the elemental composition on each sample determined by atomic absorption spectroscopy, the number of residual H^+ sites quantified by NH_3 temperature programmed desorption (TPD), and the fraction of framework Al atoms (Al_f/Al_{tot}) determined by ^{27}Al MAS NMR. The cationic charge balance ((Cationic charge)/M, Table 2.1) on H-[Al]Beta was quantified by TPD after aqueous-phase NH_3 titration of H^+ sites, and on Li-[Al]Beta and Li-[Zn]Beta was quantified by atomic absorption spectroscopy to measure the total Li content. The cationic charge balances on each parent sample were similar to those calculated on their respective Ni-exchanged forms, which are reported in Table 2.1 and calculated from the number of residual monovalent (H^+ or Li^+) cations and the number of Ni species on the solid (assuming a 2:1 exchange stoichiometry per divalent Ni^{2+} cation). Furthermore, an elemental balance performed for lithium and nickel present on the parent Li-[Zn]Beta and the Ni-Li-[Zn]Beta solids, and the lithium and nickel present in aqueous solutions before and after the template Ni ion-exchange procedure (Table

2.8, Supporting Information), were consistent with a 2:1 exchange stoichiometry. The Ni/Al value on Ni-H-[Al]Beta (0.20, Table 2.1) was identical to the number of divalent Ni^{2+} and Co^{2+} cations exchanged at saturation on the parent H-[Al]Beta sample, which was determined by measuring ion-exchange isotherms (0.20; Figures 2.14 and 2.15 Supporting Information). The Ni/Al value on the Ni-Li-[Al]Beta sample (0.26, Table 2.1) was higher than the total number of divalent cations exchanged onto H-[Al]Beta at saturation (0.20), because of the specific exchange conditions used to prepare this sample.

The higher Ni^{2+} uptake on the Ni-Li-[Al]Beta than the Ni-H-[Al]Beta sample appears to reflect, in part, the higher fraction of tetrahedrally-coordinated framework Al sites (Al_f/Al_{tot}, Table 2.1) present on the parent Li-[Al]Beta (0.97) than the parent H-[Al]Beta (0.78) sample. The H^+/Al_{tot} value was lower (0.65, Table 2.1) than the measured fraction of framework Al (0.78, Table 2.1) on H-[Al]Beta, perhaps because partial hydrolysis of Si-O-Al bonds[83] formed some undercoordinated Lewis acidic Al during conditions of aqueous NH_3 titration, which are otherwise detected as tetrahedral species because of the hydration treatments performed prior to collecting ^{27}Al MAS NMR spectra. Such phenomena would be consistent with prior studies on Beta [83, 84] and ZSM-5 [85] zeolites, in which the replacement of NH_4^+ or alkali cations with H^+ caused the reversible transformation of tetrahedral Al into octahedral Al. Cobalt cations can be exchanged nearly exclusively as divalent Co^{2+}, and saturation Co^{2+}-exchange capacities provide quantitative measurements of zeolite framework Al centers located in close proximity. Co^{2+} cations were introduced onto H-[Al]Beta and NH_4-[Al]Beta by aqueous ion-exchange and the Co^{2+} exchange isotherms (Figures 2.15 and 2.17, Supporting Information) gave saturation Co/Al values of 0.20 and 0.35, respectively, indicating a lower fraction of Al sites in close proximity [86] on H-form samples in aqueous solution. This finding is consistent with a ^{27}Al MQ MAS NMR study of zeolite Beta [87] concluding that framework Al sites in close proximity are more susceptible than isolated Al to undergo partial or complete removal from the zeolite lattice. In the case of Li-[Zn]Beta, the Li/Zn ratio of 0.45 (Table 2.1) cannot be interpreted at face value, given that both Li^+ and tetraethylammonium (TEA^+) cations charge-balance framework Zn^{2+} during crystallization, that TEA^+ cations decompose to leave behind H^+ sites after subsequent high temperature treatments (detected from IR spectra of adsorbed CO, Figure 2.21, Supporting Information), and that framework Zn sites in different configuration require different numbers of Li^+ (0, 1, or 2) for charge-compensation [88]. Taken together, these data are consistent with the predominant

exchange of Ni^{2+} cations on Ni-H-[Al]Beta, Ni-Li-[Al]Beta, and Ni-Li-[Zn]Beta, and we next characterize Ni structure and coordination using direct spectroscopic probes.

2.3.2 Spectroscopic characterization of Ni structure and geometry

Infrared spectra of CO adsorbed (85 K) on Ni-H-[Al]Beta, Ni-Li-[Al]Beta and Ni-Li-[Zn]Beta are respectively shown in Figures 2.1a, 2.1b, and 2.1c. All samples were first treated in vacuum to 823 K (1 h) and then cooled to 85 K prior to CO exposure. IR spectra were collected with increasing CO coverage until peaks for physisorbed CO (2133, 2141 cm^{-1}) [89, 90] and CO adsorbed at silanol groups (2160 cm^{-1}) [89, 91] were observed. Absorption features for CO on NiO particles supported on Si-Beta-F (ca. 2155 cm^{-1}, Figure 2.20, Supporting Information) [31, 92] or metallic Ni nanoparticles (ca. 2030 cm^{-1}) [93, 94] were not observed on any sample.

IR spectra of CO adsorbed on Ni-H-[Al]Beta and Ni-Li-[Al]Beta (Figures 2.1a and 2.1b) samples showed peaks centered at 2213 and 2206 cm^{-1} for $Ni^{2+}(CO)$ and $Ni^{2+}(CO)_2$ complexes, respectively [94, 95]. These peaks were not observed for IR spectra of CO adsorbed on Ni-Li-[Zn]Beta (Figure 2.1c), however, a predominant feature at 2196 cm^{-1} was observed on this sample. The 2196 cm^{-1} peak appears to correspond to CO adsorbed onto Ni^{2+} cations grafted at silanol defects, as IR peaks of similar frequency have been reported for CO bound to Ni^{2+} cations in nickel-impregnated silica [96] and dealuminated Beta [95]. In the case of zincosilicate Beta, framework Zn centers have been reported to unstable in air treatment at high temperatures (>823 K) [77]. Thus, the air treatment procedure used here likely removed some framework Zn atoms to form framework vacancy defects, leading to the predominant formation of grafted Ni^{2+} cations. Moreover, the Ni-Li-[Zn]Beta sample showed a small peak centered at 2222 cm^{-1} for a second type of $Ni^{2+}(CO)$ complex that is reported [97, 98] to be distinct from the $Ni^{2+}(CO)$ complex at 2213 cm^{-1}. The formation of two types of $Ni^{2+}(CO)$ complexes has been speculated to reflect Ni^{2+} cations located in different locations of Beta [95] and ZSM-5 [97, 98].

In addition to features corresponding to Ni^{2+} sites, IR peaks for CO adsorbed at Brønsted acid sites (2174 cm^{-1} [95, 99]; H-[Al]Beta spectrum in Figure 2.18, Supporting Information) were only observed on Ni-H-[Al]Beta (Figure 2.1a), while those for CO adsorbed at Li^+ cations (2185 cm^{-1}; Li-[Al]Beta spectrum in Figure 2.19 and Li-[Zn]Beta spectrum in Figure 2.21, Supporting

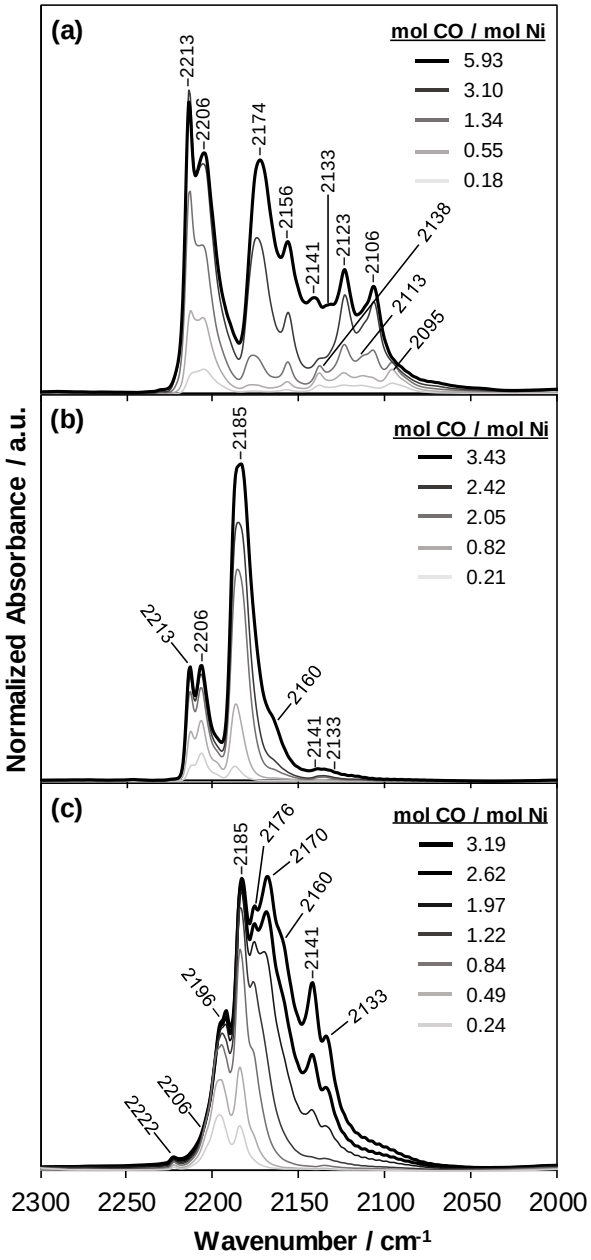

Figure 2.1. Infrared difference spectra (relative to a vacant surface) with increasing amounts (light to dark) of CO adsorbed at 85 K for (a) Ni-H-[Al]Beta, (b) Ni-Li-[Al]Beta and (c) Ni-Li-[Zn]Beta. The dark black line indicates spectra collected at saturation coverages (CO/Ni > 1.0; peaks observed at 2133 and 2141 cm^{-1} for physisorbed CO)

Information) were observed on Ni-Li-[Al]Beta (Figure 2.1b) and Ni-Li-[Zn]Beta (Figure 2.1c). In the case of Ni-Li-[Zn]Beta (Figure 2.1c), the IR peak at 2170 cm^{-1} was also observed on Li-[Zn]Beta (Figure 2.21, Supporting Information) but not on H-[Al]Beta (Figure 2.18, Supporting Information) nor on Li-[Al]Beta (Figure 2.19, Supporting Information), and is assigned to Zn-OH

groups. The 2176 cm^{-1} peak observed on Ni-Li-[Zn]Beta (Figure 2.1c) was also observed on Li-[Zn]Beta (Figure S14, Supporting Information), and is analogous to 2174 cm^{-1} peak for Brønsted sites on H-[Al]Beta (Figure 2.21, Supporting Information) and Ni-H-[Al]Beta (Figure 2.1b) and is therefore assigned to minority Brønsted sites in zincosilicates that are proposed to be too weak to protonate pyridine [88] (details in Section 2.6.4.5, Supporting Information).

IR spectra collected at low CO coverages (CO/Ni < 1.0) of Ni-H-[Al]Beta (Figure 2.1a) also showed peaks centered at 2113 cm^{-1} for $Ni^{+}(CO)$, and at 2138 and 2095 cm^{-1} for the symmetric and asymmetric modes of $Ni^{+}(CO)_2$, respectively [94, 95]. These IR peaks disappeared with increasing CO coverage (CO/Ni > 1.0), which led to the emergence of new peaks centered at 2106, 2123 and 2156 cm^{-1} corresponding to $Ni^{+}(CO)_3$ complexes [94, 95], consistent with the conversion of $Ni^{+}(CO)$ and $Ni^{+}(CO)_2$ complexes into $Ni^{+}(CO)_3$. The Ni^{+} cations appeared to have formed upon vacuum treatment (823 K, 1 h) by Ni^{2+} auto-reduction phenomena that have reported previously for Ni-exchanged NaY[49] and Ni-impregnated ZSM-5 [98]. Higher IR peak intensities for CO at Ni^{+} cations in NaY were observed as the temperature of thermal treatments (air, 8 h) increased from 473 K to 823 K [49], and in ZSM-5 were observed for samples treated in vacuum (but not in O_2) via mechanisms proposed to occur by consumption of hydroxyl groups [98]. Absorption features for Ni^{+} carbonyl complexes were not observed on Ni-Li-[Al]Beta (Figure 2.1b) or Ni-Li-[Zn]Beta (Figure 2.1c) samples that contained residual Li^{+} cations, suggesting that auto-reduction events may involve H^{+} sites. The small intensity of the $Ni^{+}(CO)$ peak (2113 cm^{-1}) relative to the $Ni^{2+}(CO)$ peak (2213 cm^{-1}) on Ni-H-[Al]Beta (Figure 2.1c), however, indicates that only a minority fraction of Ni^{+} is formed during the vacuum treatment, given that extinction coefficients measured for the $Ni^{+}(CO)$ peak at 2113 cm^{-1} are reported to be 10 times larger than that for the $Ni^{2+}(CO)$ peak at 2213 cm^{-1} [100].

Diffuse reflectance UV-visible (DRUV) spectra collected at ambient temperature of Ni-H-[Al]Beta, Ni-Li-[Al]Beta and Ni-Li-[Zn]Beta are shown respectively in Figures 2.2a, 2.2b and 2.2c, when collected under hydrated (light traces) and dehydrated (dark traces) conditions. All samples were first treated in flowing dry air to 673 K (1 h), before cooling to ambient temperature to collect spectra under dehydrated conditions. The samples were then rehydrated in flowing wet air (0.5 h) to collect spectra under hydrated conditions at ambient temperature. The sharp features

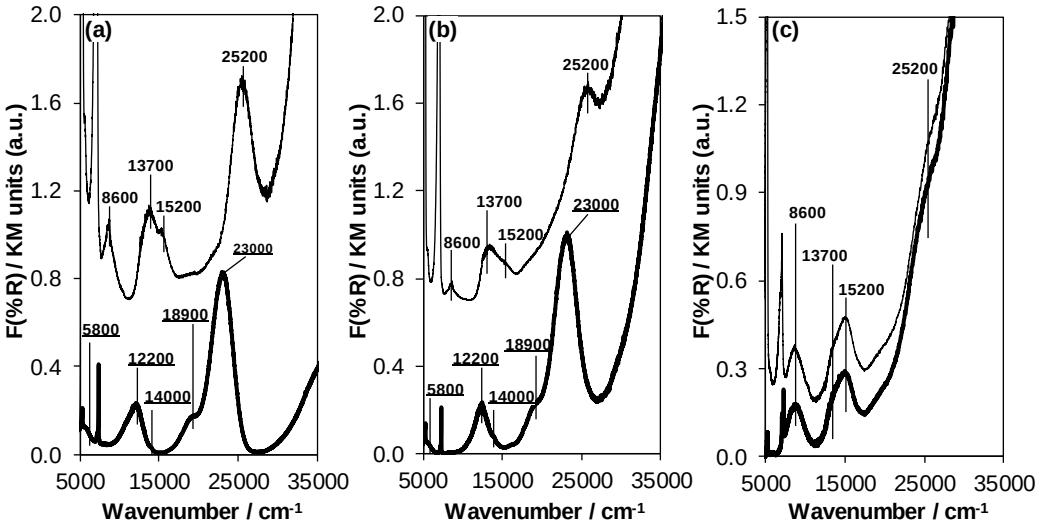

Figure 2.2. Diffuse reflectance UV-vis spectra collected under hydrated (light traces) and dehydrated conditions (dark traces) for (a) Ni-H-[Al]Beta, (b) Ni-Li-[Al]Beta and (c) Ni-Li-[Zn]Beta. Underlined and non-underlined wavenumbers indicate the absorption features for distorted tetrahedral Ni^{2+} cations and for octahedral Ni^{2+} cations, respectively

centered at 5250 and 7200 cm^{-1} for all samples under hydrated conditions (light traces) represent the combination of stretching and bending modes of H_2O, and the first overtone of the silanol O-H stretching vibration, respectively [101, 102].

The light traces in Figures 2.2a, 2.2b and 2.2c, respectively show the DRUV spectra of Ni-Li-[Al]Beta, Ni-H-[Al]Beta and Ni-Li-[Zn]Beta samples collected under hydrated conditions. All three samples showed absorption bands at 8600, 13700 and 25500 cm^{-1}, respectively corresponding to the spin-allowed d-d transitions ($^3A_{2g}(F) \rightarrow {}^3T_{2g}(F)$, $^3A_{2g}(F) \rightarrow {}^3T_{1g}(F)$, $^3A_{2g}(F) \rightarrow {}^3T_{1g}(P)$) of an octahedral $Ni^{2+}(H_2O)_6$ species [103-106]. These samples also showed an additional band at 15200 cm^{-1} for the spin-forbidden d-d transition ($^3A_{2g}(F) \rightarrow {}^1E_g(D)$) of the $Ni^{2+}(H_2O)_6$ species. This spin-forbidden d-d transition was observed previously for Ni-exchanged Beta [107, 108] and FAU [109, 110] and was attributed to spin-orbit coupling, which causes the $^1E_g(D)$ and $^3T_{1g}(F)$ levels to become similar in energy [110]. Thus, under hydrated conditions, Ni^{2+} cations on Ni-H-[Al]Beta, Ni-Li-[Al]Beta and Ni-Li-[Zn]Beta are present in octahedral coordination with oxygen atoms.

The dark traces in Figures 2.2a, 2.2b and 2.2c, respectively show the DRUV spectra of Ni-Li-[Al]Beta, Ni-H-[Al]Beta and Ni-Li-[Zn]Beta samples under dehydrated conditions. The Ni-H-

[Al]Beta and Ni-Li-[Al]Beta samples showed absorption bands at 5800, 12200, 14000, 18900 and 23000 cm^{-1}, respectively corresponding to the spin-allowed d-d transitions ($^3T_1(F) \rightarrow {}^3T_2(F)$, $^3T_1(F) \rightarrow {}^3A_2(F)$, and $^3T_1(F) \rightarrow {}^3T_1(P)$ that is split into three components because of tetrahedral distortion [110]) of Ni^{2+} cations in distorted tetrahedral coordination [110-112]. The transformation of Ni^{2+} cations from an octahedral (hydrated) to distorted tetrahedral (dehydrated) geometry is consistent with the predominance of exchanged Ni^{2+} cations in ion-exchange positions of Ni-H-[Al]Beta (Figure 2.2a) and Ni-Li-[Al]Beta (Figure 2.2b), consistent with their cation site balances (Table 2.1) and CO IR spectra (Figure 2.1). The DRUV spectrum of Ni-Li-[Zn]Beta under dehydrated conditions (Figure 2.2c, dark trace), however, was similar to that collected under hydrated conditions (Figure 2.2c, light trace), indicating that Ni^{2+} cations remain predominantly octahedrally coordinated to oxygen atoms. Similar observations of octahedrally-coordinated Ni^{2+} cations under ambient and dehydrated conditions have been reported for Ni-exchanged [Si]MCM-41 [50], proposed to contain Ni^{2+} cations grafted at six-membered siloxane rings and coordinated to oxygen atoms from adjacent hydroxyl groups [50]. Thus, these findings suggest the predominance of grafted Ni^{2+} species in Ni-Li[Zn]Beta, consistent with CO IR spectra (Figure 2.1).

X-ray absorption near edge structure (XANES) spectra are shown in Figures 2.24 and 2.25 (Supporting Information), for Ni-H-[Al]Beta, Ni-Li-[Al]Beta and Ni-Li-[Zn]Beta under hydrated and dehydrated conditions, and for Ni-Li-[Al]Beta during ethene dimerization (453 K, 0.07 kPa), with the results summarized in Table 2.2. Under both hydrated and dehydrated conditions, the pre-edge energy (Table 2.2) and pre-edge feature (Figure 2.25, Supporting Information) of Ni-H-[Al]Beta, Ni-Li-[Al]Beta and Ni-Li-[Zn]Beta samples were the same as those of a NiO standard, indicating an oxidation state of +2, consistent with predominance of Ni^{2+} cations as indicated by the site balance (Table 2.1) and CO IR spectroscopy (Figure 2.1). Further, the XANES spectra collected for the dehydrated Ni-Li-[Al]Beta sample and the Ni-Li-[Al]Beta sample during reaction with ethene (453 K, 0.07 kPa) were identical (Figures 2.24 and 2.25), providing evidence for the prevalence of the +2 oxidation state for Ni during ethene dimerization catalysis, consistent with prior reports for propene oligomerization on Ni-X [32].

Table 2.2. XANES results for Ni-H-[Al]Beta, Ni-Li-[Al]Beta and Ni-Li-[Zn]Beta under hydrated and dehydrated conditions, and for Ni-Li-[Al]Beta during ethene dimerization (453 K, 0.07 kPa).

Sample, condition	Pre-edge energy (keV)	Edge energy (keV)	Oxidation state
Ni-H-[Al]Beta, hydrated	8.3333	8.3429	+2
Ni-H-[Al]Beta, dehydrated	8.3331	8.3406	+2
Ni-Li-[Al]Beta, hydrated	8.3333	8.3429	+2
Ni-Li-[Al]Beta, dehydrated	8.3331	8.3406	+2
Ni-Li-[Al]Beta, dimerization (453 K, 0.07 kPa ethene)	8.3331	8.3406	+2
Ni-Li-[Zn]Beta, hydrated	8.3332	8.3423	+2
Ni-Li-[Zn]Beta, dehydrated	8.3332	8.3423	+2
NiO, dehydrated	8.3332	8.3410	+2

The coordination geometry of Ni^{2+} cations was quantitatively assessed from the extended X-ray absorption fine structure (EXAFS) region. Figures 2.26 and 2.27 (Supporting Information) show the EXAFS regions of the Ni-H-[Al]Beta and Ni-Li-[Al]Beta samples under hydrated and dehydrated conditions, and the results are summarized in Table 2.3. The fitted EXAFS modelconsidered the first shell to represent Ni-O scatter and the second shell to represent either Ni-Si or Ni-Al scatter. The Ni-H-[Al]Beta and Ni-Li-[Al]Beta samples under hydrated and dehydrated conditions showed Ni-O coordination numbers of 6 and 4, respectively, indicating that Ni was present as octahedral $Ni^{2+}(H_2O)_6$ under hydrated conditions and as tetrahedral Ni^{2+} cationscoordinated to framework oxygens after dehydration, consistent with DRUV spectra (Figures 2.2a and 2.2b). Further, Figure 2.28 (Supporting Information) shows the EXAFS region of the Ni-Li-[Zn]Beta sample under hydrated and dehydrated conditions, and the results are also summarized in Table 2.3. The fitted EXAFS model considered the first shell to represent Ni-O scatter, however, no appropriate model was found to describe the second shell scatter. The hydrated and dehydrated Ni-Li-[Zn]Beta samples both showed a Ni-O coordination number of 6, consistent with the predominance of grafted Ni^{2+} species in Ni-Li-[Zn]Beta, as evident from its DRUV (Figure 2.2c) and CO IR (Figure 2.1) spectra

.

Table 2.3. EXAFS fitting results for Ni-Li-[Al]Beta and Ni-Li-[Zn]Beta samples

Sample, condition	Scattering pair	Coordination number	Distance (Å)
Ni-H-[Al]Beta, hydrated	Ni-O	6.1 ± 0.1	2.04 ± 0.01
	Ni-Si/Al	1.7 ± 0.6	3.21 ± 0.02
Ni-H-[Al]Beta, dehydrated	Ni-O	4.7 ± 0.8	2.00 ± 0.02
	Ni-Si/Al	2.1 ± 0.2	2.74 ± 0.01
Ni-Li-[Al]Beta, hydrated	Ni-O	6.2 ± 0.4	2.04 ± 0.01
	Ni-Si/Al	1.6 ± 0.7	3.23 ± 0.02
Ni-Li-[Al]Beta, dehydrated	Ni-O	4.3 ± 0.2	2.00 ± 0.01
	Ni-Si/Al	1.9 ± 0.2	2.75 ± 0.01
Ni-Li-[Al]Beta, dimerization (453 K, 0.07 kPa ethene)	Ni-O	4.1 ± 0.2	2.00 ± 0.01
	Ni-Si/Al	2.0 ± 0.2	2.74 ± 0.01
Ni-Li-[Zn]Beta, hydrated	Ni-O	6.6 ± 0.4	2.04 ± 0.01
Ni-Li-[Zn]Beta, dehydrated	Ni-O	6.6 ± 0.4	2.04 ± 0.01
NiO, dehydrated	Ni-O	6.0	2.07 ± 0.01

In summary, CO IR, DRUV and XAS spectroscopy indicate that Ni is predominantly present as exchanged Ni^{2+} cations on Ni-H-[Al]Beta and Ni-Li-[Al]Beta, and as grafted Ni^{2+} cations on Ni-Li-[Zn]Beta. In the dehydrated state and during *in situ* ethene dimerization, Ni^{2+} cations in Ni-Li-[Al]Beta are four-coordinate and predominantly in distorted tetrahedral geometry according to UV-Vis, XANES and EXAFS data, consistent with the distorted tetrahedral environment of Ni^{2+} sites observed within the Ni-MFU-4l MOF material [113] that catalyzes ethene dimerization by the coordination-insertion mechanism [58]. Although Ni^{+} cations were observed in minority amounts on the Ni-H-[Al]Beta sample after vacuum treatment, such species are not expected to persist after an oxidative treatment. In addition, residual Brønsted acid sites were detected on Ni-H-[Al]Beta but not on Ni-Li-[Al]Beta, while the residual Brønsted acid sites detected on Ni-Li-[Zn]Beta are of weaker acid strength than those in aluminosilicates, as evident by their inability to protonate pyridine under equivalent conditions. Next, we use these model samples to probe the reaction pathways of ethene on Ni^{2+} cations and H^{+} sites.

2.3.3 Ethene reaction pathways on Ni^{2+} cations and Brønsted acid sites.

Scheme 2.1 shows a simplified representation of the metallacycle mechanism for ethene dimerization catalyzed by Ni^{δ} centers, where δ is the initial formal oxidation state. The catalytic cycle involves successive coordination of two ethene molecules, followed by two-electron

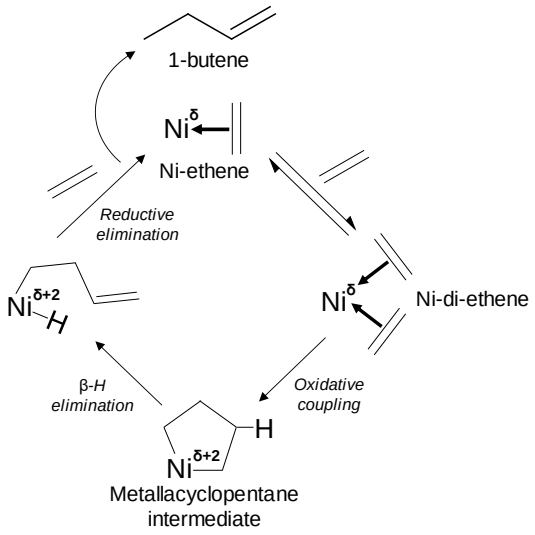

Scheme 2.1. Metallacycle mechanism for ethene dimerization at a Ni^{δ} active site.

oxidation of a Ni^{δ} center to form a $Ni^{\delta+2}$ metallacyclopentane complex, which undergoes β-hydride elimination and subsequent reductive elimination to form the terminal alkene (1-butene) as the predominant product [3, 6, 18]. Scheme 2.2 shows a simplified representation of the coordination-insertion mechanism for ethene dimerization at $[Ni(II)\text{-}H]^{+}$ sites, first involving coordination and insertion of ethene into a Ni-hydride bond, and then into a Ni-alkyl bond, followed by β-hydride elimination to form 1-butene [6]. The formal Ni oxidation state is +2 for all reactive intermediates, and internal isomers (cis-2-butene, trans-2-butene) are also formed as primary reaction products by a parallel isomerization pathway [20, 60, 71]. In contrast to the metallacycle mechanism, the coordination-insertion mechanism is reported to be initiated by external activators for most homogeneous Ni systems [114] except for methallyl [73] and SHOP-type [74] catalysts, it forms internal alkenes as primary products and the Ni metal center does not undergo a redox cycle. The key differences between the two mechanisms are summarized in Table 2.4.

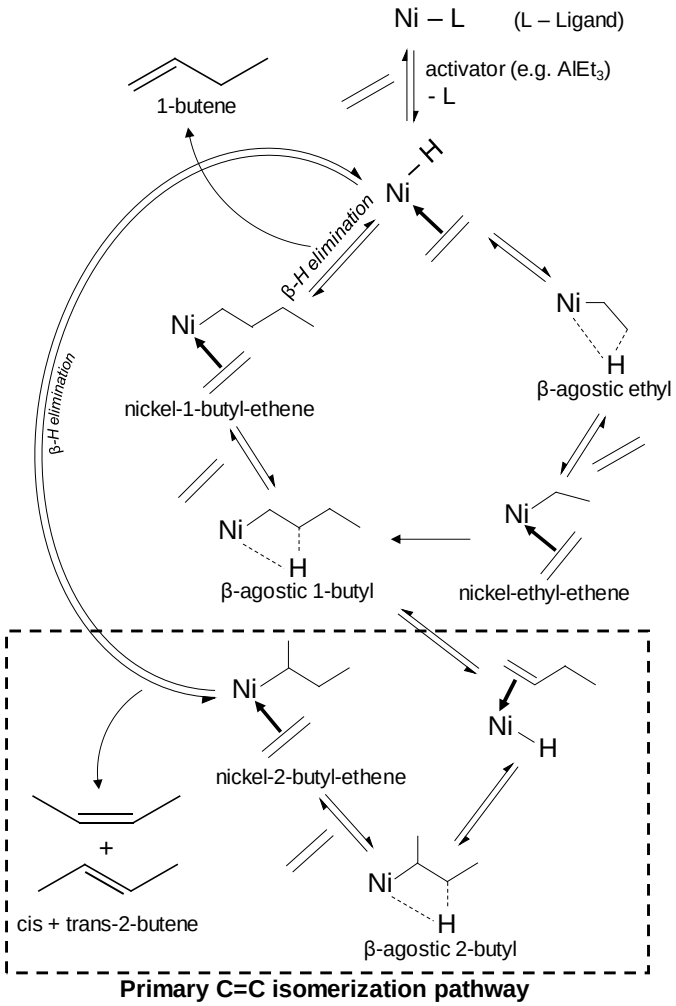

Scheme 2.2. Coordination-insertion mechanism for ethene dimerization at $[Ni(II)\text{-}H]^+$ active site. The formal oxidation state of Ni is +2 for all Ni intermediates.

Table 2.4. Comparison between coordination-insertion and metallacycle mechanisms for homogeneous Ni complexes for ethene dimerization

	Coordination-insertion	**Metallacycle**
Active site	$[Ni(II)– H]^+$	Ni^{δ}
Activator Requirement	Needed in most cases	Not needed
Ni oxidation state	+2	δ, δ+2
Product Selectivity	1-butene, cis-2-butene, trans-2-butene	1-butene

Mechanistic studies for alkene dimerization catalysis using Ni^{2+} cations supported on aluminosilicates can be ambiguous when contributions from residual H^+ sites convolute the analysis of alkene reaction pathways originating from Ni^{2+} sites. In order to discriminate the alkene reaction pathways originating from Ni^{2+} cations and H^+ sites, 0.4 kPa of ethene was contacted at 453 K under differential conversion (<5 %) with samples containing only H^+ sites (H-[Al]Beta), both Ni^{2+} cations and H^+ sites (Ni-H-[Al]Beta), both Ni^{2+} cations and trace amounts of residual H^+ sites (Ni-Li-[Al]Beta) that have been further pre-poisoned with NH_3 (Ni-Li-[Al]Beta-NH_3), and both Ni^{2+} cations and weaker residual H^+ sites (Ni-Li-[Zn]Beta). Under these conditions (453 K, 0.4 kPa), ethene conversion increased during initial time for the Ni-Li-[Zn]Beta and Ni-Li-[Al]Beta-NH_3 samples (Figure 2.30, Supporting Information), while this activation behavior was not observed for the H-[Al]Beta, Ni-H-[Al]Beta and Ni-Li-[Al]Beta samples (Figure 2.29, Supporting Information). On all samples, ethene conversion decreased with further time on stream (Figures 2.28 and 2.30, Supporting Information) indicating deactivation at long times.

Figure 2.3 shows product molar selectivities for H-[Al]Beta, Ni-H-[Al]Beta, Ni-Li-[Al]Beta, Ni-Li-[Al]Beta-NH_3 and Ni-Li-[Zn]Beta at 453 K and 0.4 kPa ethene pressure. The product molar selectivities for Ni-Li-[Al]Beta-NH_3 and Ni-Li-[Zn]Beta were invariant with ethene conversion within differential ranges (<2%) (Figures 2.31 and 2.32, Supporting Information) while those for H-[Al]Beta, Ni-H-[Al]Beta and Ni-Li-[Al]Beta changed with conversion (Figures 2.33-

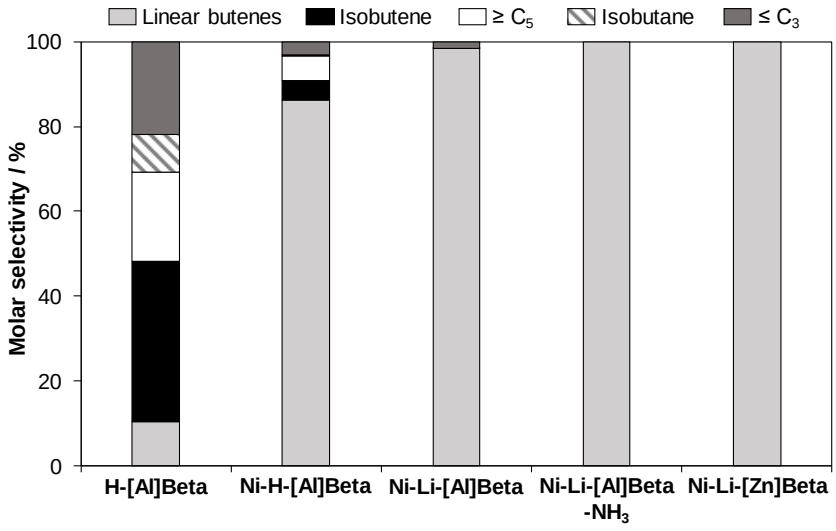

Figure 2.3. Product molar selectivities at 453 K, 0.4 kPa ethene for H-[Al]Beta (1.4% conv.), Ni-H-[Al]Beta (1.4% conv.), Ni-Li-[Al]Beta (1.4% conv.), Ni-Li-[Zn]Beta (1.3% conv.) and Ni-Li-[Al]Beta-NH_3 (without pretreatment) (1.6% conv.). FID Detection limit ~ 0.02 ppm

2.35, Supporting Information) and thus are compared at iso-conversion values (1.4%) in Figure 2.3. All samples formed 1-butene, cis-2-butene and trans-2-butene isomers (linear butenes). The H-[Al]Beta sample showed only 10% selectivity towards linear butenes, and formed significant amounts of isobutene, C_3 and smaller hydrocarbons, C_5 and larger hydrocarbons, and isobutane. The Ni-H-[Al]Beta sample predominantly formed linear butenes and smaller amounts of other products. The Ni-Li-[Al]Beta sample formed trace amounts of cracking products and isobutene, while the Ni-Li-[Al]Beta-NH_3 sample and the Ni-Li-[Zn]Beta sample selectively (>99%) formed linear butenes without any other detectable side products. These findings indicate that ethene dimerization to form linear butenes occurs on Ni^{2+} cations, while the H^+ sites present on [Al]Beta samples also catalyze the expected skeletal isomerization of dimer products to isobutene, along with cracking, oligomerization and hydride transfer reactions [115-120].

The linear butenes formed at Ni^{2+}-derived sites and H^+ sites consisted of 1-butene, cis-2-butene and trans-2-butene isomers, suggesting that alkene double bond isomerization may be catalyzed by both types of sites. The two competing mechanisms (metallacycle and coordination-insertion) proposed for alkene dimerization on Ni cations differ in their selectivity towards the isomers of dimer products. In the case of dimerization of terminal alkenes (α-olefins), the metallacycle mechanism only forms terminal alkene dimers [3], whereas the coordination-insertion mechanism forms both terminal and internal alkene dimers [6]. Moreover, the coordination-insertion mechanism involves a primary reaction route for forming internal alkene dimers, which does not require desorption and re-adsorption of terminal alkene dimers (Scheme 2.2). Therefore, to investigate the contributions of butene isomer formation, the ratios of 2-butenes/1-butene and isobutene/total butenes were measured (453 K, 0.2 kPa C_2H_4) as a function of reaction time on H-[Al]Beta, Ni-Li-[Al]Beta and Ni-Li-[Zn]Beta. All samples deactivated under these conditions, as the ethene conversion decreased with reaction time (Figure 2.36, Supporting Information).

Figure 2.4a shows the 2-butenes/1-butene and isobutene/total butene ratios measured with reaction time on H-[Al]Beta (453 K, 0.2 kPa, 250 s (mol ethene)$^{-1}$ mol H^+), with a horizontal dashed line denoting the 2-butenes/1-butene ratio expected from thermodynamic equilibrium at 453 K (Section 2.6.10, Supporting Information). Linear butenes were formed in equilibrated amounts at initial reaction times, but the 2-butenes/1-butene ratio decreased with time on stream,

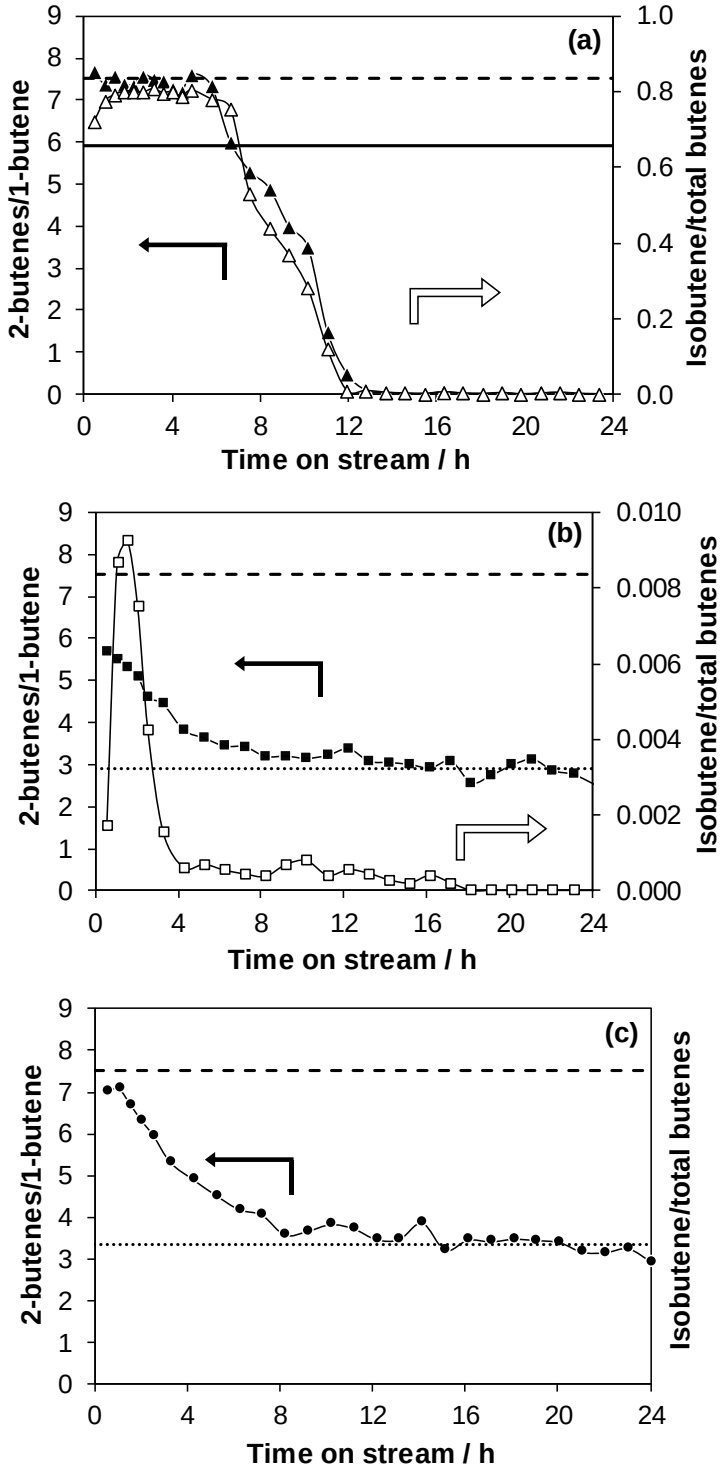

Figure 2.4. Variation of 2-butenes/1-butene ratio (filled symbols) and isobutene/total butenes ratio (unfilled symbols) for (a) H-[Al]Beta (▲) at 453 K, 0.2 kPa, 250 s (mol ethene)$^{-1}$ mol H^+, (b) Ni-Li-[Al]Beta (■) (453 K, 0.4 kPa, 2.4 s (mol ethene)$^{-1}$ mol Ni), and (c) Ni-Li-[Zn]Beta (●) (453 K, 0.7 kPa, 10.6 s (mol ethene)$^{-1}$ mol Ni). Lines are included to guide the eye: equilibrated 2-butenes/1-butene ratio at 453 K (– – – –), equilibrated isobutene/total butenes ratio at 453 K (——), asymptotic steady-state 2-butenes/1-butene ratio (·····)

eventually reaching zero as the ethene conversion decreased to zero upon complete deactivation of H^+ sites (Figure 2.36a, Supporting Information). This decrease in 2-butenes/1-butene ratio was also concurrent with the decrease in the isobutene/total butenes ratio, consistent with the deactivation of H^+ sites that catalyze skeletal isomerization (Figure 2.36a, Supporting Information).

Figure 2.4b shows the 2-butenes/1-butene ratio, and the isobutene/total butenes ratio, measured with reaction time on Ni-Li-[Al]Beta (453 K, 0.2 kPa, 2.4 s (mol ethene)$^{-1}$ mol Ni). In contrast to H-[Al]Beta, the initial 2-butenes/1-butene ratio measured at this site-time was lower than expected from thermodynamic equilibrium, indicating that linear butenes were not quasi-equilibrated. Also, during initial reaction times, a small fraction of isobutene was detected (Figure 2.4b), attributed to skeletal isomerization on trace H^+ sites present below the detection limits of the characterization techniques used here (CO IR, AAS) or on H^+ sites generated *in situ* during Ni^{2+} activation to form $[Ni(II)\text{-}H]^+$ intermediates and proximal H^+ sites.[59] The 2-butenes/1-butene ratio for Ni-Li-[Al]Beta (Figure 2.4b) decreased with further time on stream, concurrent with a decrease in the isobutene/total butenes ratio, as expected from the deactivation of trace amounts of H^+ sites. Isobutene was no longer detectable after 12 h of reaction time, after which the 2-butenes/1-butene ratio reached a steady-state but non-equilibrated value despite continued deactivation (Figure 2.36b, Supporting Information), indicating that butene double bond isomerization as solely catalyzed by the remaining Ni^{2+}-derived active sites as they continued to deactivate.

In order to confirm that butene double bond isomerization was catalyzed by Ni^{2+}-derived active sites, the 2-butenes/1-butene ratio was measured with reaction time on the Ni-Li-[Zn]Beta sample (453 K, 0.7 kPa, 10.6 s (mol ethene)$^{-1}$ mol Ni), as shown in Figure 2.4c. The 2-butenes/1-butene ratio decreased with reaction time to eventually reach a steady-state but non-equilibrated value despite continued deactivation (Figure 2.36c, Supporting Information), similar to the observation on Ni-Li-[Al]Beta. No skeletal isomer products of butene were detected for Ni-Li-[Zn]Beta, although residual H^+ sites on [Zn]Beta formed double bond isomerization products, as also reported previously for propene oligomerization (453 K).[121] Therefore, the decrease in 2-butenes/1-butene ratio with time on stream for Ni-Li-[Zn]Beta may be attributed to the deactivation of residual H^+ sites, which mediate alkene double bond isomerization but not alkene

skeletal isomerization under the conditions studied. The steady-state but non-equilibrium distribution of linear butenes on Ni-Li-[Al]Beta and Ni-Li-[Zn]Beta samples, after residual H^+ sites had deactivated, reflects butene double bond isomerization events that occur at Ni^{2+}-derived active sites.

Butene double bond isomerization on Ni-Li-[Al]Beta and Ni-Li-[Zn]Beta occur at both Ni^{2+}-derived and H^+ sites during initial reaction times, but only at remaining Ni^{2+}-derived sites at long time on stream, as denoted by the dashed lines in Figure 2.4 for the asymptotic limit for 2-butenes/1-butene ratio. In order to probe whether double bond isomerization pathways reflected primary or secondary reactions on Ni^{2+}-derived and H^+ sites, the reactant site-time was varied at fixed ethene pressure at 453 K. The effect of reactant site-time on the 2-butenes/1-butene ratio

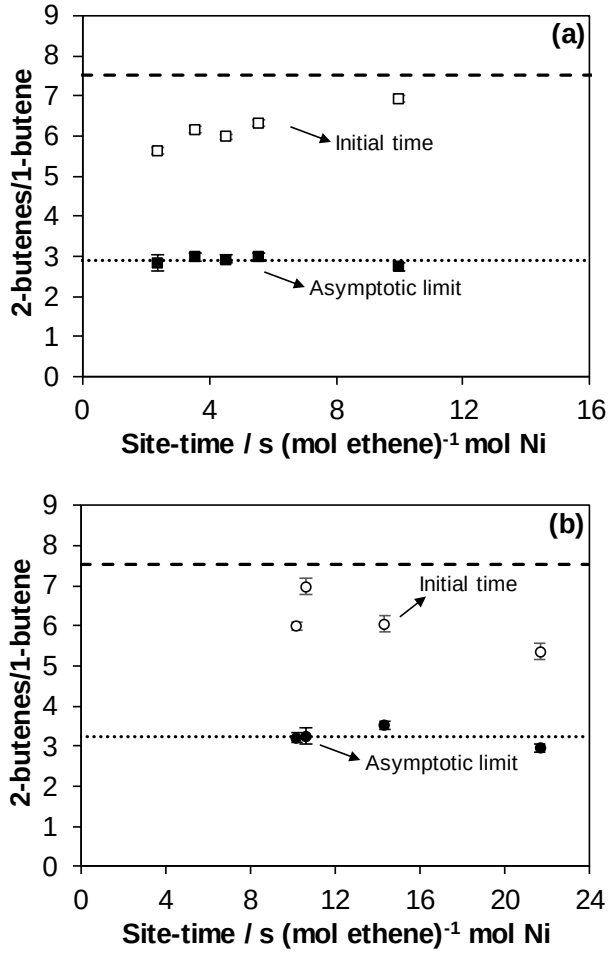

Figure 2.5. Effect of site-time on 2-butenes/1-butene ratio measured at 453 K during initial time on stream (hollow symbols) and after reaching asymptotic limit (filled symbols) for (a) Ni-Li-[Al]Beta (■) at 0.2 kPa, and (b) Ni-Li-[Zn]Beta (●) at 0.7 kPa. Lines are included to guide the eye: equilibrated 2-butenes/1-butene ratio at 453 K (– – –), asymptotic steady-state 2-butenes/1-butene ratio (·····).

measured at initial reaction times, during which both Ni^{2+}-derived and H^+ sites are turning over, and on the 2-butenes/1-butene ratio measured in the asymptotic limit at long reaction times, during which only Ni^{2+}-derived sites are turning over, is shown in Figures 2.5a and 2.5b for Ni-Li-[Al]Beta and Ni-Li-[Zn]Beta, respectively. The asymptotic 2-butenes/1-butene ratio was invariant with site-time for Ni-Li-[Al]Beta and Ni-Li-[Zn]Beta, indicating that butene double bond isomerization on Ni^{2+}-derived sites occurs via primary pathways, consistent with the coordination-insertion mechanism. In contrast, the initial 2-butenes/1-butene ratio measured on Ni-Li-[Al]Beta increased with increasing site-time (Figure 2.5a), with a non-zero value upon extrapolation to zero site-time, consistent with a secondary reaction pathway for butene double bond isomerization on residual H^+ sites that occurs in parallel to a primary reaction pathway on Ni^{2+}-derived sites. The initial 2-butenes/1-butene ratio measured on Ni-Li-[Zn]Beta (Figure 2.5b) showed no discernable dependence on reactant site-time, because of the low conversion range studied here, precluding any conclusions about the nature of alkene double bond isomerization pathways at non-Ni^{2+}-derived sites on this sample.

Prior reports have proposed that Ni sites catalyze butene double bond isomerization on Ni-H-[Al]Y [52], based on 1-butene selectivities among the C_4 products measured during pseudo-steady-state at long times on stream, after residual H^+ sites had presumably deactivated, which were similar to those measured on Ni-H-[Al]Y samples whose H^+ sites were poisoned with NH_3 or pyridine. Yet, other reports (ethene oligomerization at 323-423 K on Ni-H-[Al]MCM-41 [36], Ni-H-[Al]MCM-22 [27], Ni-H-[Al]MCM-36 [27], Ni-H-[Al]USY [28] and Ni-H-[Al]SBA-15 [38]) propose 1-butene formation at Ni sites and secondary double-bond isomerization at H^+ sites, based on 1-butene selectivities that decrease with increasing H^+ site density and reactant site-time (ethene conversion). Although previously reported decreases in 1-butene selectivity with increasing site-time [38] are consistent with the observations in Figure 2.5a, the data and analysis presented here clarify that these observations reflect double bond isomerization via secondary reaction pathways at H^+ sites, which operate in parallel to a primary reaction pathway at Ni^{2+}-derived sites.

2.3.4 Active site structure and formation in absence of an activator

Another distinction between the coordination-insertion and metallacycle mechanisms is the difference between their purported active site structures. Active sites for the coordination-insertion mechanism are proposed to be Ni(II)-hydride or Ni(II)-alkyl species, often generated from Ni^{2+} cations using external activators or initiators, while those for the metallacycle mechanism are also proposed to include reduced Ni states whose formation do not require external activators. Both Ni-Li-[Al]Beta and Ni-Li-[Zn]Beta samples show evidence for coordination-insertion mechanism even though external activators were absent, although Ni-Li-[Zn]Beta (but not Ni-Li-[Al]Beta) showed an activation transient at 453 K and 0.4 kPa ethene during initial reaction times (Figures 2.29 and 2.30, Supporting Information). This activation transient, however, was also observed for Ni-Li-[Al]Beta (Figure 2.37, Supporting Information) for ethene pressures below 0.4 kPa, while for Ni-Li-[Zn]Beta (Figure 2.38, Supporting Information) it was observed for all ethene pressures (0-1 kPa) studied.

The duration of the activation period for Ni-Li-[Al]Beta at 453 K and fixed ethene pressure was invariant with ethene site-time at each pressure studied (Figure 2.39a, Supporting Information), while no discernable dependence on ethene site-time was observed for Ni-Li-[Zn]Beta (Figure 2.39b, Supporting Information). The duration of the activation period measured on Ni-Li-[Al]Beta decreased with increasing ethene pressure and was undetectable above 0.4 kPa, while that measured on Ni-Li-[Zn]Beta was invariant with ethene pressure, as shown in Figure 2.6. These findings are consistent with ethene-assisted formation of Ni-hydride intermediates *in situ* from exchanged Ni^{2+} cations on Ni-Li-[Al]Beta, as proposed by experiment to occur at Ni^{2+}

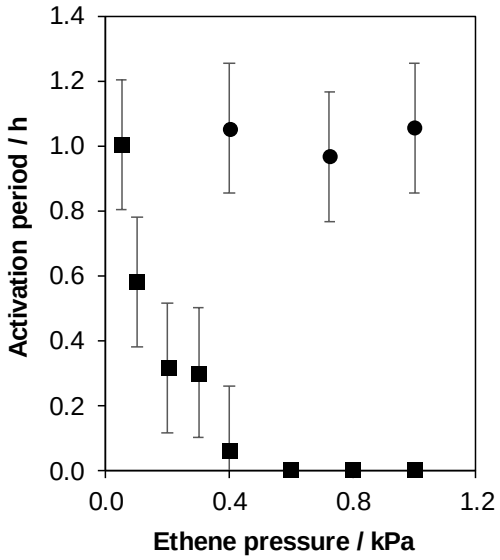

Figure 2.6. Effect of ethene pressure on activation period measured at 453 K for Ni-Li-[Al]Beta (■) and Ni-Li-[Zn]Beta (●).

cations in Ni-H-[Al]Beta via C-H bond activation of ethene to form Ni-ethenyl-hydride intermediates [51]. DFT (BEEF-vdW) studies [59] at Ni^{2+} cations in Ni-AFI have also proposed that the reaction of two ethene molecules followed by deprotonation leads to formation of a framework H^+ site and a [Ni(II)-butenyl]$^+$ complex, which then transforms into an agostic [Ni(II)-butadiene-H]$^+$ complex that undergoes β-hydride elimination (chain transfer) with ethene to form 1,3-butadiene and a [Ni(II)-hydride-ethene]$^+$ intermediate. In contrast to the behavior observed on Ni-Li-[Al]Beta, the weak effects of ethene pressure (in the range studied) on the duration of the activation period measured on Ni-Li-[Zn]Beta (Figure 2.6) likely reflects the presence of a minority amount of exchanged Ni^{2+} cations that form hydride intermediates.

In order to determine if the activation transient reflects the formation of [Ni(II)-H]$^+$ intermediates, butenes site-time yields were measured on Ni-Li-[Al]Beta and Ni-Li-[Zn]Beta in the presence of co-fed H_2 and were compared to those measured in the absence of co-fed H_2. Butenes site-time yields were taken as the sum of those for 1-butene, cis-2-butene, trans-2-butene and isobutene (a secondary reaction product formed from linear butenes). Although the trace amounts of isobutene observed on Ni-Li-[Al]Beta suggest that minority H^+ sites are present that also catalyze ethene dimerization, their contributions to butenes site-time yields were assumed to be negligible, because initial site-time yields estimated (without co-fed H_2) at zero site-time on H-

[Al]Beta (453 K, per H^+, Table 2.11) are 20x lower than those measured on Ni-Li-[Al]Beta (453 K, per Ni, Section 2.6.13, Supporting Information). Also, the initial site-time yields measured on Ni-Li-[Zn]Beta (453 K, per Ni, Section 2.6.13, Supporting Information) are two orders of magnitude lower than those on Ni-Li-[Al]Beta, indicating that the grafted octahedral Ni^{2+} cations predominantly present on Ni-Li-[Zn]Beta (2196 cm^{-1} CO IR, Figure 2.1c) are less reactive than the exchanged, tetrahedral Ni^{2+} cations present on Ni-Li-[Al]Beta. It is plausible that the minority charge-compensating Ni^{2+} cations present (2222 cm^{-1} CO IR, Figure 2.1c) are precursors to the dominant dimerization active sites on Ni-Li-[Zn]Beta.

Figures 2.7a and 2.7b show the butenes site-time yield with time on stream for Ni-Li-[Al]Beta (0.05 kPa ethene, 453 K) and Ni-Li-[Zn]Beta (0.7 kPa ethene, 453 K), respectively, in the absence and presence of co-fed H_2 (5 kPa for Ni-Li-[Al]Beta and 7 kPa for Ni-Li-[Zn]Beta). In the absence of co-fed H_2, the butenes site-time yield on Ni-Li-[Al]Beta (Figure 2.7a) and Ni-Li-[Zn]Beta (Figure 2.7b) initially increased with time on stream during an activation period and

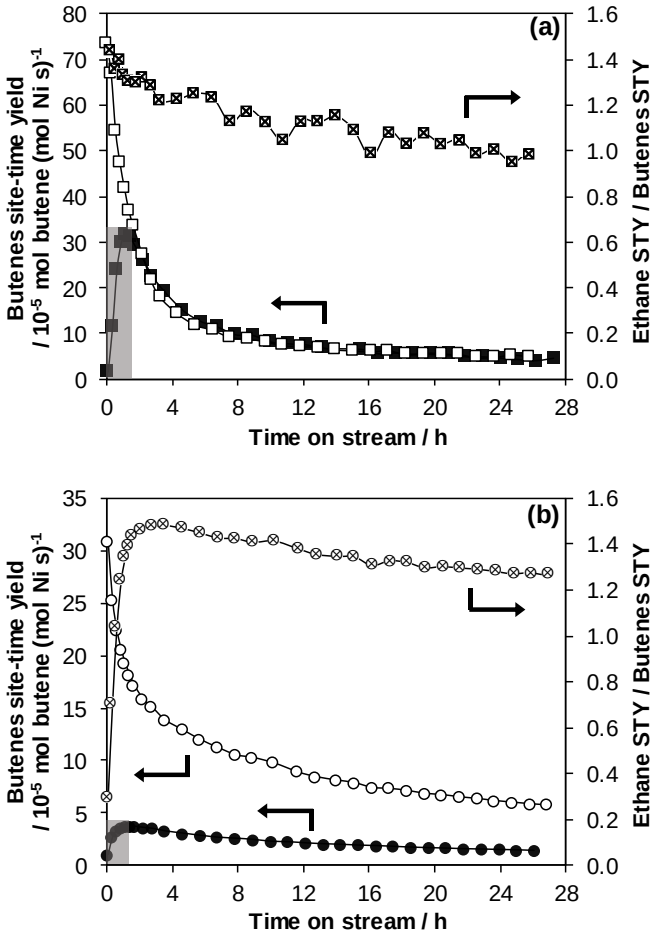

Figure 2.7. Butenes site-time yields at 453 K in the presence (hollow symbols) and absence (filled symbols) of H_2, and the ratio of site-time yields (STY) of ethane to butenes (symbols with cross), measured on (a) Ni-Li-[Al]Beta (■) at 0.05 kPa ethene, 11.1 s (mol ethene)$^{-1}$ mol Ni, 5 kPa H_2 and (b) Ni-Li-[Zn]Beta (●) at 0.7 kPa, 20 s (mol ethene)$^{-1}$ mol Ni, 7 kPa H_2. Lines are intended to guide the eye and the shaded region shows the activation period in absence of H_2.

then decreased during a deactivation period. A similar activation period was reported by Mlinar et. al [32] during initial reaction times for propene oligomerization on Ni-Na-[Al]X at 453 K, which was attributed to migration of Ni^{2+} cations from the hexagonal prisms of FAU to the sodalite cages and their coordination with propene to form a $[Ni(II)\text{-alkyl}]^+$ complex. Yet, this proposal seems unlikely for Ni^{2+} cations exchanged onto Beta frameworks that are located within 12-MR voids and accessible to alkene reactants. Further, in the presence of co-fed H_2, the activation transient was not observed for Ni-Li-[Al]Beta (Figure 2.7a) nor for Ni-Li-[Zn]Beta (Figure 2.7b), consistent with facilitated formation of $[Ni(II)\text{-H}]^+$ intermediates in the presence of H_2. Moreover, Ni-Li-[Al]Beta showed the same deactivation transient with and without co-fed H_2 after ~5 h of

time on stream (Figure 2.7a), indicating that a similar fraction of Ni^{2+} cations were transformed into active $[Ni(II)\text{-}H]^+$ intermediates in the presence and absence of H_2. In the case of Ni-Li-[Zn]Beta, butenes site-time yields were significantly higher in presence of hydrogen (Figure 2.7b), which we surmise resulted in the formation of an increased number of active $[Ni(II)\text{-}H]^+$ intermediates from spectator Ni^{2+} cations that are predominantly grafted in the framework Beta, or in the formation of Zn-hydride intermediates that could also be active for ethene dimerization.

Co-fed H_2 also resulted in the formation of ethane as a side product via ethene hydrogenation. The ratio of ethane-to-butenes site-time yields is shown on the secondary axes of Figures 2.7a and 2.7b for Ni-Li-[Al]Beta (0.05 kPa C_2H_4, 5 kPa H_2, 453 K) and Ni-Li-[Zn]Beta (0.7 kPa C_2H_4, 7 kPa H_2, 453 K), respectively. This site-time yield ratio initially increased with time on stream for Ni-Li-[Zn]Beta but not for Ni-Li-[Al]Beta, and decreased at longer times on stream to approach near unity values on both samples. This behavior is consistent with the presence of metal-hydride (Ni [122], Zn [123], Co [124]) intermediates, which have been reported to mediate alkene hydrogenation and alkane dehydrogenation cycles.

In order to further probe the formation of Ni-hydride intermediates in the presence of co-fed molecular hydrogen, H/D isotopic scrambling experiments were performed using different inlet H_2 and D_2 compositions at 453 K on Ni-Li-[Al]Beta and Ni-Li-[Zn]Beta, and on the Li-[Al]Beta, H-[Al]Beta and Li-[Zn]Beta control samples. Ni-Li-[Al]Beta (Figure 2.44, Supporting Information) and Ni-Li-[Zn]Beta (Figure 2.45, Supporting Information) samples statistically scrambled the isotopic content of inlet H_2-D_2 mixtures in the effluent HD products, which was verified by comparisons to isotopic equilibration achieved in analogous H_2-D_2 scrambling experiments performed on a 1% Pt/Al_2O_3 sample (pre-reduced using H_2, 673 K, 1 h) (Figure 2.43, Supporting Information). Such isotopic scrambling was not observed on the control samples that did not contain Ni species (Li-[Al]Beta, H-[Al]Beta, Li-[Zn]Beta; Figures 2.44 and 2.45, Supporting Information).

The number of Ni^{2+} sites that reversibly form $[Ni(II)\text{-}H]^+$ or $[Ni(II)\text{-}D]^+$ intermediates (at 453 K) was estimated from sequential H_2-D_2 exchange experiments performed on Ni-Li-[Al]Beta and Ni-Li-[Zn]Beta (details in Section 2.6.14.5, Supporting Information). Table 2.5 reports the amount of HD formed (per Ni site) on Ni-Li-[Al]Beta and Ni-Li-[Zn]Beta samples after each H_2/D_2 step change, after correcting for residual contributions from non-Ni sites measured on

Table 2.5. Quantification of nickel hydrides by H_2-D_2 exchange experiments at 453 K

Catalyst	mol HD (mol Ni)$^{-1}$		mol HD (mol Ni)$^{-1}$ (Average)
	$H_2 \rightarrow D_2$	$D_2 \rightarrow H_2$	
Ni-Li-[Al]Beta	0.92	0.85	0.87
	0.88	0.85	
	0.87	0.85	
Ni-Li-[Zn]Beta	0.32	0.32	0.31
	0.32	0.32	
	0.30	0.31	

corresponding Li-exchanged control samples (details in Section 2.6.14.6, Supporting Information). On average, the number of $[Ni(II)\text{-}H]^+$ intermediates was quantified to be 0.87 and 0.31 on Ni-Li-[Al]Beta and Ni-Li-[Zn]Beta, respectively (Table 2.5). The near unity value of 0.87 HD (per Ni) on Ni-Li-[Al]Beta reflects H-D exchange at nearly all Ni sites, which are predominantly present as exchanged Ni^{2+} cations (Sections 2.3.1 and 2.3.2). The sub-unity value of 0.30 HD (per Ni) on Ni-Li-[Zn]Beta reflects the presence of some grafted Ni^{2+} cations (Sections 2.3.1 and 2.3.2) that do not undergo H-D exchange under the conditions studied. Taken together, the H/D isotopic scrambling and H_2-D_2 exchange experiments provide quantitative evidence for the formation of $[Ni(II)\text{-}H]^+$ structures in presence of H_2 at 453 K, and provide justification for the elimination of activation transients on Ni-Li-[Al]Beta and Ni-Li-[Zn]Beta (Figure 2.7) in the presence of co-fed H_2.

2.4 Conclusions

Efforts to distinguish between metallacycle and coordination-insertion mechanisms for alkene dimerization catalyzed by Ni-based aluminosilicates are complicated, in part because residual H^+ sites on these supports also catalyze alkene dimerization and isomerization reactions. Ethene reaction pathways on Ni^{2+} cations and residual H^+ sites on aluminosilicate compositions of zeolite Beta were distinguished here by studying model materials that were prepared by

progressively poisoning or weakening the strength of residual H^+ sites to suppress their reactivity. Ni^{2+}-derived sites selectively catalyze ethene dimerization to form linear butenes, while the H^+ sites on aluminosilicate Beta also catalyze cracking, oligomerization, hydride transfer and skeletal isomerization of alkenes. Isobutene skeletal isomers of linear butenes were taken as a kinetic marker for the presence of residual H^+ sites, allowing discrimination of butene double bond isomerization pathways originating from H^+ and Ni^{2+}-derived sites. Double bond isomerization of 1-butene to 2-butene isomers occurred by secondary pathways on H^+ sites, but by primary reaction pathways on Ni^{2+}-derived sites, consistent with Ni-catalyzed coordination-insertion dimerization of ethene. Further, *in situ* X-ray absorption spectroscopy showed that Ni cations retained their +2 oxidation state during ethene dimerization, also consistent with coordination-insertion mechanism.

Ni^{2+} cations in Beta molecular sieves operate characteristically by the coordination-insertion mechanism of alkene dimerization in the absence of externally supplied activators or co-catalysts, although these are required to initiate coordination-insertion catalytic cycles in the case of α-diimine Ni complexes and Ni^{2+} cations supported on metal-organic frameworks. In the absence of external activators, an activation transient observed under dilute ethene conditions (<0.4 kPa) was eliminated by co-feeding H_2 to facilitate the *in-situ* formation of $[Ni(II)\text{-}H]^+$ species, which are the proposed active sites in the coordination-insertion mechanism. The H_2-assisted formation of $[Ni(II)\text{-}H]^+$ species was verified by H/D isotopic scrambling, and H_2-D_2 isotopic exchange experiments quantified the number of $[Ni(II)\text{-}H]^+$ intermediates formed. In the absence of H_2 and external activators, the duration of the activation transient decreased with increasing ethene pressures, indicating that active Ni^{2+}-derived intermediates in the coordination-insertion mechanism are likely formed *in situ* upon reaction with ethene.

Taken together, alkene double bond isomerization at Ni^{2+} cations by a primary reaction pathway, the +2 oxidation state of Ni cations during dimerization catalysis, and the formation of $[Ni(II)\text{-}H]^+$ active intermediates, provide incontrovertible evidence for the dominance of coordination-insertion mechanism, and not the metallacycle mechanism, as the origin of alkene dimerization on Ni-exchanged zeolites. This implies that kinetic, and not thermodynamic, factors influence isomer distributions within alkene dimer products, providing an opportunity to influence the selectivity towards α-olefin isomers that are the desired co-monomers in industrially practiced polymerization of ethene and propene [14]. Knowledge of the dominant reaction mechanism also

provides a framework to interpret the kinetic effects of varying other catalyst structural features, such as the confining void environments around Ni^{2+} cations.

2.5 Acknowledgements

Acknowledgment is made to the donors of the American Chemical Society Petroleum Research Fund for partial support of this research, under grant number 54216-DNI5. This work was also supported in part by the National Science Foundation under Cooperative Agreement No. EEC-1647722, an Engineering Research Center for the Innovative and Strategic Transformation of Alkane Resources (CISTAR). The use of Advanced Photon Source to obtain the XAS results is supported by the U.S. Department of Energy, Office of Science, and Office of Basic Energy Sciences, under Contract DE-AC02-06CH11357. MRCAT operations are supported by the Department of Energy and the MRCAT member institutions. We also thank Prof. Peter Stair (Northwestern) for helpful technical discussions.

2.6 Supporting Information

2.6.1 Synthesis of control sample NiO/Si-Beta-F

The NiO/Si-Beta-F control sample was synthesized to detect the IR feature for CO adsorbed on NiO nanoparticles, which can be invisible to other bulk characterization techniques such as XRD or XAS for small particles. First, a Si-Beta-F support was synthesized by using a reported hydrothermal synthesis procedure [125]. 29.35 g of ultrapure water (18.2 MΩ-cm) was added to 20.47 g of tetraethylammonium fluoride dihydrate (TEAF, Alfa Aesar, 97% pure), followed by addition of 41.42 g of tetraethylorthosilicate (TEOS, Sigma Aldrich, 98% pure). The mixture was covered and stirred for 24 h under ambient conditions to completely hydrolyze TEOS. Then, the mixture was uncovered and kept stirring for another 6-7 h to completely evaporate ethanol, which also evaporated some water. Finally, water was re-added to achieve the molar composition of 1 SiO_2/0.55 TEAF/7.25 H_2O. The gel was then transferred to Teflon-lined, stainless steel autoclaves and was heated statically at 413 K for 7 days. The product was collected by centrifugation, washed with ultrapure water and acetone, and then dried overnight in a drying oven

at 363 K. The dried product was treated in a muffle furnace (Nabertherm LE 6/11/P300) at 853 K (0.0167 K s^{-1}) in air (20 cm^3 s^{-1} g-cat^{-1}, 99.999% UHP, Matheson Tri-Gas) for 10 h.

The NiO nanoparticles were supported on Si-Beta-F by incipient wetness impregnation. 1 g of Si-Beta-F support was introduced into a small crystallizing dish and gradually added with drops of 0.273 M $Ni(NO_3)_2$ solution, while stirring the solid continuously. A total of 1 mL solution of 0.273 M $Ni(NO_3)_2$ was added, while taking precaution that the solution is directly introduced to contact the support and not the sides of the crystallizing dish. The crystallizing dish was then covered by an aluminum foil and a stream of flowing air was introduced over it to facilitate drying of the solid, overnight. The dried product was treated in the muffle furnace at 773 K (0.0167 K s^{-1}) in air (20 cm^3 s^{-1} g-cat^{-1}, 99.999% UHP, Matheson Tri-Gas) for 4 h.

2.6.2 Structural characterization of Beta molecular sieves

2.6.2.1 Powder X-ray diffraction

The crystal morphology of solid samples was determined by powder X-ray diffraction patterns (XRD) collected using a Rigaku SmartLab X-ray diffractometer equipped with an ASC-6 automatic sample changer and a Cu Kα x-ray source (λ = 0.154 nm) operated at 1.76 kW.

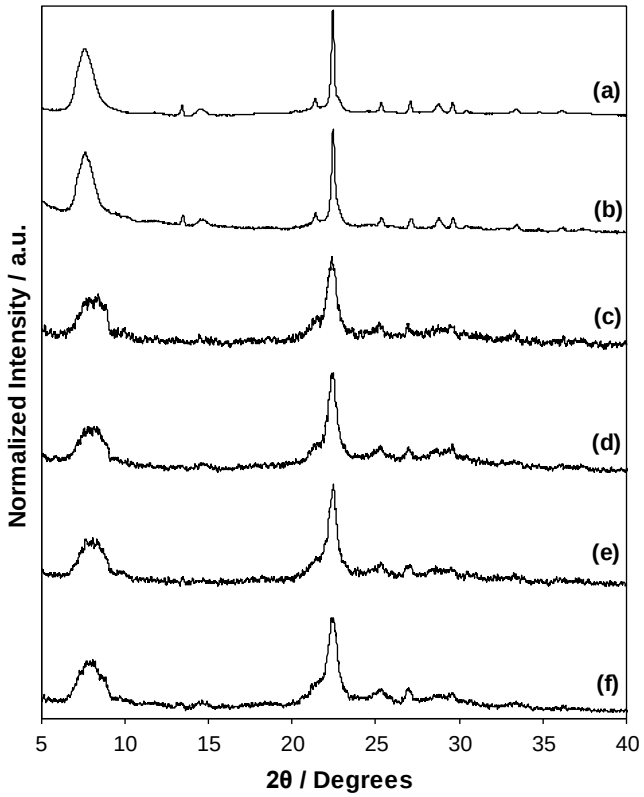

Figure 2.8. XRD patterns of a) Ni-Li-[Zn]Beta, b) Li-[Zn]Beta, c) Ni-Li-[Al]Beta, d) Li-[Al]Beta, e) Ni-H-[Al]Beta and f) H-[Al]Beta

Typically, 0.01 g of sample were loaded into a zero background, low dead volume sample holders (Rigaku) and diffraction patterns were collected from 4-90° 2θ at a scan rate of 0.0125° s^{-1} with a step size of 0.01°.

Figure 2.8 shows the powder XRD patterns collected for all aluminosilicate and zincosilicate Beta samples. The powder XRD patterns were consistent with the diffraction pattern for Sn-Beta (BEA*) reported in the International Zeolite Association (IZA) structure database [126], which confirmed Beta framework topology for all samples.

2.6.2.2 Micropore volume measurement using N_2 adsorption

The micropore volumes of solid samples were determined from N_2 (77 K) adsorption isotherms measured using Micromeritics ASAP2020 Surface Area and Porosity Analyzer. Typically, 0.04 g of the solid sample were pelleted and sieved to retain particles between 180 and

250 μm in diameter. Prior to adsorption measurements, the samples were degassed by heating under vacuum (~5 μm Hg) to 393 K for 2 h and 623 K for 8 h.

Figures 2.9 and 2.10 show N_2 adsorption isotherms (77 K) measured on aluminosilicate and zincosilicate Beta samples, respectively; isotherms are offset by 400 cm^3 g^{-1} for clarity. Micropore volumes were determined from a semi-log derivative analysis of N_2 adsorption isotherms ($\partial(V_{ads}/g)/\partial(\log(P/P_0)$ vs. $\log (P/P_0)$), where the first maximum represents the micropore filling transition and the subsequent minimum represents the end of micropore filling. Table 2.6 shows the micropore volumes determined from N_2 adsorption (77 K) to be 0.19 – 0.20 cm^3 g^{-1} for all samples, consistent with the Beta topology

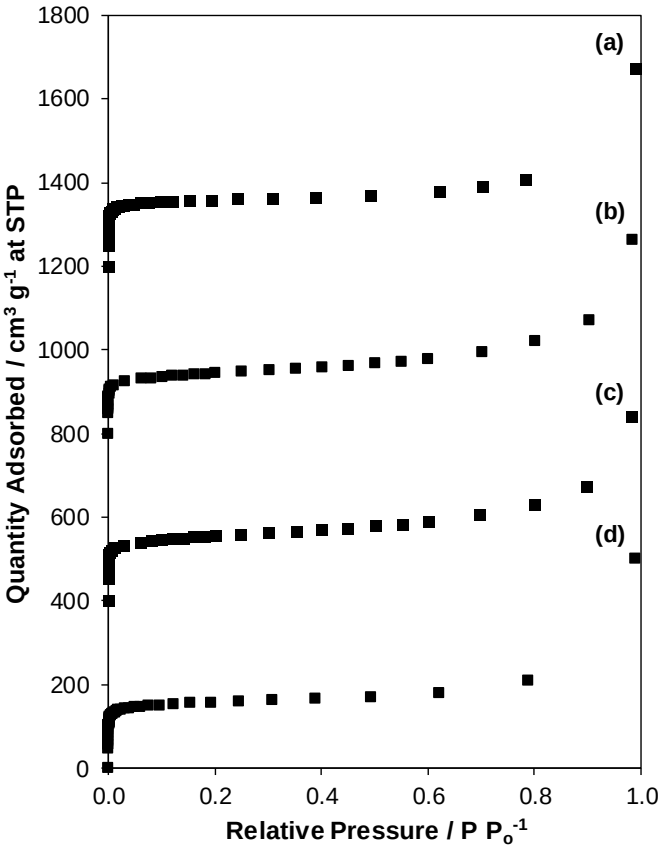

Figure 2.9. N_2 adsorption isotherms (77 K) measured on a) Ni-Li-[Al]Beta, b) Li-[Al]Beta, c) Ni-H-[Al]Beta, and d) H-[Al]Beta.

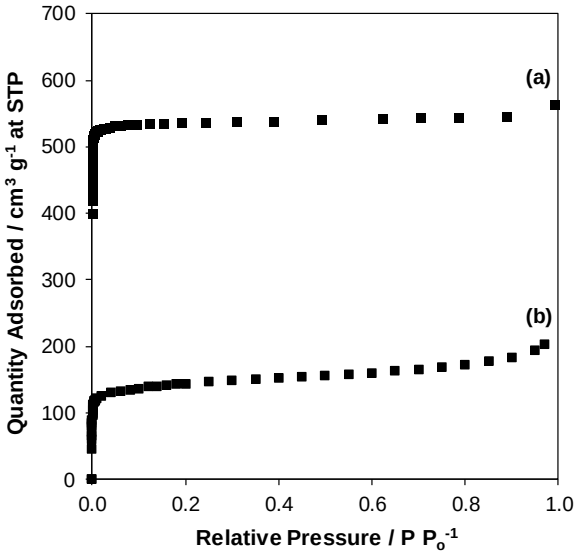

Figure 2.10. N_2 adsorption isotherms (77 K) measured on a) Ni-Li-[Zn]Beta, and b) Li-[Zn]Beta.

Table 2.6. Micropore volumes of aluminosilicate and zincosilicate Beta samples determined from N_2 adsorption isotherms

Sample	Micropore volume / $cm^3\ g^{-1}$
H-[Al]Beta	0.20
Ni-H-[Al]Beta	0.19
Li-[Al]Beta	0.19
Ni-Li-[Al]Beta	0.20
Li-[Zn]Beta	0.19
Ni-Li-[Zn]Beta	0.20

2.6.2.3 Elemental analysis using Atomic Absorption Spectroscopy (AAS)

Bulk elemental compositions of catalysts were determined using atomic absorption spectroscopy (AAS) performed with a Perkin Elmer AAnalyst 300 Atomic Absorption Spectrometer. Samples were prepared by dissolving 0.02 g of catalyst in 3 g of hydrofluoric acid (48 wt. %, Sigma-Aldrich) overnight, and then diluting with 50 g of ultrapure water (18.2 MΩ). Additional dilution was required for Ni, Li and Zn measurements. 1000 ppm AAS standards (Sigma-Aldrich, TraceCERT, +/- 4 ppm) for each metal were diluted to create calibration standards, and the instrument was calibrated for each element prior to the measurements.

Absorbances were measured in a reducing acetylene/nitrous oxide flame for Si and Al at wavelengths of 251.6 nm and 308.2 nm, respectively, while in an oxidizing acetylene/air flame for Li, Ni and Zn at wavelengths 670.8, 232.0 and 213.9 nm, respectively. The Si/Al ratios were determined using the Al weight fraction together with the unit cell formula for zeolite Beta. The results of elemental analysis for H-[Al]Beta, Ni-H-[Al]Beta, Li-[Al]Beta, Ni-Li-[Al]Beta, Li-[Zn]Beta and Ni-Li-[Zn]Beta are summarized in Table 2.1 in the main text.

2.6.2.4 Quantification of H^+ sites by NH_3 TPD

The number of H^+ sites on H-[Al]Beta was quantified by NH_3 temperature-programmed desorption (TPD) following aqueous ion-exchange with a NH_4NO_3 solution. The number of residual H^+ sites on Ni-H-[Al]Beta was quantified by NH_3 TPD following saturation with gaseous NH_3 and purging treatments that remove all non-Brønsted bound NH_3, as reported in detail elsewhere [127, 128]. The TPD experiments were carried out using a Micromeritics Autochem II 2920 Chemisorption analyzer connected to an Agilent 5973N mass selective detector (MSD). The H^+/Al values for H-[Al]Beta and Ni-H-[Al]Beta are shown in Table 2.1 in the main text.

2.6.2.5 Thermogravimetric (TGA) and Differential Scanning Calorimetry (DSC) Analysis

Thermogravimetric (TGA) and differential scanning calorimetry (DSC) analysis was performed using TA Instruments SDT Q600 with a dry air flow of 111 $cm^3\ s^{-1}\ g^{-1}$ and temperature ramp of 10 K min^{-1} from 303 K to 1173 K, to determine the organic content of as-made Li-[Zn]Beta and the moisture or water content of all other samples.

Figure 2.11 shows the TGA-DSC results for the as-made Li-[Zn]Beta sample. The weight loss caused by combustion of TEA^+ cations was 17% and occurred between 444 and 1100 K. This corresponded to approximately TEA^+/Zn = 1, indicating a H^+/Zn ratio of 1 for Li-[Zn]Beta sample after combustion of TEA^+ cations during air treatment.

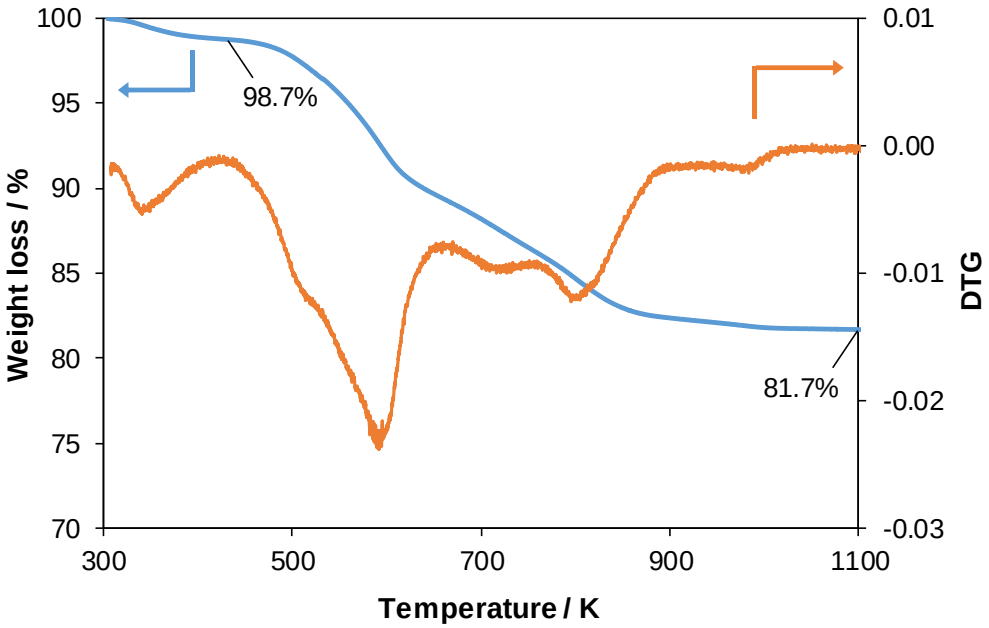

Figure 2.11. Thermogravimetric analysis of as-made Li-[Zn]Beta sample showing weight loss and DTG (differential weight loss) curves**.**

The water content of H-[Al]Beta, Ni-H-[Al]Beta, Li-[Al]Beta, Ni-Li-[Al]Beta, Li-[Zn]Beta (without organic TEA^+), Ni-Li-[Zn]Beta and NiO/Si-Beta-F samples was determined from the weight loss that occurred between 300 and 1173 K and is shown in Table 2.7.

Table 2.7. Water content of aluminosilicate and zincosilicate Beta samples determined by weight loss from thermogravimetric analysis.

Sample	Water / wt. %
H-[Al]Beta	14.36
Ni-H-[Al]Beta	15.10
Li-[Al]Beta	10.79
Ni-Li-[Al]Beta	12.78
NiO/Si-Beta-F	0.57
Li-[Zn]Beta	9.94
Ni-Li-[Zn]Beta	5.92

2.6.2.6 ^{27}Al MAS NMR measurements for [Al]Beta samples

^{27}Al magic angle spinning nuclear magnetic resonance (MAS NMR) spectra were recorded to determine the fraction of framework and extraframework Al for H-[Al]Beta and Li-[Al]Beta samples. Prior to the measurement, the samples were hydrated in a desiccator containing a saturated potassium chloride (KCl) solution for >48 h and then packed in a 4 mm ZrO_2 rotor. Spectra were collected at 104.24 MHz and a MAS rate of 5 kHz under ambient conditions using a Chemagnetics CMX-Infinity 400 spectrometer in a wide-bore 9.4 Tesla magnet (Purdue Interdepartmental NMR Facility) with a 2.3 μs pulse (equivalent to ca. 30°), a 12.8 ms of acquisition time, and a relaxation delay of 1s. A two-pulse phase modulation (TPPM) scheme and ^{1}H decoupling was used during the acquisition. All spectra were referenced to a static sample of $AlCl_3$ dissolved in D_2O (0 ppm ^{27}Al line). Figure 2.12 shows ^{27}Al MAS NMR spectra of H-[Al]Beta and Li-[Al]Beta samples normalized by setting the maximum intensity within each spectrum to unity.

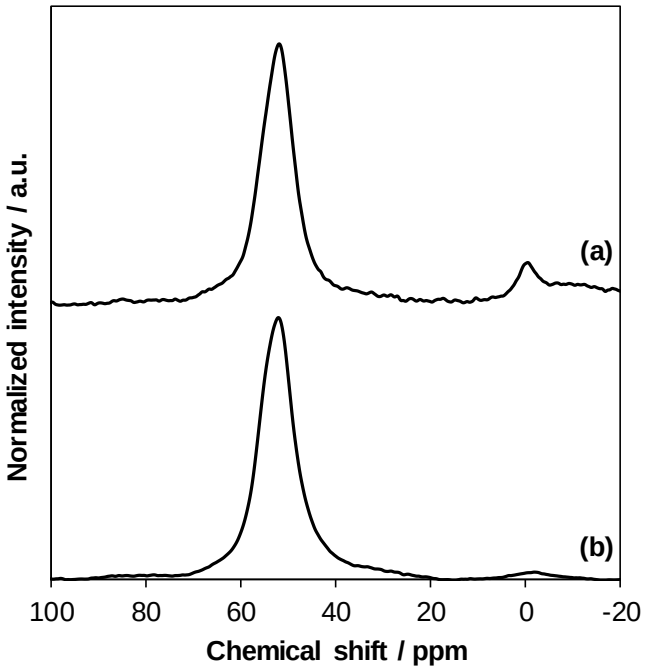

Figure 2.12. ^{27}Al MAS NMR spectra of a) H-[Al]Beta and b) Li-[Al]Beta.

2.6.2.7 SEM images

Scanning electron microscopy (SEM) images were taken in a FEI Quanta 3D FEG Dual-beam SEM with an Everhart-Thornley attachment for high vacuum imaging. Images were captured using a focused beam mode at 10.0 kV and spot size of 4 μm.

During hydrothermal synthesis, the Li-[Zn]Beta (CIT-6) crystals can undergo a solid-state phase transformation to VET framework (VPI-8) at long crystallization times [129], and thus change the crystal morphology. To verify if the transformation to VET phase has not occurred, an SEM image was acquired for as-made Li-[Zn]Beta sample, as shown in Figure 2.13. The SEM image (Figure 2.13) showed predominantly pseudo-cubic or rounded shaped Beta crystals, and only traces of needle shaped VET crystals, suggesting a pure Beta phase.

We do not report SEM images for the Zeolyst samples here, but note that the SEM image of the Zeolyst NH_4-[Al]Beta sample can be found in Figure S4 of the Supporting Information in Dusselier et al. [130].

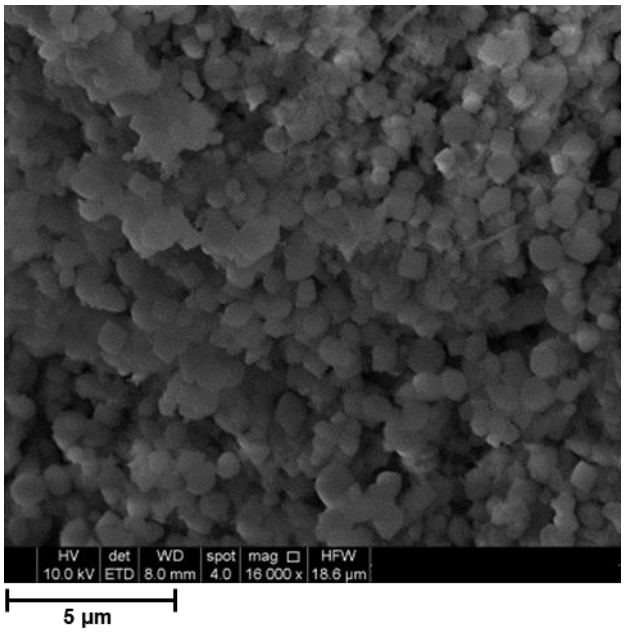

Figure 2.13. SEM image for as-made Li-[Zn]Beta.

2.6.3 Site titration methods for [Al]Beta samples

2.6.3.1 Nickel ion-exchange for H-[Al]Beta

Figure 2.14 shows nickel exchange isotherm (294 K) obtained by equilibrating H-[Al]Beta samples with aqueous $Ni(NO_3)_2$ solutions of increasing molarity, without pH adjustment. Nickel was exchanged as isolated Ni^{2+} cations with Langmuirian adsorption behavior up to Ni/Al_{tot} saturation value of ~ 0.2, similar to the Co/Al_{tot} saturation value as shown in Figure 2.15.

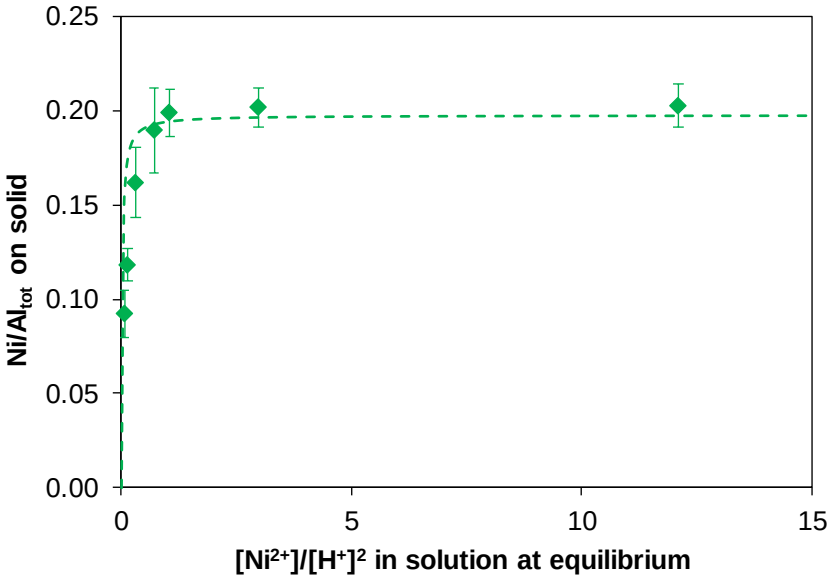

Figure 2.14. Nickel exchange isotherm for H-[Al]Beta at 348 K. Dashed line represents least square regression fit of data to a Langmuirian isotherm.

2.6.3.2 Cobalt ion-exchange for H-[Al]Beta

Figure 2.15 shows cobalt exchange isotherm (294 K) obtained by equilibrating H-[Al]Beta samples with aqueous $Co(NO_3)_2$ solutions of increasing molarity, without pH adjustment. Cobalt was exchanged as isolated Co^{2+} cations with Langmuirian adsorption behavior until Co/Al_{tot} saturation value of ~ 0.2.

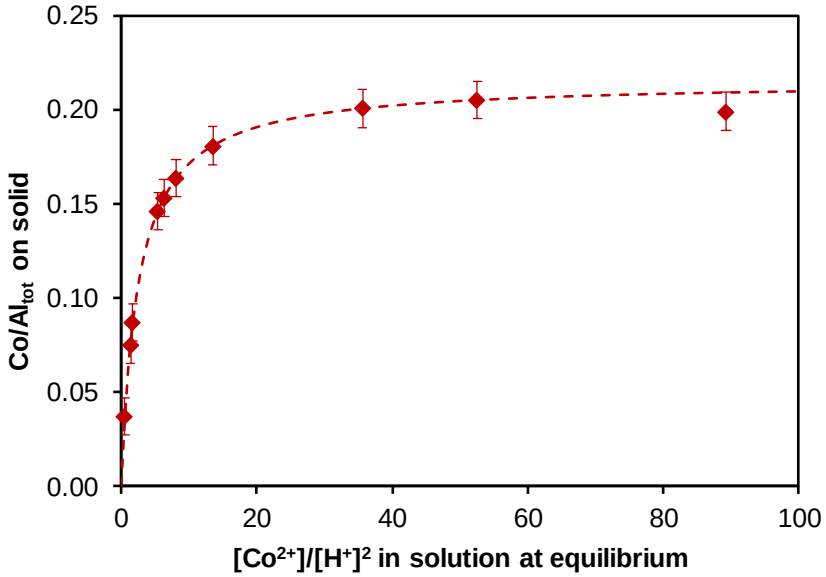

Figure 2.15. Cobalt exchange isotherm for H-[Al]Beta at 294 K. Dashed line represents least square regression fit of data to a Langmuirian isotherm.

The presence of isolated Co^{2+} cations was further supported by UV-vis DR spectra collected for these samples under ambient conditions, as shown in Figure 2.16. The peak area of d-d transition features (~19000 cm^{-1}) for hydrated Co^{2+} cations increased with increasing Co loading, and the area remained constant for samples with Co/Al_{tot} value of ~ 0.2.

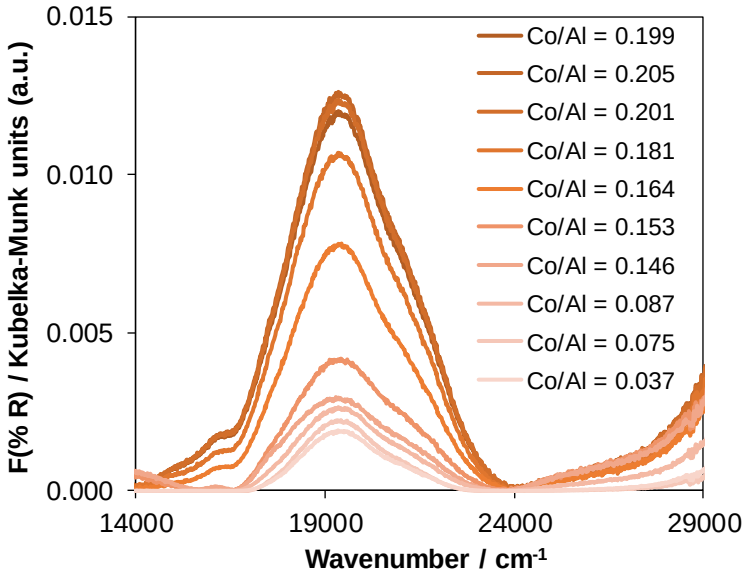

Figure 2.16. Diffuse reflectance UV-vis spectra collected under ambient conditions for H-[Al]Beta samples with increasing Co^{2+} content (light to dark).

2.6.3.3 Cobalt ion-exchange for NH_4-[Al]Beta

Figure 2.17 shows the cobalt exchange isotherm (294 K) obtained by equilibrating NH_4-[Al]Beta samples with aqueous $Co(NO_3)_2$ solutions of increasing molarity, without pH adjustment. The Co/Al_{tot} value reached a saturation value of ~ 0.35.

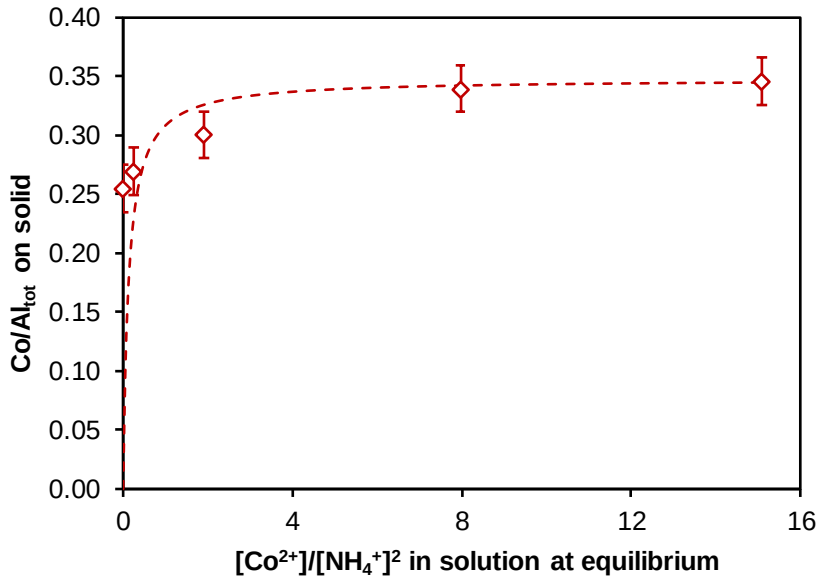

Figure 2.17. Cobalt exchange isotherm for NH_4-[Al]Beta at 294 K. Dashed line represents least square regression fit of data to a Langmuirian isotherm.

2.6.4 Spectroscopic and analytical characterization of control samples

2.6.4.1 CO infrared spectroscopy on H-[Al]Beta

Figure 2.18 shows infrared spectra for H-[Al]Beta sample with CO dosed sequentially at 85 K. CO was observed to preferentially adsorb on Brønsted acid sites as the absorption feature at 2174 cm^{-1} preferentially grew with increase in amounts of CO dosed. At higher amounts of CO, the absorption features at 2133 and 2141 cm^{-1} indicated physisorbed CO. The small shoulders observed at 2166 and 2160 cm^{-1} corresponded to CO adsorbed on Al-OH groups [95] and silanols [98], respectively.

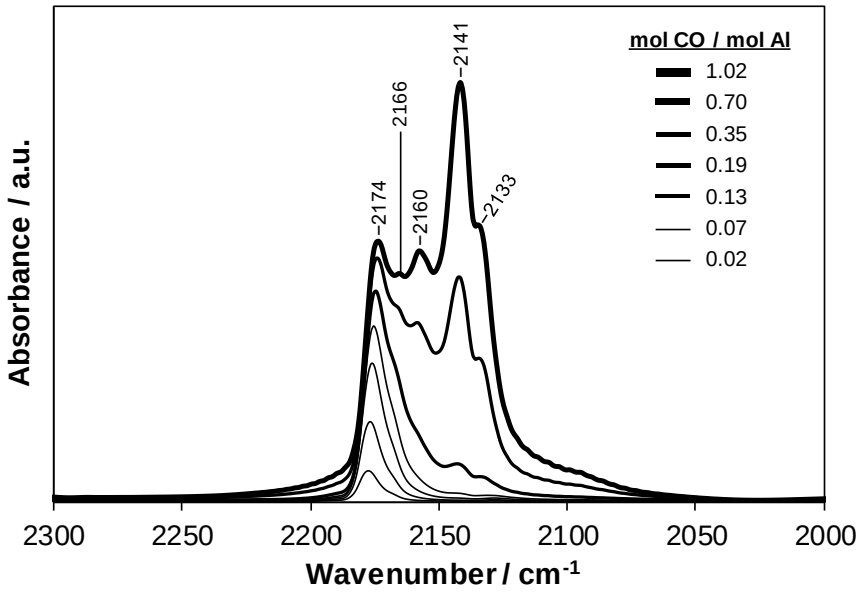

Figure 2.18. Infrared difference spectra (relative to empty surface) with increasing amounts of CO dosed at 85 K on H-[Al]Beta.

2.6.4.2 CO infrared spectroscopy on Li-[Al]Beta

Figure 2.19 shows infrared spectra for Li-[Al]Beta sample with CO dosed sequentially at 85 K. At low CO coverages (CO/Al < 0.5), no feature was observed at 2175 cm^{-1} like H-[Al]Beta, suggesting absence of residual Brønsted acid sites. In contrast, a predominant absorption feature was observed at 2185 cm^{-1}, which was assigned to CO bonded to Li^{+} cations.[131] At high CO coverages (CO/Al > 0.5), the absorption peaks at 2133 and 2141 cm^{-1} suggested presence of physisorbed CO.[89, 99] Also, the shoulders at 2160 cm^{-1} and 2174 cm^{-1}, and the small feature at 2199 cm^{-1} indicated CO bonded to silanol groups,[98] hydrogen bonded CO and framework Lewis acidic Al^{3+} centers,[99] respectively.

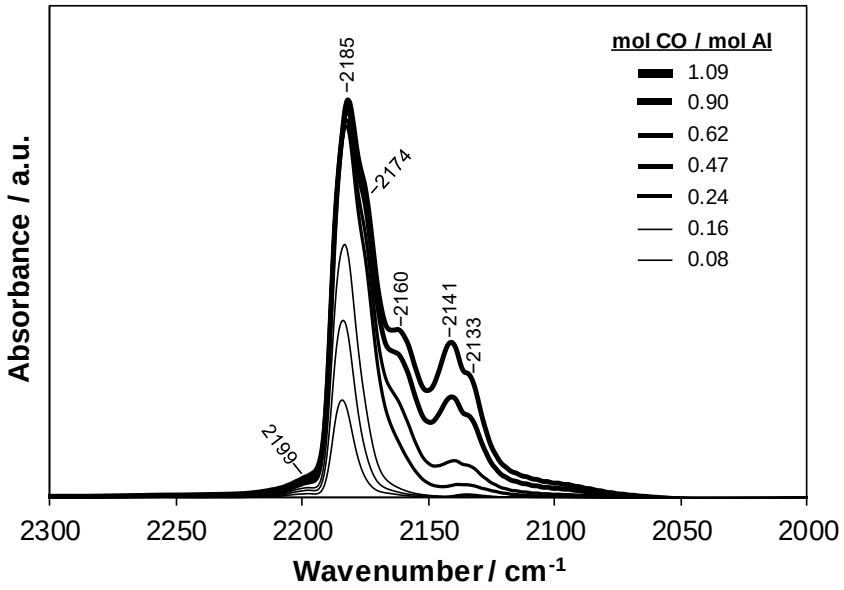

Figure 2.19. Infrared difference spectra (relative to empty surface) with increasing amounts of CO dosed at 85 K on Li-[Al]Beta**.**

2.6.4.3 CO infrared spectroscopy on NiO/Si-Beta-F

Figure 2.20 shows infrared spectra for NiO/Si-Beta-F sample with CO dosed sequentially at 85 K. The absorption peak at 2155 cm^{-1} showed CO bonded to NiO nanoparticles [31, 92] and the absorption peaks at 2133 and 2141 cm^{-1} correspond to physisorbed CO [89, 99]. The NiO absorption peak was detected only after appearance of the physisorbed CO peak, indicating weak binding of CO to NiO nanoparticles. The broad features around 2115 cm^{-1} and 2181 cm^{-1} represented gaseous CO [132].

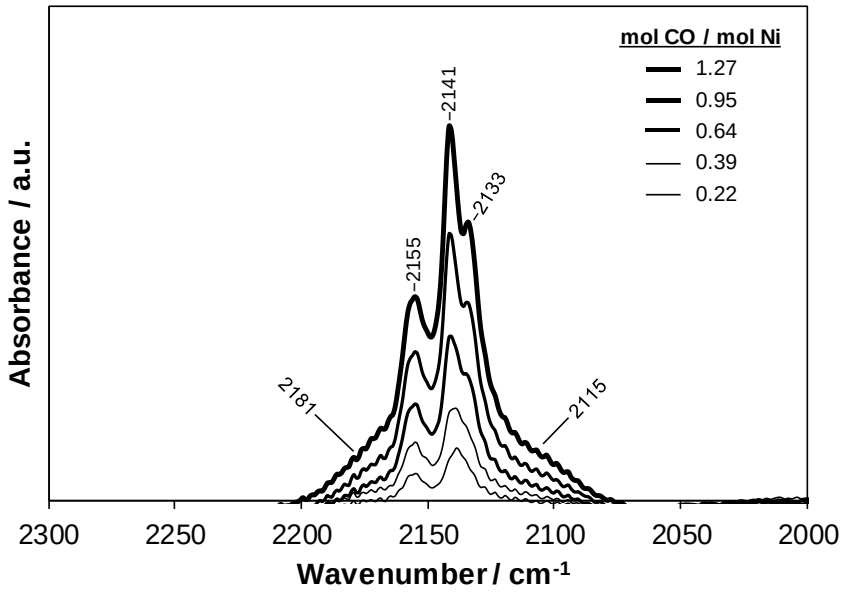

Figure 2.20. Infrared difference spectra (relative to empty surface) with increasing amounts of CO dosed at 85 K on NiO/Si-Beta-F.

2.6.4.4 CO infrared spectroscopy on Li-[Zn]Beta

The presence of H^+ sites on Li-[Zn]Beta was confirmed by CO adsorbed infrared spectroscopy. Figure 2.21 shows infrared spectra for CO dosed sequentially on Li-[Zn]Beta till the features for physisorbed CO appeared at 2133 and 2141 cm^{-1}. The feature at 2194 cm^{-1} was assigned to CO adsorbed on Lewis acidic framework Zn^{2+} sites analogous to [Al]Beta [99]. The 2185 cm^{-1} and 2160 cm^{-1} bands were respectively assigned to CO bonded to Li^+ cations and silanol groups, similar to Li-[Al]Beta (Figure 2.19). The 2176 cm^{-1} absorption band represented CO bonded to acidic bridging hydroxyl groups or Brønsted acid sites, known from the literature on aluminosilicates [89, 95, 98, 99]. The band at 2170 cm^{-1} was assigned to CO adsorbed on Zn-OH groups analogous to the feature observed at 2165 cm^{-1} for CO interacting with Al-OH groups on [Al]Beta [95].

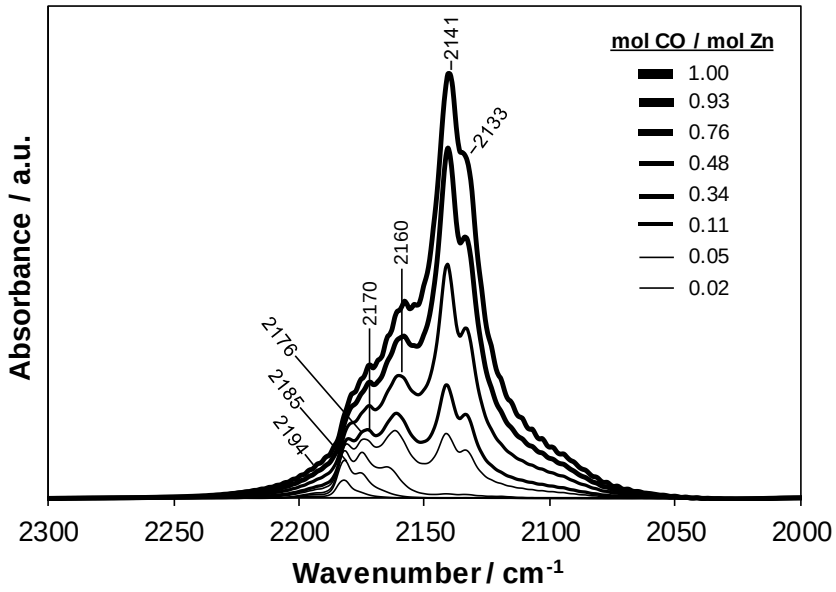

Figure 2.21. Infrared difference spectra (relative to empty surface) with increasing amounts of CO dosed at 85 K on Li-[Zn]Beta**.**

2.6.4.5 Pyridine infrared spectroscopy on Li-[Zn]Beta

Pyridine adsorbed infrared spectroscopy was performed on Li-[Zn]Beta to determine if the Brønsted acid sites differ in their acid strength relative to H-[Al]Beta. Figure 2.22 shows evolution of infrared spectra for successive doses of pyridine on Li-[Zn]Beta at 423 K. The absorption bands for pyridine bound to Lewis acid sites were observed at 1451 cm^{-1} and 1610 cm^{-1} [133-135], and the feature at 1491 cm^{-1} indicated ring stretches of pyridine coordinated to Lewis acid sites or pyridine protonated at Brønsted acid sites [133-135]. The absorption bands observed at 1446 cm^{-1} and 1575 cm^{-1}, indicated hydrogen bonded physisorbed pyridine [134, 135], while the band at 1600 cm^{-1} suggested presence of gas phase pyridine. The characteristics IR features for protonated pyridine at 1550 and 1637 cm^{-1} [133, 134, 136, 137], however, were absent, consistent with the findings of Orazov et al. [88]. Thus, the Brønsted acid sites present on Li-[Zn]Beta were weak in strength to protonate pyridine, unlike those on H-[Al]Beta. Thus, we conclude that the Brønsted acid sites on Li-[Zn]Beta have relatively low acid strength compared to those on H-[Al]Beta.

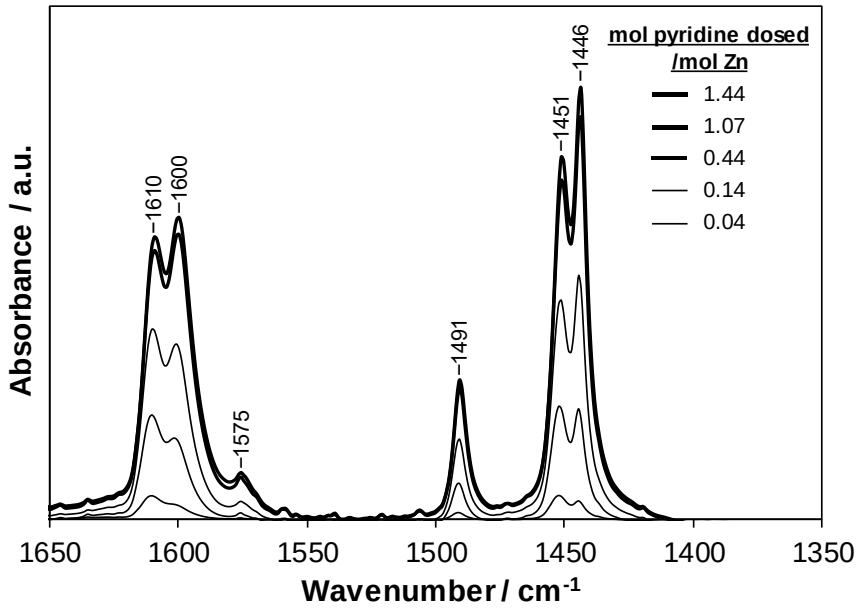

Figure 2.22. Infrared difference spectra (relative to empty surface) for successive pyridine doses on Li-[Zn]Beta at 423 K**.**

2.6.4.6 DR UV-vis spectroscopy on Li-[Zn]Beta

Figure 2.23 shows the diffuse reflectance UV-visible spectrum in the 200-500 nm region for the Li-[Zn]Beta sample collected at ambient temperature after dehydration in flowing dry air at 673 K (1 h). The predominant absorption feature at 270 nm is indicative of framework tetrahedral atoms and no peak was observed in the region 350-400 nm for non-framework zinc oxide [138].

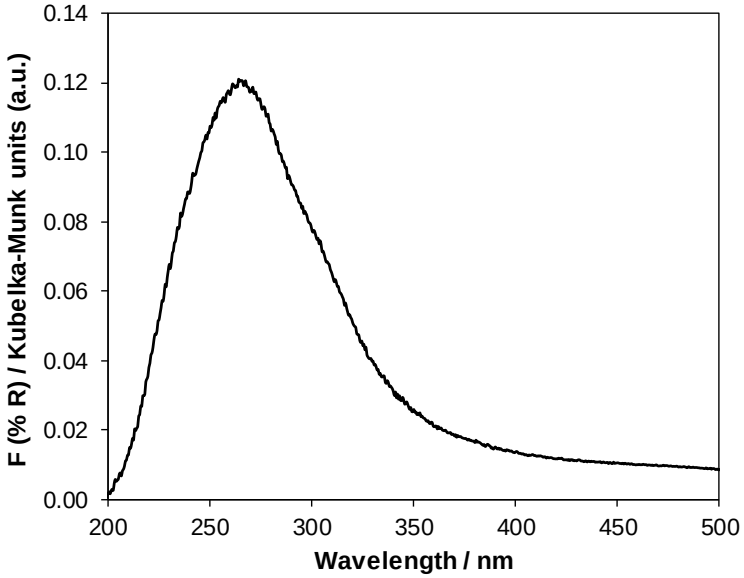

Figure 2.23. Diffuse reflectance UV-vis spectra collected under dehydrated conditions for Li-[Zn]Beta at ambient temperature.

2.6.5 Elemental balance for nickel template ion-exchange of Li-[Zn]Beta

To determine the exchange stoichiometry between Li^+ and Ni^{2+} cations during template ion-exchange procedure, elemental composition was determined for Li-[Zn]Beta, starting $Ni(NO_3)_2$ solution, resulting Ni-Li-[Zn]Beta and the supernatant $Ni(NO_3)_2$ solution at the end of exchange procedure, as shown in Table 2.8. The moles of Li^+ cations detected in the supernatant solution were approximately twice the moles of Ni^{2+} cations on the resulting Ni-Li-[Zn]Beta. This suggested a 2:1 ion-exchange stoichiometry between Li^+ and Ni^{2+} cations during the template ion-exchange procedure.

Table 2.8. Nickel and lithium elemental composition for Li-[Zn]Beta, Ni-Li-[Zn]Beta, starting $Ni(NO_3)_2$ solution and supernatant $Ni(NO_3)_2$ solution for one specific experiment[†].

Element	Before ion-exchange		After ion-exchange	
	Li-[Zn]Beta	Starting $Ni(NO_3)_2$ solution	Ni-Li-[Zn]Beta	Supernatant $Ni(NO_3)_2$ solution
Moles Ni	0	4.93E-04	1.07E-04	2.44E-04
Moles Li	2.93E-04	0	8.00E-05	1.97E-04

[†]The experiment involved contacting 0.5 g of Li-[Zn]Beta sample with 49 mL solution of 0.01 M $Ni(NO_3)_2$ at 348 K for 5 h

2.6.6 X-ray absorption characterization of nickel

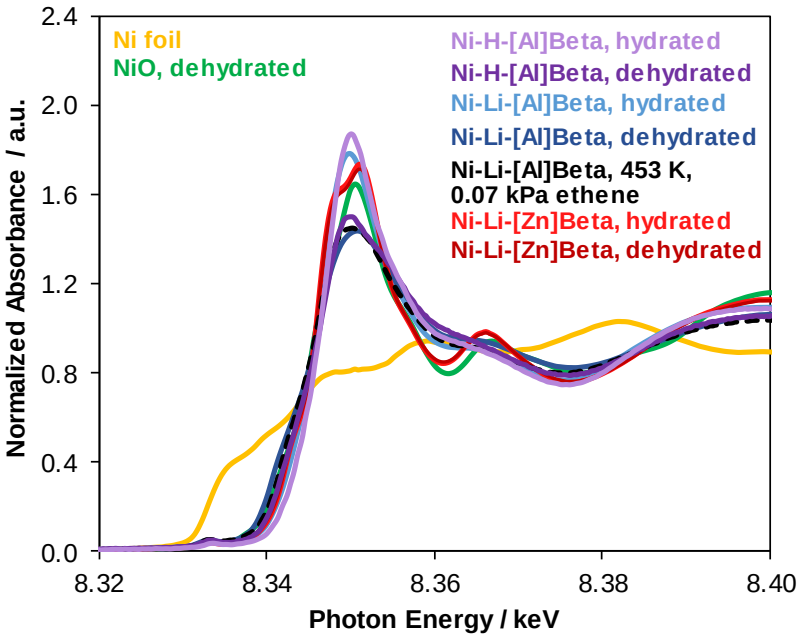

Figure 2.24. XANES spectra for Ni-H-[Al]Beta, Ni-Li-[Al]Beta and Ni-Li-[Zn]Beta samples under hydrated and dehydrated conditions, and during ethene dimerization (453 K, 0.07 kPa ethene) for Ni-Li-[Al]Beta. NiO and Ni foil are used as reference materials.

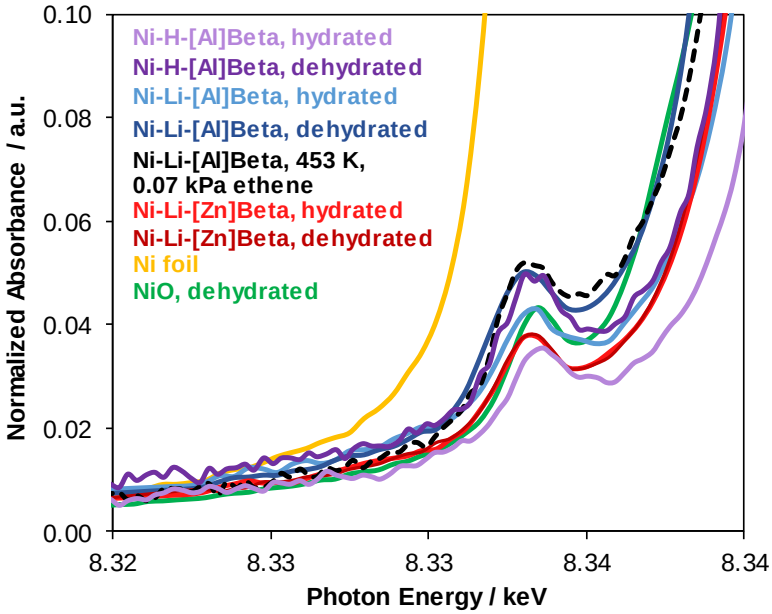

Figure 2.25. XANES spectra around pre-edge region for Ni-H-[Al]Beta, Ni-Li-[Al]Beta and Ni-Li-[Zn]Beta samples under hydrated and dehydrated conditions, and during ethene dimerization (453 K, 0.07 kPa ethene) for Ni-Li-[Al]Beta. NiO and Ni foil are used as reference materials.

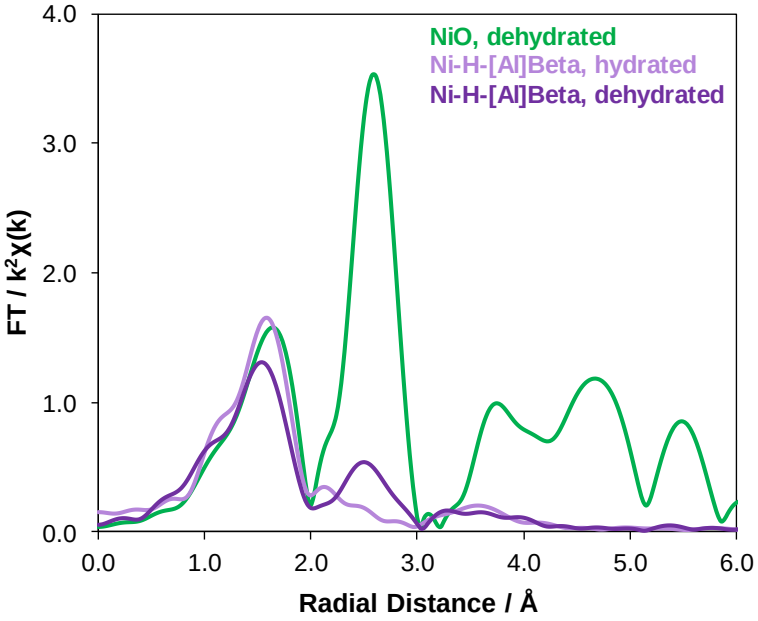

Figure 2.26. EXAFS for Ni-H-[Al]Beta sample under hydrated and dehydrated conditions, and for NiO (reference material).

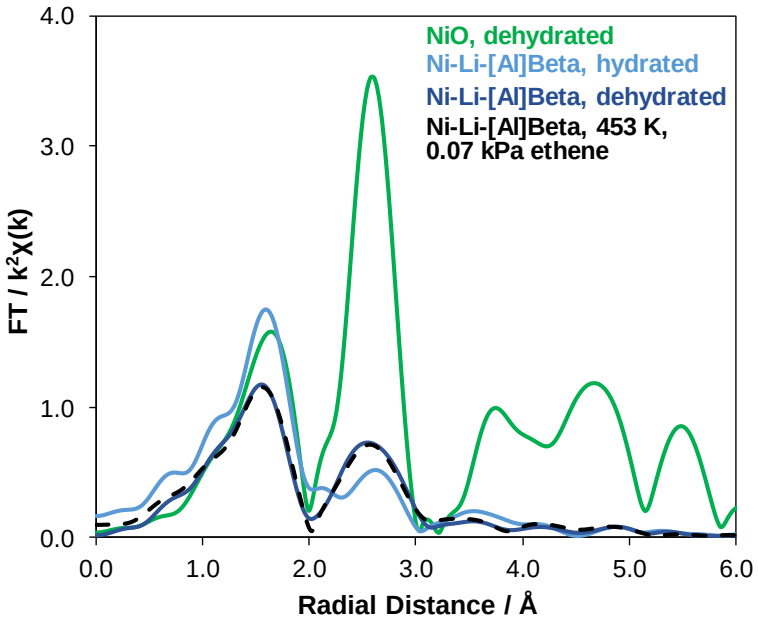

Figure 2.27. EXAFS for Ni-Li-[Al]Beta sample under hydrated, dehydrated conditions, and during ethene dimerization (453 K, 0.07 kPa ethene), and for NiO (reference material).

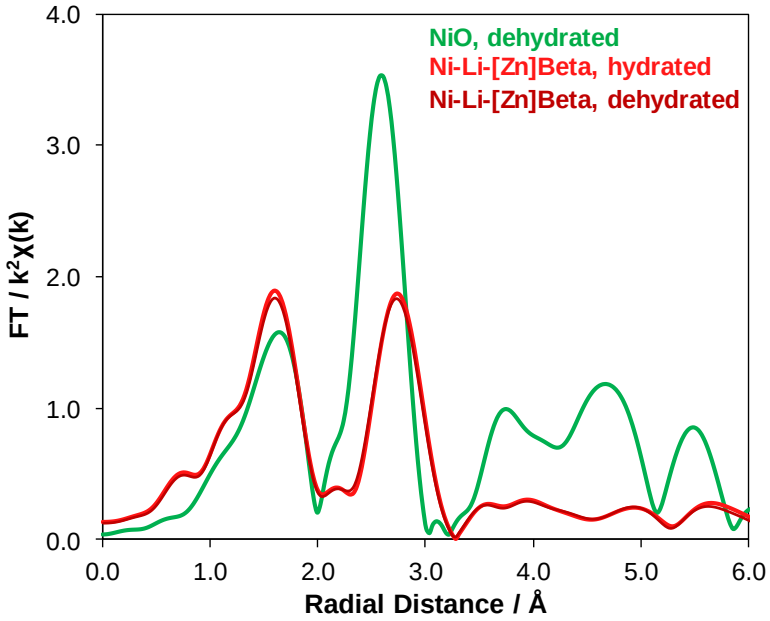

Figure 2.28. EXAFS for Ni-Li-[Zn]Beta sample under hydrated and dehydrated conditions, and for NiO (reference material)**.**

2.6.7 Ethene conversion as a function of reaction time at 453 K and 0.4 kPa ethene

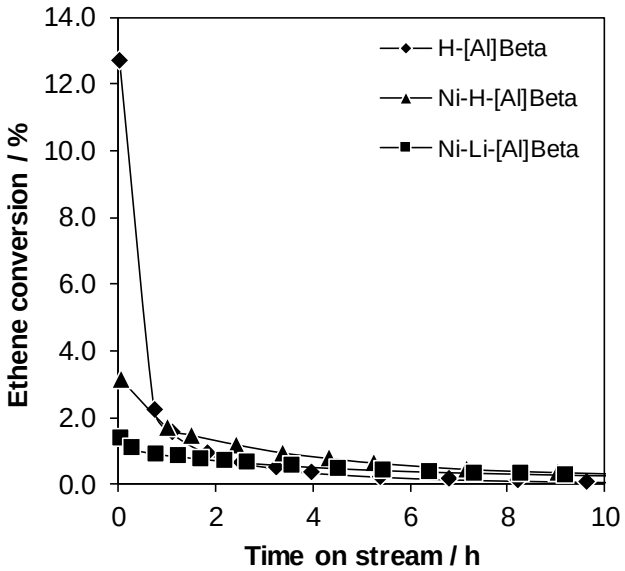

Figure 2.29. Variation of ethene conversion with time on stream at 453 K and 0.4 kPa ethene pressure for H-[Al]Beta (100 s (mol ethene)$^{-1}$ mol H^+), Ni-H-[Al]Beta (2.5 s (mol ethene)$^{-1}$ mol Ni) and Ni-Li-[Al]Beta (2.7 s (mol ethene)$^{-1}$ mol Ni). Lines are intended to guide the eye.

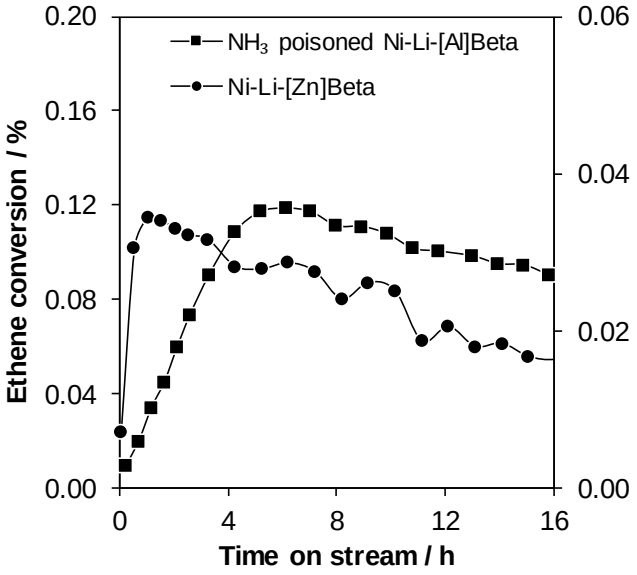

Figure 2.30. Variation of ethene conversion with time on stream at 453 K and 0.4 kPa ethene pressure for Ni-Li-[Al]Beta-NH_3 (2.7 s (mol ethene)$^{-1}$ mol Ni) and Ni-Li-[Zn]Beta (20 s (mol ethene)$^{-1}$ mol Ni). Lines are intended to guide the eye.

2.6.8 Variation of product molar selectivity with ethene conversion

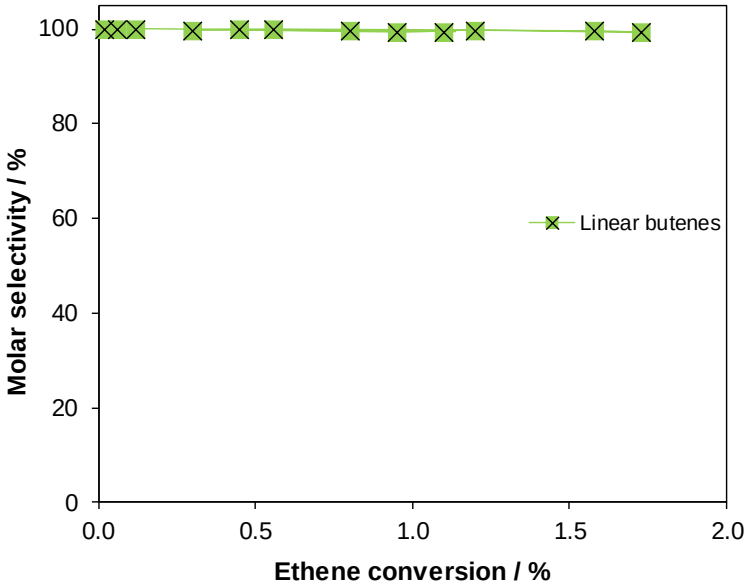

Figure 2.31. Dependence of product molar selectivity on ethene conversion for Ni-Li-[Al]Beta-NH_3 at 453 K, 0.4 kPa ethene. Lines are intended to guide the eye.

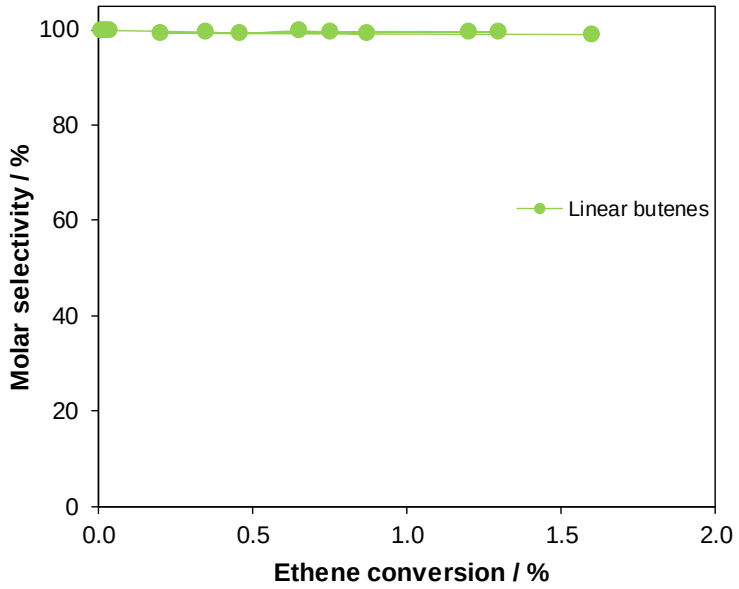

Figure 2.32. Dependence of product molar selectivity on ethene conversion for Ni-Li-[Zn]Beta at 453 K, 0.4 kPa ethene. Lines are intended to guide the eye.

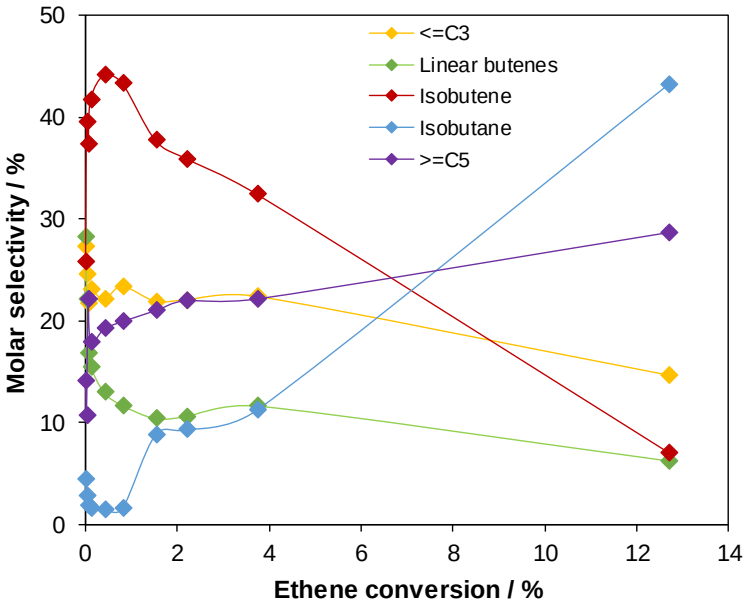

Figure 2.33. Dependence of product molar selectivity on ethene conversion for H-[Al]Beta at 453 K, 0.4 kPa ethene, 100 s (mol ethene)$^{-1}$ mol H^+. Lines are intended to guide the eye.

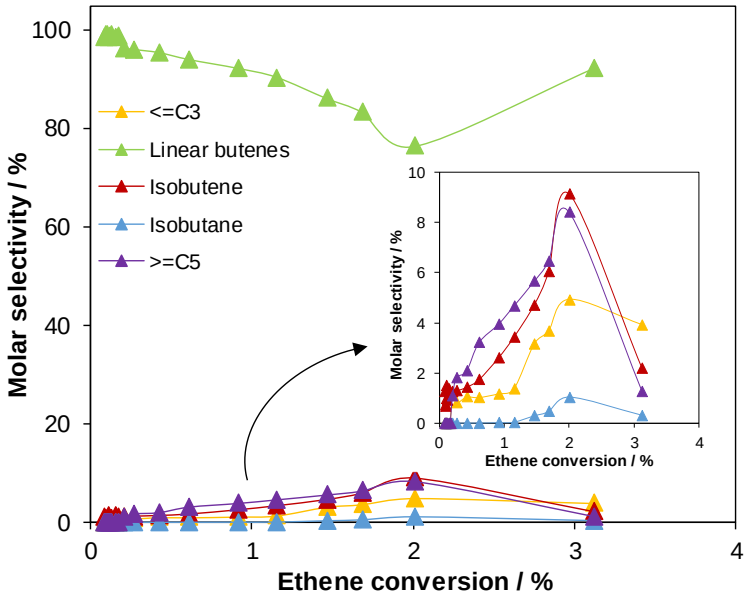

Figure 2.34. Dependence of product molar selectivity on ethene conversion for Ni-H-[Al]Beta at 453 K, 0.4 kPa ethene, 2.5 s (mol ethene)$^{-1}$ mol Ni. The inset shows magnified plot for products with less than 10% molar selectivity. Lines are intended to guide the eye.

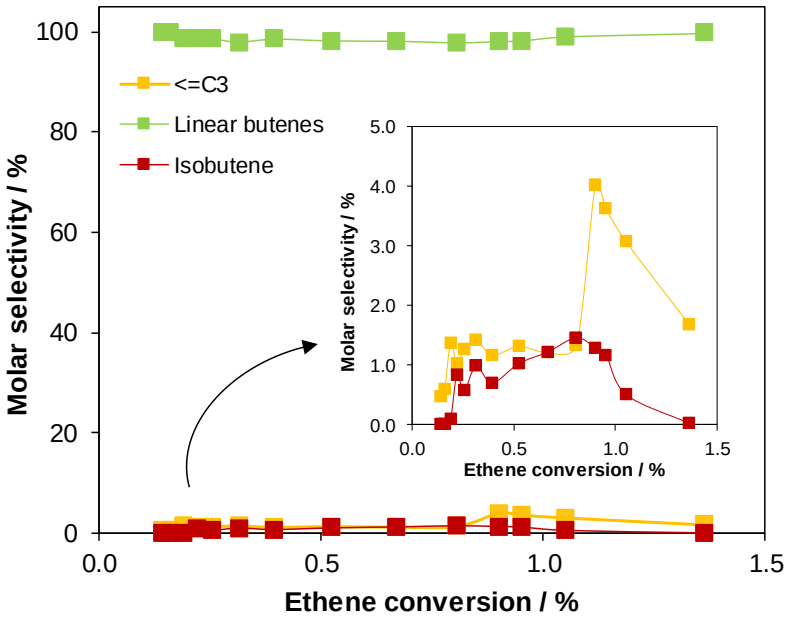

Figure 2.35. Dependence of product molar selectivity on ethene conversion for Ni-Li-[Al]Beta at 453 K, 0.4 kPa ethene, 2.7 s (mol ethene)$^{-1}$ mol Ni. The inset shows magnified plot for products with less than 5% molar selectivity. Lines are intended to guide the eye.

2.6.9 Ethene conversion as a function of reaction time at 453 K and 0.2 kPa ethene

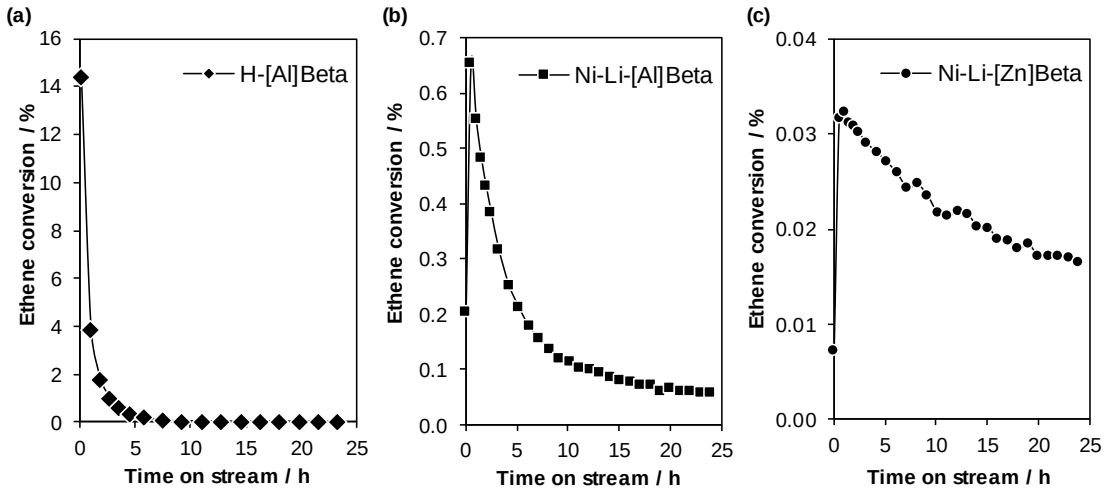

Figure 2.36. Variation of ethene conversion with time on stream at 453 K and 0.2 kPa ethene pressure for (a) H-[Al]Beta (250 s (mol ethene)$^{-1}$ mol H^+), (b) Ni-Li-[Al]Beta (2.4 s (mol ethene)$^{-1}$ mol Ni), and (c) Ni-Li-[Zn]Beta (10.6 s (mol ethene)$^{-1}$ mol Ni). Lines are intended to guide the eye.

2.6.10 Estimation of thermodynamic equilibrium of butene isomers

The equilibrium distribution of butene isomers was determined considering the reactions in Scheme 2.3.

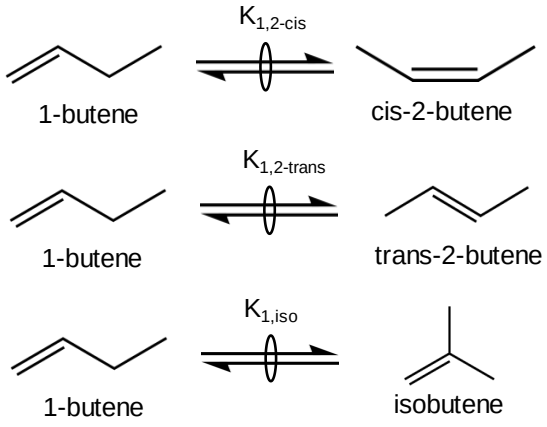

Scheme 2.3. Equilibrium between 1-butene, cis-2-butene, trans-2-butene and isobutene.

The equilibrium constants and butene isomer ratios at 453 K were estimated using the following procedure, and the results are summarized in Table 2.10.

1. The standard-state heat of reaction (ΔH^o_{rxn}) and the standard-state Gibbs free energy of reaction (ΔG^o_{rxn}) were estimated for the equilibria in Scheme 2.3, using equations 2.1 and 2.2, respectively. Table 2.9 shows the reported [139] values for the standard heats of formation and the standard free energies of formation, which were used for equations 2.1 and 2.2.

$$\Delta H^o_{rxn\,(1,isomer)} = \Delta H^o_{f\,(isomer)} - \Delta H^o_{f\,(1-butene)} \quad (2.1)$$

$$\Delta G^o_{rxn\,(1,isomer)} = \Delta G^o_{f\,(isomer)} - \Delta G^o_{f\,(1-butene)} \quad (2.2)$$

2. The equilibrium constants at 298.15 K ($K^o_{1,isomer}$) for the equilibria in Scheme 2.3 were determined from the standard-state free energy of reaction (ΔG^o_{rxn}) using equation 2.3 and are reported in Table 2.10.

$$RTlnK^o_{1,isomer} = -\Delta G^o_{rxn\,(1,isomer)} \quad (2.3)$$

3. The equilibrium constants at 453.15 K for the equilibria in Scheme 2.3 were determined by solving the Van't Hoff equation (Equation 2.4), utilizing the temperature dependence of the heat of reaction given by Equation 2.5. The difference in specific heats (ΔC_p) for each equilibrium in Scheme 2.3 was determined using equations 2.6 and 2.7 [139], where C1, C2, C3, C4 and C5 are constants (Table 2.9). Equations 2.4-2.6 were solved by using the STIFF method within the Ordinary Differential Equation Solver of Polymath 6.10, and the equilibrium constants at 453.15 K ($K_{1,isomer}$) are reported in Table 2.10.

$$\frac{d}{dT} lnK_{1,isomer} = \frac{\Delta H_{rxn(1,isomer)}}{RT^2} \quad (2.4)$$

$$\Delta H_{rxn(1,isomer)} = \Delta H^o_{rxn\,(1,isomer)} + \int_{298.15}^{T} \Delta C_p \, dT \quad (2.5)$$

$$\Delta C_p = C_{p,isomer} - C_{p,1-butene} \quad (2.6)$$

$$C_p = C1 + C2\left[\frac{C3}{T}\Big/ sinh\left(\frac{C3}{T}\right)\right]^2 + C4\left[\frac{C5}{T}\Big/ cosh\left(\frac{C5}{T}\right)\right]^2 \quad (2.7)$$

4. The 2-butenes/1-butene ratio and the isobutene/total butene ratios were calculated using equations 2.8 and 2.9, respectively and are reported in Table 2.10.

$$\frac{2-butenes}{1-butene} = K_{1,2-cis} + K_{1,2-trans} \quad (2.8)$$

$$\frac{isobutene}{total\ butenes} = \left[\frac{K_{1,2-cis} + K_{1,2-trans}}{K_{1,iso}} + \frac{1}{K_{1,iso}} + 1\right]^{-1} \quad (2.9)$$

Table 2.9. Standard heats of formation, standard free energies of formation and constants for specific heat capacity estimation of butene isomers [139].

Butene isomer	Standard (298.15 K) heat of formation / J mol^{-1}	Standard (298.15 K) free energy of formation / J mol^{-1}	Constants for specific heat / J kmol^{-1} K^{-1}				
			C1	C2	C3	C4	C5
1-butene	-500	7.04E+04	59980	208460	1588	129400	707.3
cis 2-butene	-7400	6.54E+04	57650	211500	1630	128720	739.1
trans 2-butene	-11000	6.32E+04	65920	207000	1673	125100	742.2
isobutene	-17100	5.81E+04	61250	206600	1545	120570	676

Table 2.10. Calculated equilibrium constants and butene isomer ratios at 298.15 K and 453.15 K**.**

Calculated parameter	Temperature / K	
	298.15	453.15
$K_{1,2-cis}$	8.022	2.98
$K_{1,2-trans}$	19.557	4.595
$K_{1,iso}$	161.403	16.496
2-butenes/1-butene	27.569	7.523
isobutene/total butenes	0.850	0.659

2.6.11 Effect of ethene pressure on activation period

Figure 2.37 shows the transients for butenes (C_4) site-time yields (1-butene, cis-2-butene, trans-2-butene, isobutene) on Ni-Li-[Al]Beta at 453 K and ethene pressures from 0.05 kPa to 1 kPa. The activation transient was observed for ethene pressures below 0.4 kPa and it was not detected at pressures higher than 0.4 kPa.

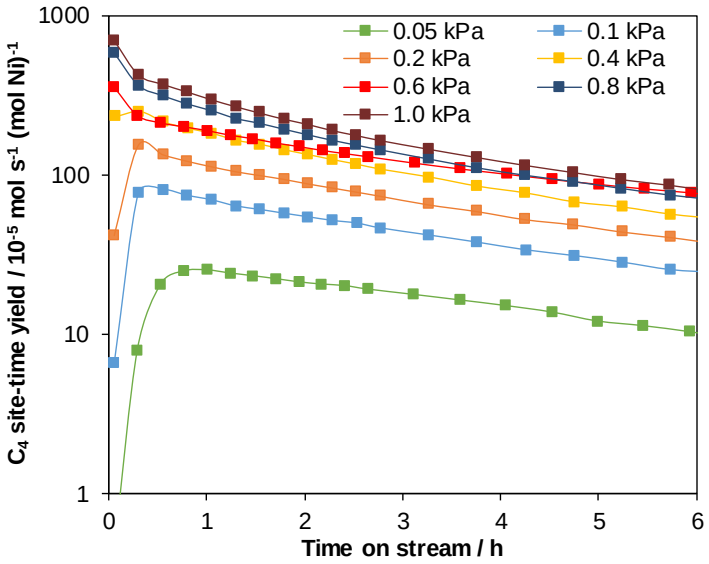

Figure 2.37. Semi-log plot of C_4 site-time yields as a function of time on stream for Ni-Li-[Al]Beta at 453 K and ethene pressures of 0.05, 0.1, 0.2, 0.4, 0.6 and 0.8 kPa.

Figure 2.38 shows the transients for butenes (C_4) site-time yields (1-butene, cis-2-butene, trans-2-butene, isobutene) on Ni-Li-[Zn]Beta at 453 K and ethene pressures from 0.4 kPa to 1 kPa. The activation transient was observed for all ethene pressures up to 1 kPa.

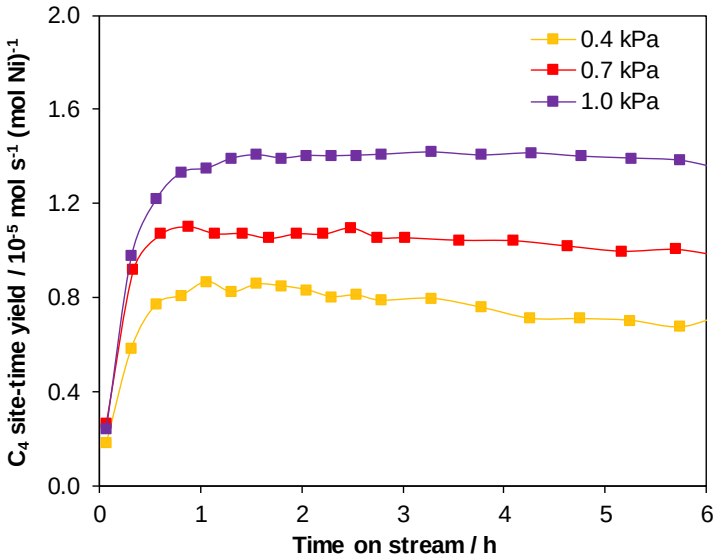

Figure 2.38. C_4 site-time yields as a function of time on stream for Ni-Li-[Zn]Beta at 453 K and ethene pressures of 0.4, 0.7 and 1.0 kPa.

2.6.12 Effect of ethene site-time on activation period

Figures 2.39a and 2.39b show the effect of site-time on measured activation period at 453 K and fixed ethene pressures for Ni-Li-[Al]Beta and Ni-Li-[Zn]Beta, respectively. The error on these measurements is determined by the time between two consecutive GC injections, which is about 0.2 h. The activation period measured for Ni-Li-[Al]Beta at 0.2 and 0.3 kPa ethene could not be distinguished, within this error. Nevertheless, the activation period was invariant with site-time at fixed ethene pressure for Ni-Li-[Al]Beta. For Ni-Li-[Zn]Beta, however, no particular trend could be recognized.

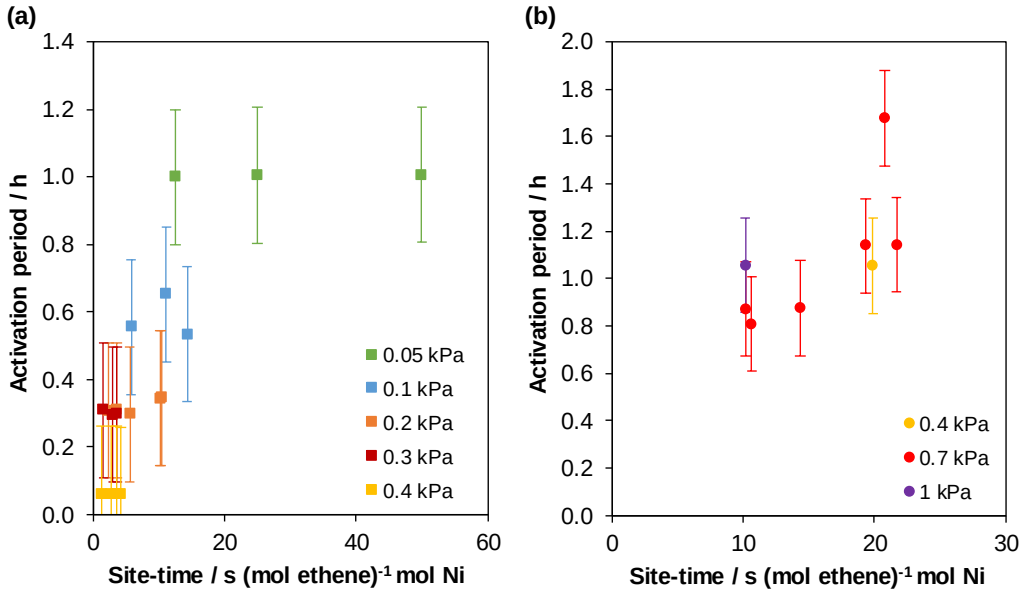

Figure 2.39. Effect of ethene site-time on activation period measured at 453 K for (a) Ni-Li-[Al]Beta (0.05, 0.1, 0.2, 0.3 and 0.4 kPa), and (b) Ni-Li-[Zn]Beta (0.4, 0.7 and 1 kPa).

2.6.13 Initial butenes site-time yields on H^+ and Ni^{2+} cations

The butenes (C_4) site-time yield (1-butene, cis-2-butene, trans-2-butene, isobutene) at 453 K decreased with time on stream for H-[Al]Beta, Ni-H-[Al]Beta, Ni-Li-[Al]Beta and Ni-Li-[Zn]Beta samples for all ethene pressures studied, as these samples deactivated at extended reaction times. The deactivation of H^+ and Ni sites has been respectively attributed to the formation of coke [140] via polycondensed aromatics [141] and to the formation of large oligomers (C_8, C_{10}, C_{12}, C_{14}) [33, 41] which do not desorb under these reaction conditions.

Figure 2.40a shows the C_4 site-time yield with time on stream for H-[Al]Beta at 453 K and 0.2 kPa ethene (142.9 s (mol ethene)$^{-1}$ mol H^+). The deactivation transient followed an exponential decay, and thus a first order deactivation rate model was fitted to estimate the initial C_4 site-time yield. The initial C_4 site-time yields were estimated for experiments performed at varying ethene site-times, and extrapolated to determine the initial C_4 site-time yield at zero ethene site-time, as shown in Figure 2.40b. The butenes formed on H-[Al]Beta are consumed in secondary reactions such as cracking and oligomerization (Figure 2.33), therefore the initial C_4 site-time yield at zero

site-time represents the initial C_4 formation rate, or initial ethene dimerization rate, and is shown in Table 2.11.

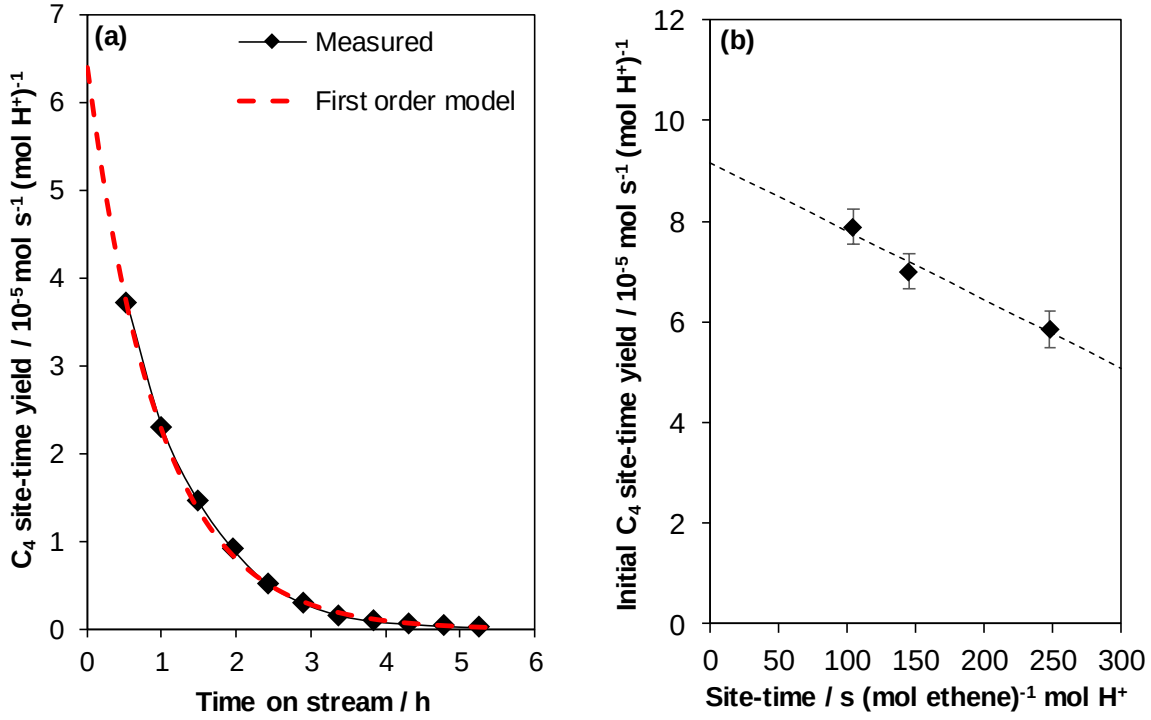

Figure 2.40. (a) C_4 site-time yield measured as a function of time on stream on H-[Al]Beta at 453 K, 0.2 kPa ethene and 142.9 s (mol ethene)$^{-1}$ mol H^+. (b) Variation of initial C_4 site-time yield with site-time on H-[Al]Beta at 453 K and 0.2 kPa ethene.

Next, Figure 2.41a shows the C_4 site-time yield (STY) with reaction time, measured on Ni-Li-[Zn]Beta at 453 K and 0.2 kPa ethene (71.4 s (mol ethene)$^{-1}$ mol Ni). Similar to H-[Al]Beta, the deactivation transient was exponential, and a first order deactivation model was fitted to estimate the initial C_4 site-time yield. The initial butenes site-time yields were also estimated at different ethene site-times, and were invariant with ethene site-time, as shown in Figure 2.41b. Thus, the initial butene formation rate, or initial ethene dimerization rate, was determined as the mean value of the estimated initial C_4 site-time yields and is shown in Table 2.11.

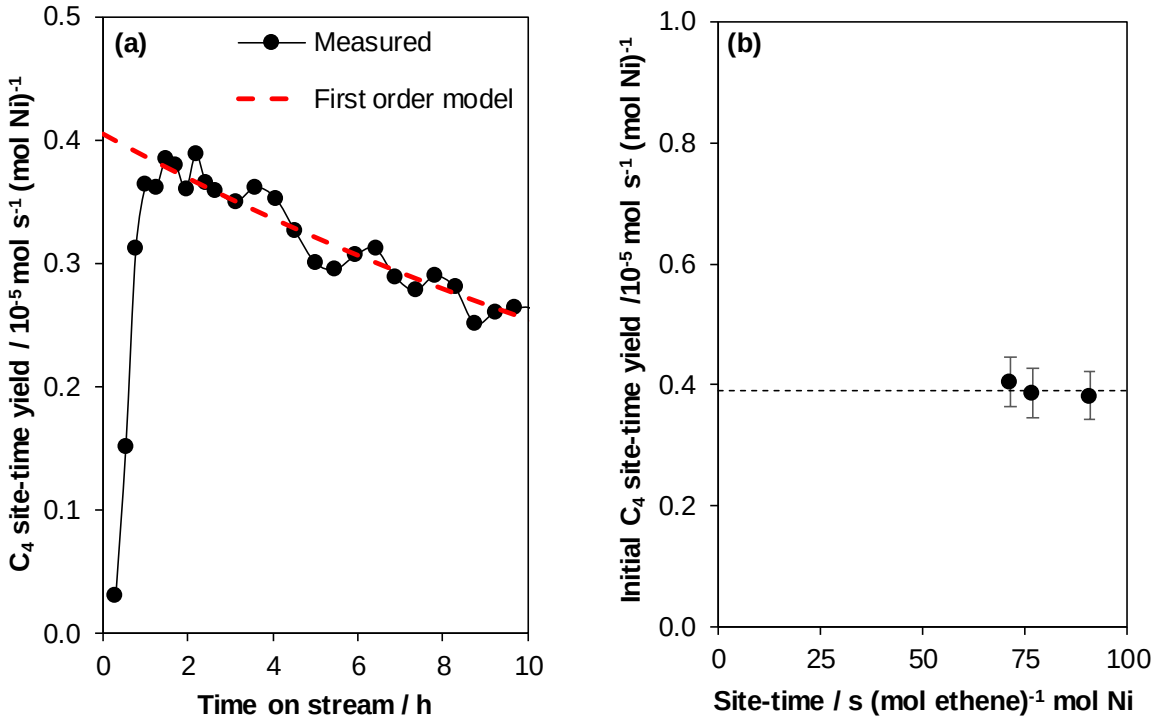

Figure 2.41. (a) C_4 site-time yield measured as a function of time on stream on Ni-Li-[Zn]Beta at 453 K, 0.2 kPa ethene and 71.4 s (mol ethene)$^{-1}$ mol Ni. (b) Variation of initial C_4 site-time yield with site-time on Ni-Li-[Zn]Beta at 453 K and 0.2 kPa ethene.

Further, Figure 2.42a shows the C_4 site-time yield (STY) with time on stream for Ni-Li-[Al]Beta at 453 K and 0.2 kPa ethene (2.4 s (mol ethene)$^{-1}$ mol Ni). The deactivation transient was hyperbolic indicating a multi-site deactivation phenomenon, [142] and a second-order deactivation model was fitted to estimate the initial site-time yield of butenes. Similar to H-[Al]Beta, the initial C_4 site-time yields were estimated at different ethene site-times (Figure 2.42b) and extrapolated to zero ethene site-time to determine the initial C_4 formation rate or initial ethene dimerization rate and is shown in Table 2.11.

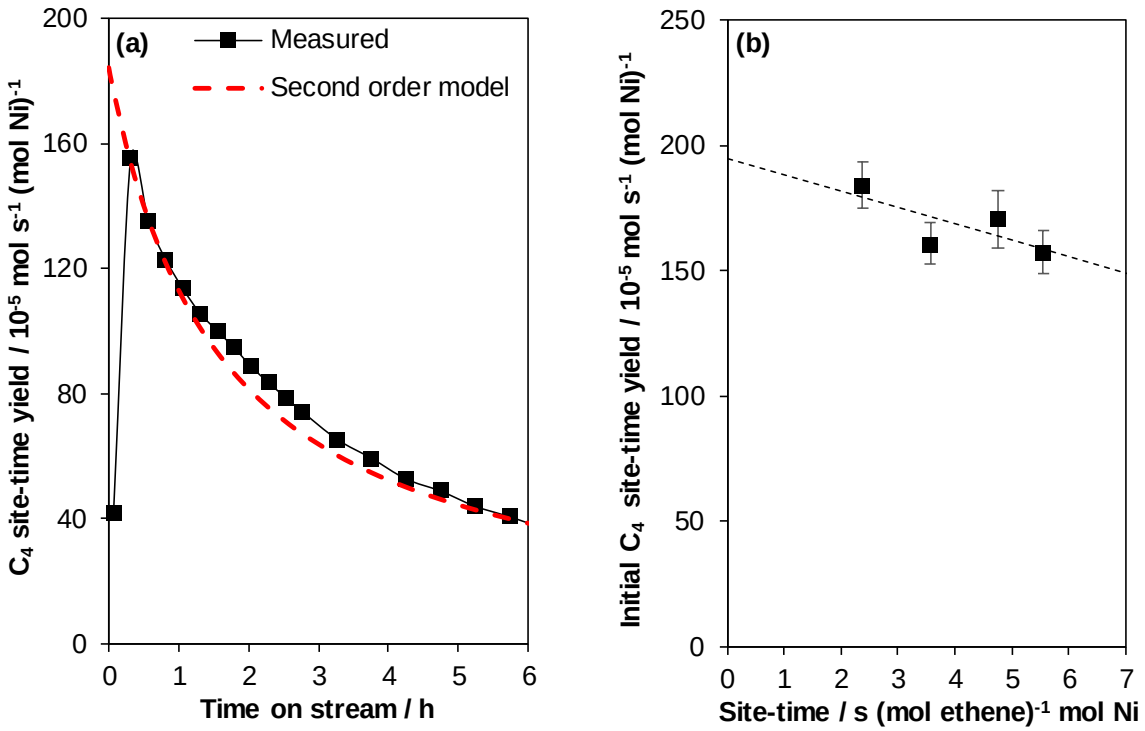

Figure 2.42. (a) C_4 site-time yield measured as a function of time on stream on Ni-Li-[Al]Beta at 453 K, 0.2 kPa ethene and 2.4 s (mol ethene)$^{-1}$ (mol Ni). (b) Variation of initial C_4 site-time yield with site-time on Ni-Li-[Al]Beta at 453 K and 0.2 kPa ethene.

Table 2.11. Initial ethene dimerization rates measured at 453 K and 0.2 kPa ethene

Catalyst	Initial butenes STY at zero site-time (Initial butene formation rate) / 10^{-5} mol s^{-1} (mol site*)$^{-1}$
H-[Al]Beta	9.16
Ni-Li-[Zn]Beta	0.43
Ni-Li-[Al]Beta	183.47

*Site – H^+ for H-[Al]Beta, Ni for Ni-Li-[Zn]Beta and Ni-Li-[Al]Beta

2.6.14 H/D isotopic scrambling and H_2-D_2 exchange experiments

2.6.14.1 Statistical estimation of most probable H/D distribution

The scrambling of H and D atoms to form a distribution of H_2, D_2 and HD molecules can be determined statistically by calculating the probabilities of H and D recombination. This statistical analysis performed by considering equal probability of combining every H and D atom

has been shown to yield the most probable distribution of H and D atoms [143]. Described below is a derivation to estimate the most probable H/D distribution for a given composition of an inlet H_2-D_2 mixture.

1. Consider an ensemble of P total atoms on a catalyst surface consisting of M number of hydrogen atoms and N number of deuterium atoms, and let m and n be the fractions of hydrogen and deuterium atoms, respectively.

$$P = M + N \tag{2.10}$$

$$M = mP \tag{2.11}$$

$$N = nP \tag{2.12}$$

2. The recombination of H and D atoms on the catalyst surface will form molecular H_2, D_2 and HD as the products. The selectivity (S) for each product is equal to the probability (P) of the recombination events between H and D atoms required to form that product, as shown by equations 2.13-2.15. For example, the H_2 selectivity, $S(H_2)$, will be equal to the probability of combining one H atom with another H atom, among an ensemble of P atoms, given by equation 2.16. For the analysis below, an equal probability of combination of every H and D atom, with every other H and D atom is considered (Equations 2.16-2.18) to obtain the statistically most probable distribution. Also, since M, N and P are the number of atoms (not moles), M, N, P >> 1.

$$H_2\ selectivity = S(H_2) = \frac{H_2}{H_2 + D_2 + HD} = P(H_2) \tag{2.13}$$

$$D_2\ selectivity = S(D_2) = \frac{D_2}{H_2 + D_2 + HD} = P(D_2) \tag{2.14}$$

$$HD\ selectivity = S(HD) = \frac{HD}{H_2 + D_2 + HD} = P(HD) \tag{2.15}$$

$$P(H_2) = \frac{{}_MC_1}{{}_PC_1} \times \frac{{}_{M-1}C_1}{{}_{P-1}C_1} \approx \frac{{}_MC_1}{{}_PC_1} \times \frac{{}_MC_1}{{}_PC_1} \tag{2.16}$$

$$P(D_2) = \frac{{}_NC_1}{{}_PC_1} \times \frac{{}_{N-1}C_1}{{}_{P-1}C_1} \approx \frac{{}_NC_1}{{}_PC_1} \times \frac{{}_NC_1}{{}_PC_1} \tag{2.17}$$

$$P(HD) = \frac{{}_MC_1}{{}_PC_1} \times \frac{{}_NC_1}{{}_{P-1}C_1} + \frac{{}_NC_1}{{}_PC_1} \times \frac{{}_MC_1}{{}_{P-1}C_1} \approx 2 \times \frac{{}_MC_1}{{}_PC_1} \times \frac{{}_NC_1}{{}_PC_1} \tag{2.18}$$

$$S(H_2) = P(H_2) = \frac{M}{P} \times \frac{M}{P} = \frac{m^2P^2}{P^2} = m^2 \quad (2.19)$$

$$S(D_2) = P(D_2) = \frac{N}{P} \times \frac{N}{P} = \frac{n^2P^2}{P^2} = n^2 \quad (2.20)$$

$$S(HD) = P(HD) = 2 \times \frac{M}{P} \times \frac{N}{P} = \frac{2mnP^2}{P^2} = 2mn \quad (2.21)$$

3. The H and D atoms within the ensemble are formed by dissociative adsorption of molecular H_2 and D_2 from the inlet gas mixture, so the fraction of H and D atoms, represented by m and n, correspond to the relative mole fractions of gaseous H_2 and D_2 in the inlet stream. Thus, the selectivities for the products H_2, D_2 and HD can be estimated by using equations 2.19-2.21 for a given composition (m, n) of inlet H_2-D_2 mixture.

2.6.14.2 H/D scrambling on 1% Pt/Al_2O_3 sample

H/D isotopic scrambling on 1% Pt/Al_2O_3 sample was performed by preparing inlet H_2 and D_2 mixtures of six different compositions and contacting them with the sample (pre-reduced using H_2, 673 K, 1 h) at 453 K. Figure 2.43 shows the selectivities for HD products measured on the 1% Pt/Al_2O_3 sample at different inlet H_2-D_2 compositions, which were consistent with those for statistical scrambling of deuterium content of inlet H_2-D_2 compositions, calculated using equation 2.21.

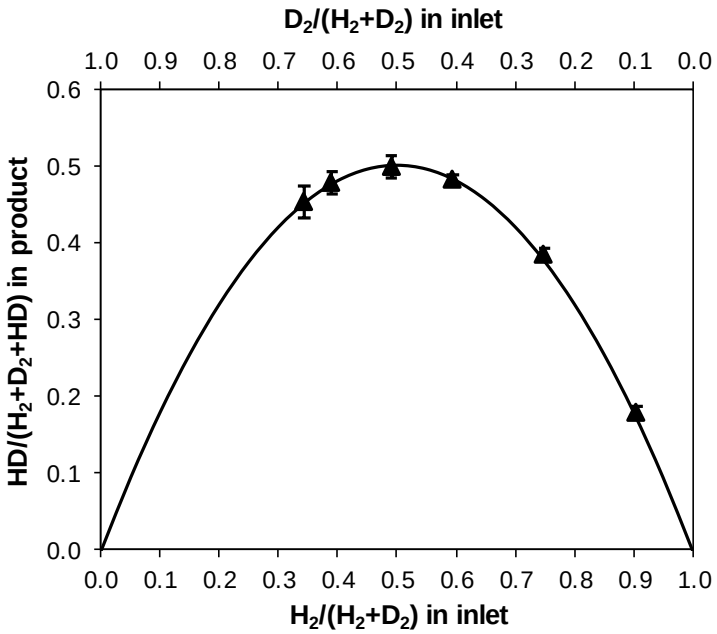

Figure 2.43. HD product selectivities measured on 1% Pt/Al_2O_3 sample (▲) at 453 K as a function of H_2-D_2 inlet compositions. The solid line (——) shows the calculated HD selectivities for statistical scrambling of deuterium content of inlet H_2-D_2 compositions.

2.6.14.3 H/D scrambling on Ni-Li-[Al]Beta, Li-[Al]Beta and H-[Al]Beta samples

Similar to 1% Pt/Al_2O_3 sample, H/D isotopic scrambling was performed on a Ni-Li-[Al]Beta sample (pretreated in air, 803 K, 5 h) held at 453 K. The H_2 and D_2 gases were also contacted with the Li-[Al]Beta and H-[Al]Beta samples at an inlet H_2-D_2 composition of 60%-40% at 453 K. Figure 2.44 shows the selectivities for HD products measured on Ni-Li-[Al]Beta, Li-[Al]Beta and H-[Al]Beta samples and also those calculated for statistical scrambling of deuterium content of inlet H_2-D_2 compositions, using equation 2.21. The Ni-Li-[Al]Beta sample, but not the Li-[Al]Beta and H-[Al]Beta samples, statistically scrambled the isotopic content of the inlet H_2-D_2 mixtures.

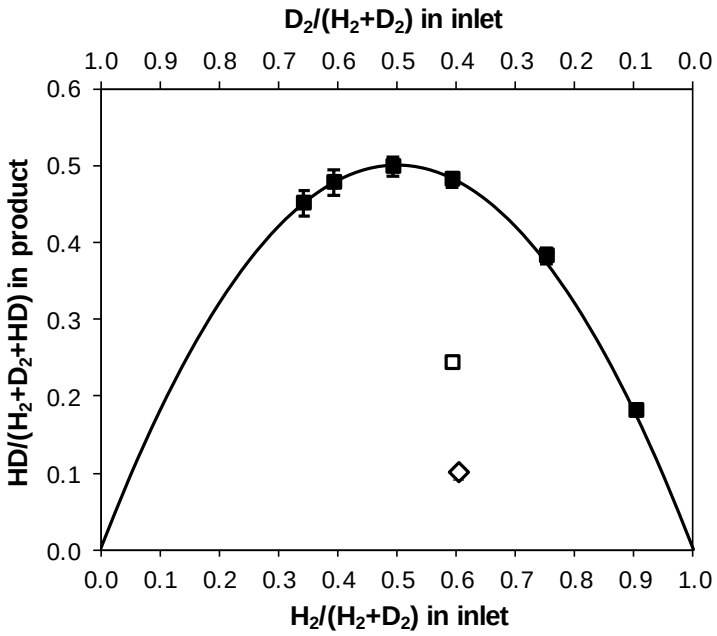

Figure 2.44. HD product selectivities measured on Ni-Li-[Al]Beta (■), Li-[Al]Beta (□) and H-[Al]Beta (◊) samples at 453 K as a function of H_2-D_2 inlet compositions. The solid line (——) shows the calculated HD selectivities for statistical scrambling of deuterium content of inlet H_2-D_2 compositions.

2.6.14.4 H/D scrambling on Ni-Li-[Zn]Beta and Li-[Zn]Beta samples

Similar to 1% Pt/Al_2O_3 and Ni-Li-[Al]Beta samples, H/D isotopic scrambling on Ni-Li-[Zn]Beta was performed by preparing inlet H_2 and D_2 gas mixtures of varying composition and contacting them with the sample (pretreated in air, 803 K, 5 h) at 453 K. These inlet H_2 and D_2 gas mixtures were also contacted with the Li-[Zn]Beta sample at an inlet H_2-D_2 composition of 60%-40% at 453 K. Figure 2.45 shows the selectivities for HD products measured on Ni-Li-[Zn]Beta and Li-[Zn]Beta samples and also those calculated for statistical scrambling of deuterium content of inlet H_2-D_2 compositions, using equation 2.21. The Ni-Li-[Zn]Beta sample, but not the Li-[Zn]Beta sample, statistically scrambled the isotopic content of inlet H_2-D_2 mixtures.

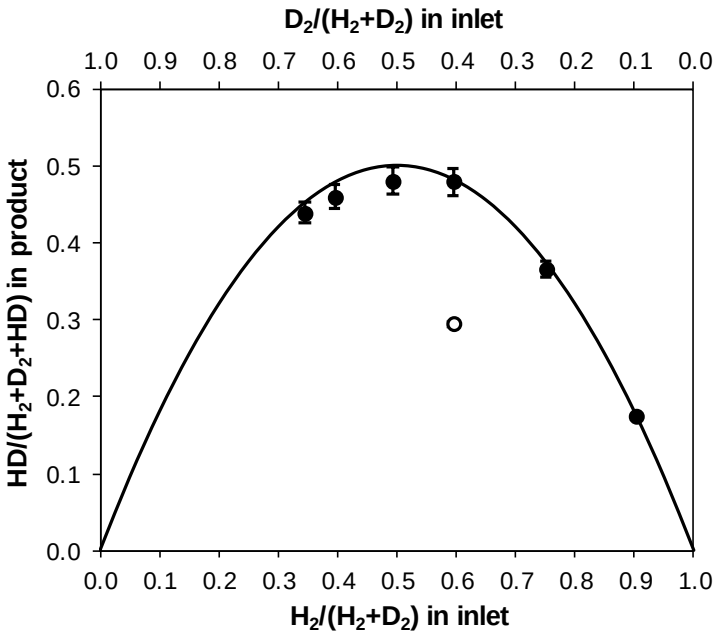

Figure 2.45. HD product selectivities measured on Ni-Li-[Zn]Beta (●) and Li-[Zn]Beta (○) samples at 453 K as a function of H_2-D_2 inlet compositions. The solid line (——) shows the calculated HD selectivities for statistical scrambling of deuterium content of inlet H_2-D_2 compositions.

2.6.14.5 H_2, D_2 and HD transients during H_2-D_2 exchange experiments

For H_2-D_2 exchange experiments, each sample was first pretreated in air (803 K, 4-5 h) and then held in flowing H_2 (453 K, 5 kPa H_2 in Ar, 1-2 h) to form $[Ni(II)\text{-}H]^+$, followed by a step change that replaced H_2 with D_2 (453 K, 5 kPa D_2 in Ar, 1-2 h) in order to convert $[Ni(II)\text{-}H]^+$ species into $[Ni(II)\text{-}D]^+$ species and form gaseous HD. Then, a second step change to replace D_2 with H_2 was performed to quantify the number of $[Ni(II)\text{-}D]^+$ species that reversibly exchange isotopes to form $[Ni(II)\text{-}H]^+$ and gaseous HD. Figure 2.46 shows the time on stream profiles for molar H_2, D_2 and HD flows measured on the Ni-Li-[Al]Beta sample at 453 K for six consecutive H_2-D_2 step changes, and Figure 2.47 shows the same only for the first two step changes for enhanced clarity. Figures 2.48-2.51 show the time on stream profiles for H_2, D_2 and HD molar flows measured on the Li-[Al]Beta, H-[Al]Beta, Ni-Li-[Zn]Beta and Li-[Zn]Beta samples, respectively, at 453 K. The 5 kPa H_2 in Ar and 5 kPa D_2 in Ar mixtures showed a distinct but non-zero signal for HD (m/z = 3) when fed directly to the Residual Gas Analyzer (RGA), used to

determine the baseline values for HD molar flows that are denoted by the dashed line in Figures 2.46-2.51.

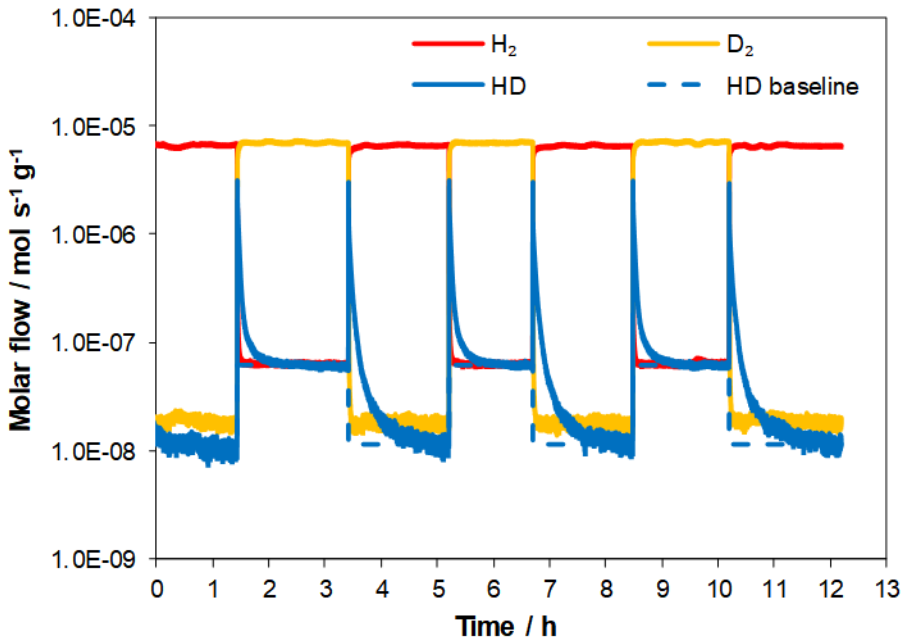

Figure 2.46. Semi-log plot for H_2, D_2 and HD molar flows against time, measured on Ni-Li-[Al]Beta at 453 K during consecutive step changes between 5 kPa H_2 in Ar and 5 kPa D_2 in Ar.

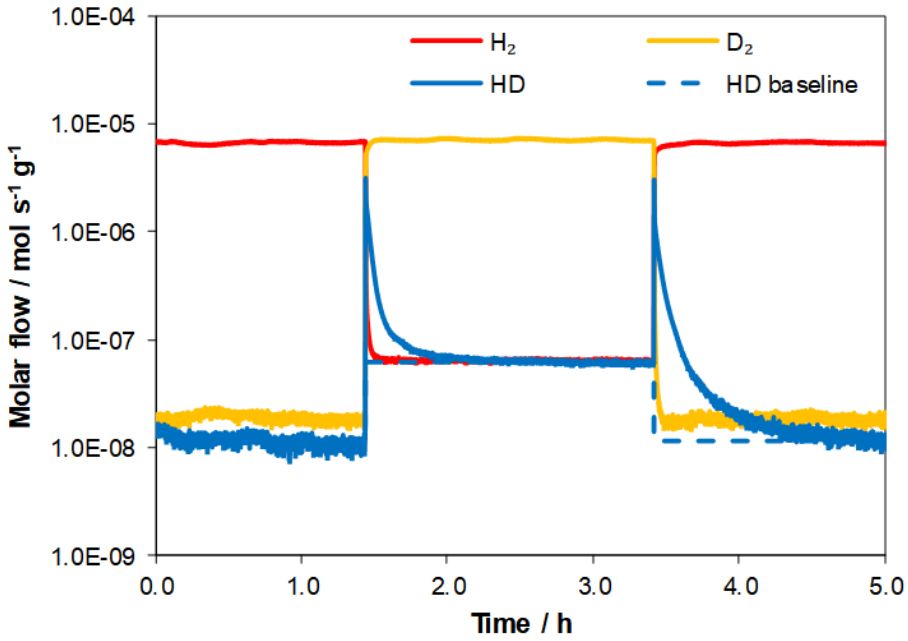

Figure 2.47. Semi-log plot for H_2, D_2 and HD molar flows against time, measured on Ni-Li-[Al]Beta at 453 K during the first two step changes between 5 kPa H_2 in Ar and 5 kPa D_2 in Ar.

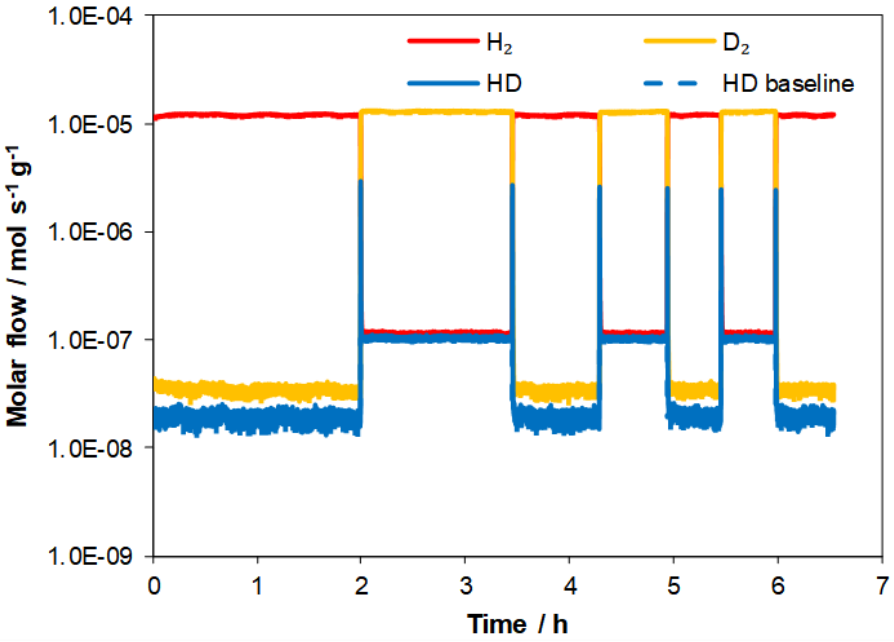

Figure 2.48. Semi-log plot for H_2, D_2 and HD molar flows against time, measured on Li-[Al]Beta at 453 K during consecutive step changes between 5 kPa H_2 in Ar and 5 kPa D_2 in Ar.

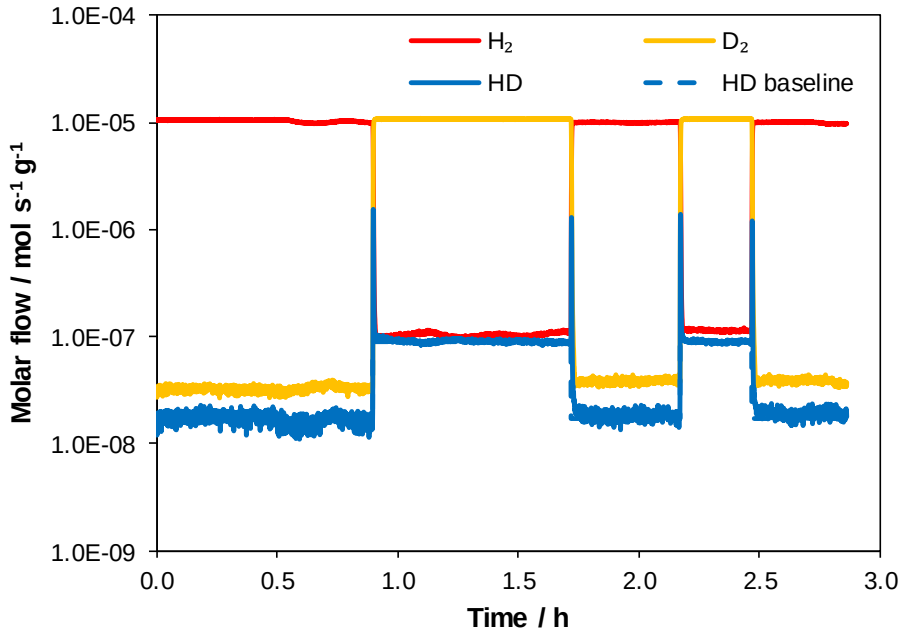

Figure 2.49. Semi-log plot for H_2, D_2 and HD molar flows against time, measured on H-[Al]Beta at 453 K during consecutive step changes between 5 kPa H_2 in Ar and 5 kPa D_2 in Ar.

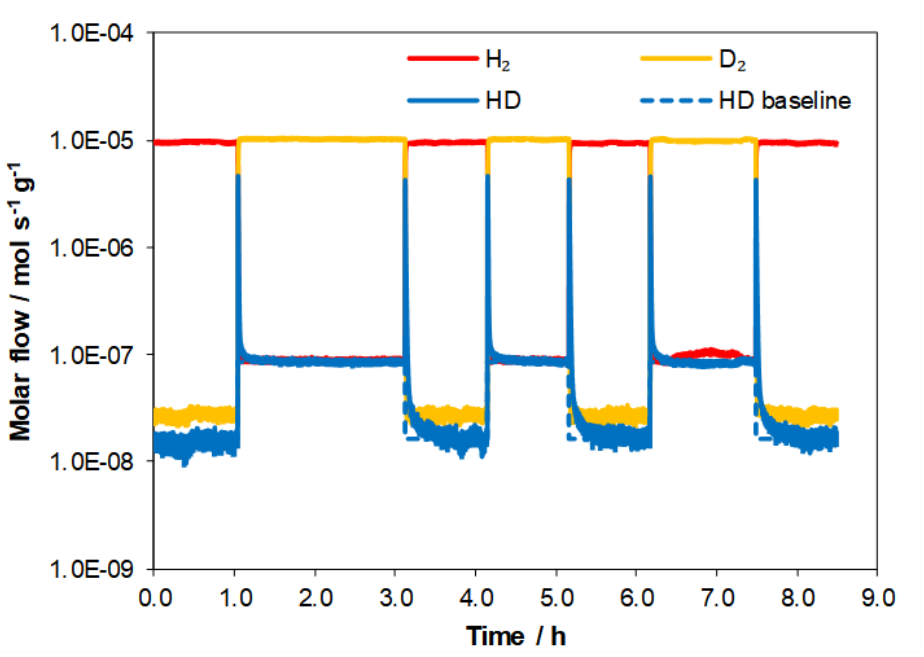

Figure 2.50. Semi-log plot for H_2, D_2 and HD molar flows against time, measured on Ni-Li-[Zn]Beta at 453 K during consecutive step changes between 5 kPa H_2 in Ar and 5 kPa D_2 in Ar.

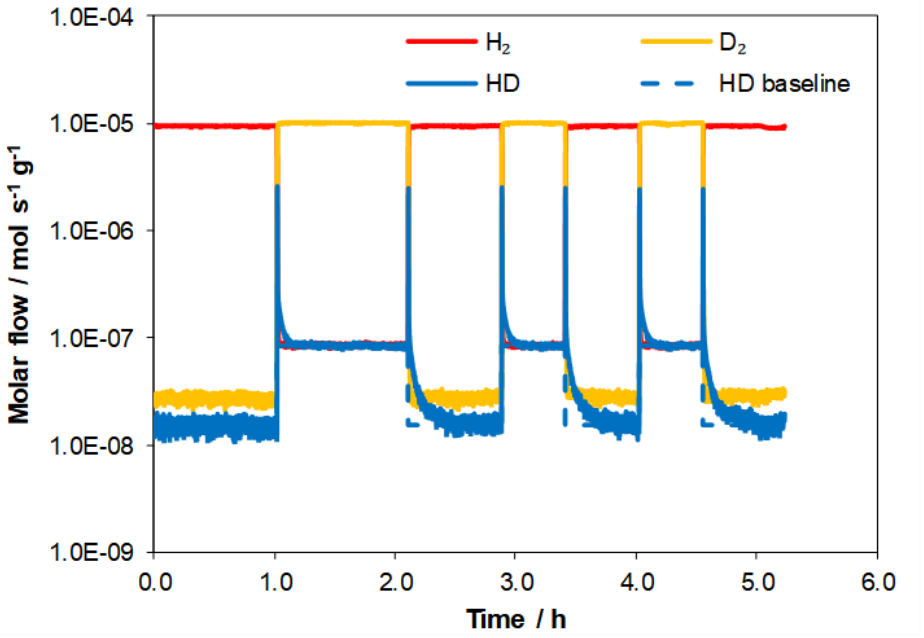

Figure 2.51. Semi-log plot for H_2, D_2 and HD molar flows against time, measured on Li-[Zn]Beta at 453 K during consecutive step changes between 5 kPa H_2 in Ar and 5 kPa D_2 in Ar.

2.6.14.6 HD Quantification from H_2-D_2 exchange experiments

For all samples, the measured HD molar flow was corrected for the HD baseline (dashed line in Figures 2.46-2.51) and then integrated for the time duration of the step change to determine the moles of HD formed during each step change. Table 2.12 shows the moles of HD quantified per dry mass (corrected for water content measured by TGA, Table 2.7) of the Ni-Li-[Al]Beta, Li-[Al]Beta, H-[Al]Beta, Ni-Li-[Zn]Beta and Li-[Zn]Beta samples, corresponding to each step change at 453 K.

Table 2.12. HD moles quantified by H_2-D_2 exchanges at 453 K.

Sample	HD moles quantified during step change / 10^{-3} mol g^{-1}	
	$H_2 \rightarrow D_2$	$D_2 \rightarrow H_2$
Ni-Li-[Al]Beta	0.30	0.28
	0.29	0.28
	0.29	0.28
Li-[Al]Beta	0.03	0.02
	0.02	0.02
	0.02	0.02
H-[Al]Beta	0.01	0.01
	0.01	0.01
Ni-Li-[Zn]Beta	0.12	0.13
	0.12	0.13
	0.12	0.12
Li-[Zn]Beta	0.04	0.04
	0.04	0.04
	0.04	0.04

To determine the moles of HD formed only at the Ni sites of Ni-Li-[Al]Beta and Ni-Li-[Zn]Beta samples, the moles of HD formed per dry mass of Li-[Al]Beta and Li-[Zn]Beta (Table 2.12) were respectively subtracted from those measured on Ni-Li-[Al]Beta and Ni-Li-[Zn]Beta samples (Table 2.12) for each corresponding step change, and the corrected values are shown in Table 2.13. Further, the moles of HD quantified per dry mass of the H-[Al]Beta sample (Table 2.12) were 20 times lower than those on Ni-Li-[Al]Beta sample; thus, the possibility of HD exchange at acidic hydroxyl groups present in minority amounts or generated *in-situ* during dissociative adsorption of H_2 or D_2 on Ni-Li-[Al]Beta sample can be excluded.

Table 2.13. HD moles quantified by H_2-D_2 exchanges at 453 K and corrected for non-Ni contributions.

Sample	Corrected HD moles quantified during step change / 10^{-3} mol g^{-1}	
	$H_2 \rightarrow D_2$	$D_2 \rightarrow H_2$
Ni-Li-[Al]Beta	0.28	0.26
	0.27	0.26
	0.27	0.26
Ni-Li-[Zn]Beta	0.08	0.09
	0.08	0.09
	0.08	0.08

3. SITE REQUIREMENTS AND KINETICS OF ETHENE DIMERIZATION CATALYZED BY NICKEL CATIONS

3.1 Introduction

In Chapter 2, the coordination-insertion mechanism was shown to be the dominant route for ethene dimerization on Ni-containing Beta zeolites. Also, the coordination-insertion catalytic cycle was shown to be initiated by the formation of Ni(II)-hydride intermediates from the Ni^{2+} cations exchanged on zeolite Beta.

In addition to these exchanged Ni^{2+} cations, other Ni structures have been proposed as the precursors to the dimerization active sites. For example, $[NiOH]^+$ cations were proposed as the precursor sites by Agirrezabal-Telleria and Iglesia [41], because the dimerization rates (per g_{cat}) on MCM-41 increased linearly with $Ni/H^+_{initial}$ ratio up to unity and were independent thereafter. Ni^{2+} cations grafted at acidic silanol groups and undercoordinated Ni^{2+} sites on NiO nanoparticles were proposed by Moussa et al. [144] since materials predominantly containing these Ni structures exhibited higher ethene consumption rates (per g_{cat}) than those containing exchanged Ni^{2+} cations [144]. Moreover, Ni^{2+} cations grafted at acidic silanol groups were proposed to undergo an oxidative addition with an alkene C-H bond to form Ni ethenyl hydride intermediates, which were further proposed to mediate ethene dimerization by a mechanism similar to coordination-insertion [51].

Further, the catalytic studies for alkene dimerization on these Ni precursor sites have been carried out at various reaction conditions and with different methodologies for kinetic data analysis because of catalyst deactivation. In the case of propene dimerization (453 K, 1-5 bar) on exchanged Ni^{2+} cations in X zeolite, pseudo steady-state rates were measured for propene consumption after prolonged deactivation (>16 h) and exhibited a first order dependence on propene pressure but also varied with Ni density [32]. In contrast, for ethene dimerization (393 K, 11.6 – 25.1 bar) on exchanged Ni^{2+} cations in Beta zeolite, ethene consumption rates obtained by correcting for deactivation by return to reference reaction conditions with a predetermined deactivation model exhibited a second order dependence on ethene pressure. Also, for the proposed $NiOH^+$ sites in MCM-41, no deactivation was observed for low Ni loading samples ($Ni/Al \leq 0.8$), and steady-state ethene dimerization rates (448 K, 5-25 bar) showed a second order dependence on ethene

pressure [41]. Since the reaction data in these studies were measured in different kinetic regimes, it remains unclear if all the Ni structures proposed as precursor sites are transformed into the Ni-hydride or Ni-alkyl intermediates that initiate the coordination mechanism.

Here, the kinetics of ethene dimerization are studied on Beta zeotype samples synthesized to predominantly contain the exchanged or the grafted Ni^{2+} cations. The measured catalytic data is analyzed by extrapolation to initial time, which allows correlating the reaction kinetics to the structure of Ni precursor sites determined by *ex-situ* characterization techniques. The mechanistic considerations of the coordination-insertion mechanism together with the measured kinetic parameters clarify the influence of Ni precursor site structure on ethene dimerization catalysis.

3.2 Experimental Methods

3.2.1 Catalyst synthesis and characterization

The samples Ni-Li-[Al]Beta and Ni-Li-[Zn]Beta were synthesized by methods described in Chapter 2 (Section 2.2.1).

The Ni speciation was determined by CO infrared spectroscopy and the structural geometry was probed using diffuse reflectance UV-vis (DRUV) spectroscopy and extended X-ray absorption fine structure (EXAFS) characterization techniques, as described in Chapter 2 (Section 2.2.2).

3.2.2 Reaction measurements

The site-time yields of butene and other reaction products of ethene were measured at 453 K in a packed-bed, plug-flow reactor made of a 3/8-inch O.D. quartz tube. To avoid excessive pressure drop at high feed flow rates, the samples were pelleted and sieved to retain particles in the size range 180-250 μm. Approximately, 0.005-0.100 g of sample was loaded into the reactor, depending on the site-velocity to be maintained, and was supported between two quartz wool plugs. The Ni-Li-[Al]Beta sample was diluted with pure-silica Beta (Si-Beta-F) to ensure a minimum of 0.025 g of total solids in the reactor, while the H-[Al]Beta and Ni-Li-[Zn]Beta samples were loaded without dilution. The pure-silica Beta (Si-Beta-F) was independently determined to be catalytically inert throughout the range of reaction conditions to be tested. The

temperature of the catalyst bed was measured with a K-type thermocouple in direct contact with the external surface of the quartz tube and positioned at the center of the catalyst bed. The reactor was heated using a resistively-heated three-zone furnace (Series 3210, Applied Test Systems) and the temperature was controlled using Watlow controllers (EZ-Zone Series).

Before introducing ethene, the samples were (0.01–0.10 g) were treated at 803 K (0.0167 K s^{-1}) in a 5% O_2/95% He mixture (16.7 cm^3 g_{cat}^{-1} s^{-1}, 99.999%, Matheson Tri-Gas) for 4 hours followed by cooling to 453 K. During the cool down step, a reactant mixture consisting of ethene (1% C_2H_4, 5% Ar, 94% He, Matheson Tri-Gas, 99.999% purity) and He (Pure, Matheson Tri-Gas, 99.999% purity) was prepared and measurements for quantification of the feed were carried out on a GC-MS system (Agilent 7890B GC; Agilent 5975C MSD). After cooling the catalyst bed to 453 K, the residual oxygen was removed from the system by flowing pure He (16.7 cm^3 g_{cat}^{-1} s^{-1}, 99.999%, Matheson Tri-Gas) for at least 0.5 h. After the He flush, the reactant mixture was contacted with the catalyst bed at near ambient pressures (PX309 series, OMEGA), and the first gas sample was injected to the GC-MS after approximately 3 min of time on stream. Reactants and products were separated using GS-AL/KCl capillary column (0.530 mm ID × 50 m; Agilent) and the outlet flow of the column was split using a splitter plate and sent to a flame ionization detector (FID) and the mass selective detector (MSD). The products were quantified by manually integrating the FID signal and they were identified using the NIST spectra library database and also verified by injecting known hydrocarbon standards. The ethene partial pressure was varied (0.01–1 kPa; 10^{-7}–10^{-4} (mol ethene) g^{-1} s^{-1}) by dilution with He (99.999%, Matheson Tri-Gas). The catalysts deactivated with time on stream and were regenerated after every reaction run at 803 K (0.0167 K s^{-1}) in a 5% O_2/95% He mixture (16.7 cm^3 g_{cat}^{-1} s^{-1}, 99.999%, Matheson Tri-Gas) for 4 hours in between consecutive experiments, because they were observed to deactivate with time on stream. Since ethene conversions were differential (< 5%), the total ethene conversion was determined as the ratio of total carbon molar flow rates in the products detected to the total carbon molar flow rates in the ethene feed. No products were detected in the presence of ethene (0.05-1 kPa) at 453 K on Li-[Zn]Beta and Li-[Al]Beta.

Single-site (exponential) and multi-site (hyperbolic) deactivation models (detailed derivations in Section 3.6.2, Supporting Information) were used to fit the measured butene site-

time yields using a Python program (Section 3.6.5, Supporting Information). The choice of the model was determined by the Python program based on the goodness of fit criteria ($R^2 \geq 0.97$).

3.3 Results and Discussion

3.3.1 Characterization of Ni site structures

The IR spectra of CO adsorbed on evacuated samples of Ni-Li-[Al]Beta and Ni-Li-[Zn]Beta collected at 85 K are shown in Figures 2.1b and 2.1c (Chapter 2), respectively, and discussed in detail in Chapter 2 (Section 2.3.2). The Ni-Li-[Al]Beta sample showed predominant features at 2213 and 2206 cm^{-1} corresponding to $Ni^{2+}(CO)$ and $Ni^{2+}(CO)_2$ complexes [94, 95] respectively, while these were absent for Ni-Li-[Zn]Beta. The Ni-Li-[Zn]Beta sample showed a predominant peak at 2196 cm^{-1}, assigned to CO adsorbed on Ni^{2+} cations grafted at silanol defects. The Ni-Li-[Zn]Beta sample also showed a small feature at 2222 cm^{-1} corresponding to a second type of $Ni^{2+}(CO)$ complex that is reported [97, 98] to be distinct from the $Ni^{2+}(CO)$ complex with the characteristic 2213 cm^{-1} feature. The absorption features for $Ni^{+}(CO)_x$ complexes (2113 cm^{-1} for x=1; 2138 and 2095 for x=2; 2106, 2123 and 2156 cm^{-1} for x=3) and those for CO adsorbed on undercoordinated Ni^{2+} on NiO clusters (2155 cm^{-1}) or Ni^0 nanoparticles (2030 cm^{-1}) were not observed on these samples. These results suggested Ni to be predominantly present as exchanged Ni^{2+} cations on Ni-Li-[Al]Beta and as grafted Ni^{2+} cations on Ni-Li-[Zn]Beta. Further, the IR feature for CO adsorbed at Brønsted acid sites (2174 cm^{-1}) [95, 99] was absent for both Ni-Li-[Al]Beta and Ni-Li-[Zn]Beta samples, suggesting the absence of residual H^+ sites.

Also for Ni-Li-[Al]Beta and Ni-Li-[Zn]Beta samples, the DRUV spectra (Figure 2.2b and 2.2c) collected at ambient temperature and the EXAFS characterization (Table 2.3, Figure 2.27 and 2.28) are described in detail in Chapter 2 (Section 2.3.2). The DRUV spectra showed the absorption bands for d-d transitions of octahedrally coordinated Ni^{2+} cations (8600, 13700, 15200 and 25500 cm^{-1}) [103-106], when the Ni-Li-[Al]Beta and Ni-Li-[Zn]Beta samples were present in a hydrated state. After a dehydration treatment, the DRUV spectrum collected at ambient temperature remained unchanged for Ni-Li-[Zn]Beta, while that for Ni-Li-[Al]Beta showed absorption bands for d-d transitions of Ni^{2+} present in a distorted tetrahedral geometry (5800, 12200, 14000, 18900 and 23000 cm^{-1}) [110-112]. This change in structural geometry of Ni^{2+}

cations from octahedral to tetrahedral for Ni-Li-[Al]Beta was quantitatively assessed by EXAFS, which showed a change in Ni-O coordination number from 6 to 4. On the other hand, the EXAFS showed no change in Ni-O coordination number for Ni-Li-[Zn]Beta and it remained 6-coordinate in both the hydrated and dehydrated states (Chapter 2, Table 2.3). These results are consistent with the predominance of exchanged Ni^{2+} cations on Ni-Li-[Al]Beta and that of grafted Ni^{2+} cations on Ni-Li-[Zn]Beta.

3.3.2 Measurement of initial ethene dimerization rates

The Ni-Li-[Al]Beta and Ni-Li-[Zn]Beta catalysts predominantly formed isomers of linear butenes (1-butene, cis-2-butene, trans-2-butene) at 453 K under dilute ethene conditions (0.05-1 kPa), when the ethene conversions were maintained to be differential (< 5%) (Chapter 2, Figure 2.3). Although the CO IR (Chapter 2, Section 2.3.2) showed the absence of H^+ sites on Ni-Li-[Al]Beta, H^+ sites were generated *in-situ* during the formation of Ni-hydrides ($[Ni(II)-H]^+$) from exchanged Ni^{2+} cations (Chapter 2, Section 2.3.4), as indicated by the formation of isobutene, as a result of secondary skeletal isomerization of linear butenes on the H^+ sites [61, 64] (Chapter 2, Section 2.3.3). Isobutene was not detected on Ni-Li-[Zn]Beta perhaps because of the lower ethene conversion and weaker acid strength of H^+ sites on zincosilicate supports as reflected by their inability to protonate pyridine (Chapter 2, Section 2.6.4.5). Thus, the site-time yields for 1-butene, cis-2-butene, trans-2-butene, and isobutene were taken together to estimate the butene (C_4) site-time yields.

The C_4 site-time yields (STY) measured on Ni-Li-[Al]Beta, the H-[Al]Beta support, and Ni-Li-[Zn]Beta at 453 K and 0.2 kPa ethene are respectively plotted against reaction time in Figure 3.1a-c, which show that these samples deactivate at long reaction times. The deactivation of Ni and H^+ sites has been respectively attributed to the formation of heavy molecular weight (C_8, C_{10}, C_{12}, C_{14}) polyconjugated aliphatic and aromatic compounds [33, 41, 141] that do not desorb under these reaction conditions and to the formation of coke [140]. The C_4 site-time yields on Ni-Li-[Al]Beta (Figure 3.1a) exhibited a hyperbolic decay suggesting that deactivation

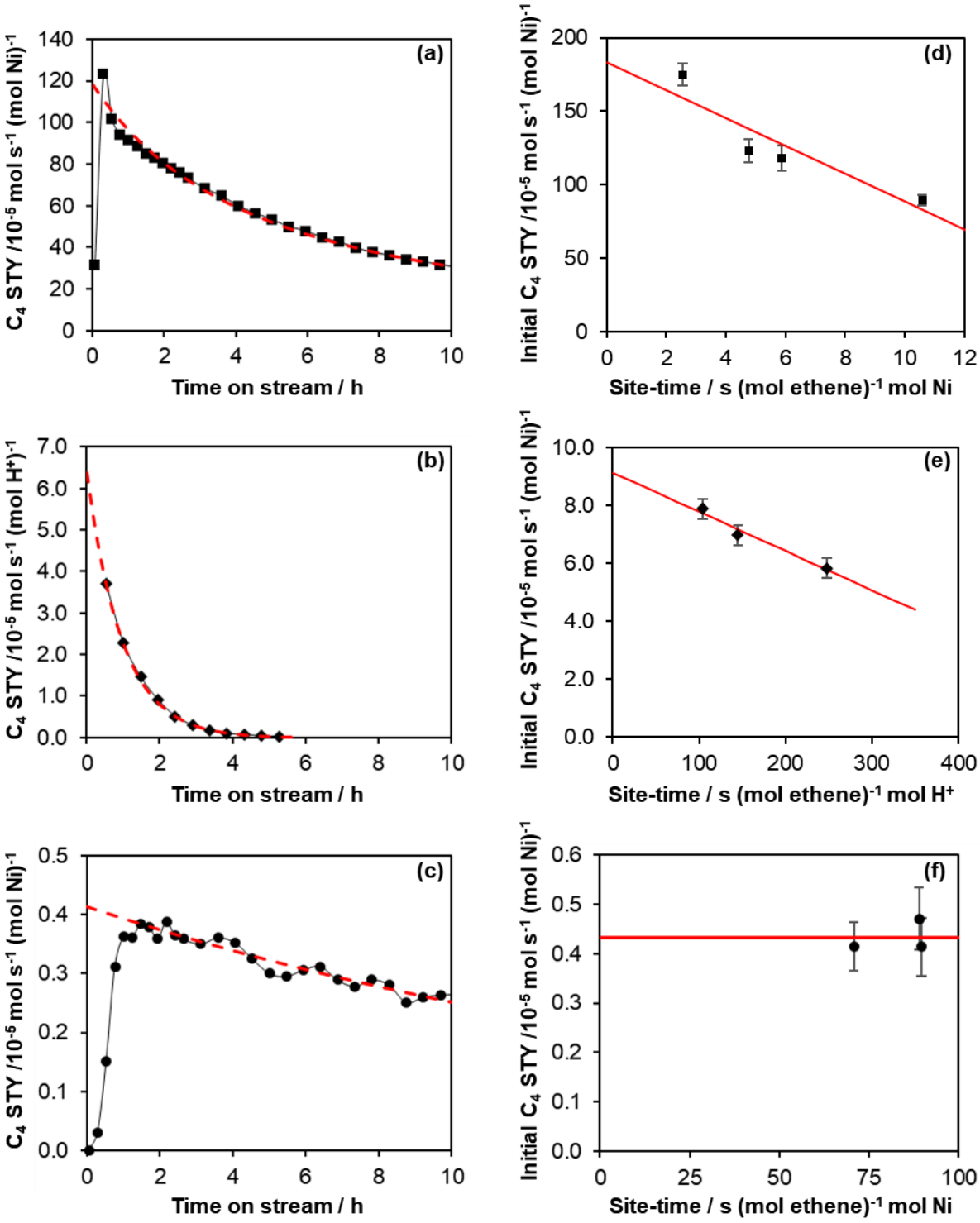

Figure 3.1. Butene site-time yields (STY) measured at 453 K, 0.2 kPa – As a function of reaction time for (a) Ni-Li-[Al]Beta (6 s (mol ethene)$^{-1}$ mol Ni), (b) H-[Al]Beta (120 s (mol ethene)$^{-1}$ mol H^{+}), and (c) Ni-Li-[Zn]Beta (71 s (mol ethene)$^{-1}$ mol Ni). And dependence of initial butene site-time yields on ethene site-time for (d) Ni-Li-[Al]Beta, (e) H-[Al]Beta, and (f) Ni-Li-[Zn]Beta. Dashed red lines indicate predicted values using deactivation models and solid red lines indicate fitted trendlines for extrapolation.

involves more than one site, while those for H-[Al]Beta (Figure 3.1b) and Ni-Li-[Zn]Beta (Figure 3.1c) exhibited a first-order (exponential) decay suggesting a single-site deactivation process. The Ni-Li-[Zn]Beta exhibited an activation transient (Figure 3.1c) during initial reaction times for all ethene pressures (0.05-1 kPa), while such an activation transient was not observed for the H-[Al]Beta support (Figure 3.1b). The Ni-Li-[Al]Beta also exhibited an activation transient, which diminished with increasing ethene pressure and disappeared at pressures greater than 0.4 kPa (Chapter 2, Figure 2.6). These activation transients reflect the transformation of Ni into the coordination-insertion active sites [145] (Chapter 2, Section 2.3.4) concurrent with their deactivation. On the other hand, the deactivation transients solely reflect changes related to deactivation of the active sites. Thus, in the case of C_4 site-time yields that showed an activation transient, the initial C_4 site-time yields were estimated by fitting exponential or hyperbolic decay models (Derivation in Section 3.6.2, Supporting Information) to the data points corresponding to the deactivation transient, as shown in Figure 3.1a-c.

Further, the initial C_4 site-time yields were estimated at varying ethene site-time velocities and extrapolated to zero site-time (solid red line) for Ni-Li-[Al]Beta, H-[Al]Beta, and Ni-Li-[Zn]Beta, as shown respectively in Figures 3.1d-f for 0.2 kPa ethene, and in Section 3.6.4, Supporting Information for other ethene pressures. The initial C_4 site-time yields decreased with increasing site-time for Ni-Li-[Al]Beta (Figure 3.1d) and H-[Al]Beta (Figure 3.1e), consistent with the consumption of butenes in secondary reactions such as cracking, oligomerization and those leading to the deactivation of these samples. On the other hand, the C_4 site-time yields were invariant with site-time for Ni-Li-[Zn]Beta (Figure 3.1f), suggesting minimal extent of secondary reactions of butenes at lower ethene conversions. The initial C_4 site-time yields extrapolated to zero site-time, reflect the initial rates of C_4 formation in the absence of secondary reactions and thus represent the initial ethene dimerization rates. Table 3.1 shows the initial ethene dimerization rates measured on Ni-Li-[Al]Beta, H-[Al]Beta, and Ni-Li-[Zn]Beta at 453 K and 0.2 kPa ethene. The initial ethene dimerization rate was 20 times higher on Ni-Li-[Al]Beta than that on the H-[Al]Beta support and therefore, the rates measured on Ni-Li-[Al]Beta reflect dimerization turnovers at exchanged Ni^{2+} cations, while the contributions from the *in-situ* generated H^+ sites (Chapter 2, Section 2.3.4) are insignificant.

Table 3.1. Initial ethene dimerization rates measured at 453 K and 0.2 kPa ethene

Sample	Initial ethene dimerization rate / 10^{-5} mol s^{-1} (mol site*)$^{-1}$
H-[Al]Beta	9.16
Ni-Li-[Zn]Beta	0.43
Ni-Li-[Al]Beta	183.47

*site – H^+ for H-[Al]Beta, Ni for Ni-Li-[Zn]Beta and Ni-Li-[Al]Beta

3.3.3 Effect of Ni site structure on ethene dimerization

As discussed in Chapter 2, the coordination-insertion catalytic cycle for Ni-exchanged Beta zeolites is initiated by *in-situ* formation of $[Ni(II)\text{-}H]^+$ (Ni-hydrides) from Ni^{2+} cations. Scheme 3.1. shows the coordination-insertion mechanism, wherein the β-hydride elimination steps (5 and 9) to desorb butenes are preceded by the coordination of ethene because the desorption of butenes from β-agostic $[Ni(II)\text{-}(1\text{-butyl})]^+$ and $[Ni(II)\text{-}(2\text{-butyl})]^+$ to form a $[Ni(II)\text{-}H]^+$ (Ni-hydride) was calculated to be highly endothermic [59, 146]. This mechanistic detail implies that the $[Ni(II)\text{-}H\text{-}ethene]^+$ is the catalytic active site while the $[Ni(II)\text{-}H]^+$ (Ni-hydride) serves as a precursor to its formation. Further, the free energy profile (Figure 3.3, Supporting Information) for ethene dimerization (393 K, 1 bar) via the coordination-insertion mechanism on Ni-AFI was calculated (BEEF-vdW) by Brogaard and Olsbye [59], which indicates the highest energy transition state to be involved in the formation of β-agostic $[Ni(II)\text{-}(1\text{-butyl})]^+$ from $[Ni(II)\text{-ethyl-ethene}]^+$ (step 3). Also, this elementary step involves the highest intrinsic free energy barrier (68 kJ mol^{-1}) relative to all other elementary steps and therefore it is considered kinetically-relevant with the other elementary steps to be quasi-equilibrated. These mechanistic considerations were applied to derive the rate expression (Section 3.6.3, Supporting Information) in equation 3.1 for ethene dimerization, wherein the coverage terms (in the denominator) respectively correspond to the $[Ni(II)\text{-H-ethene}]^+$, β-agostic $[Ni(II)\text{-ethyl}]^+$ and $[Ni(II)\text{-ethyl-ethene}]^+$ intermediates.

$$\frac{r_{dim}}{[Ni(II)-H-ethene]^+} = \frac{k_3 K_2 K_1 P_{ethene}}{1 + K_1 + K_2 K_1 P_{ethene}} \qquad (3.1)$$

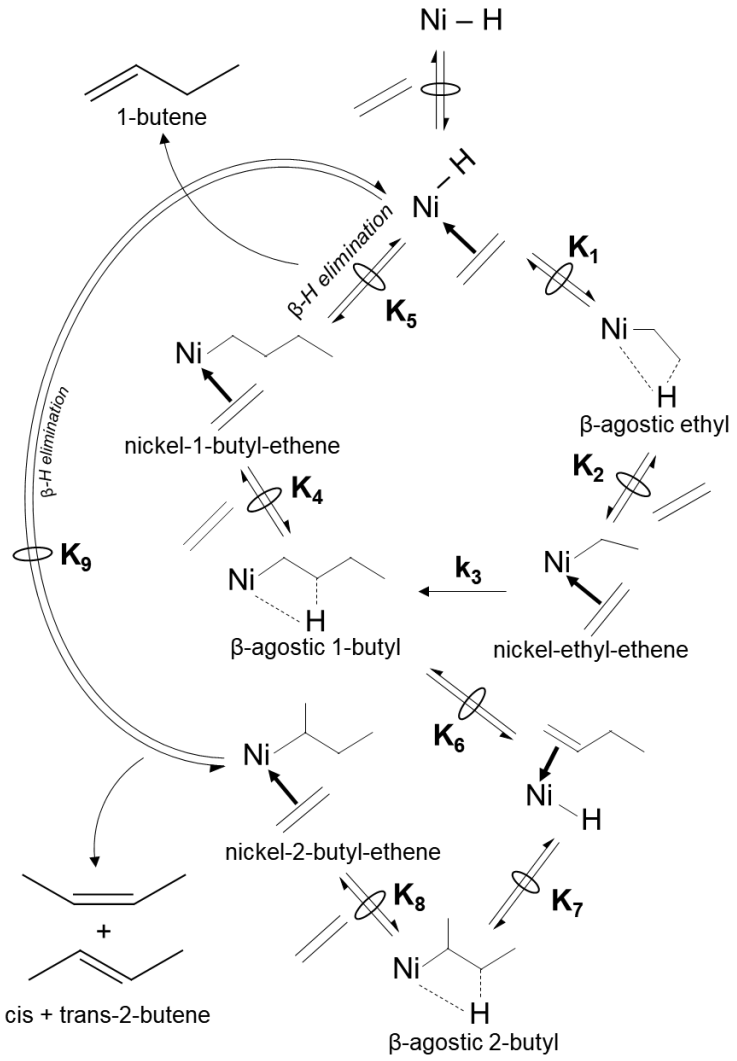

Scheme 3.1. Coordination-insertion catalytic cycle with mechanistic assumptions for elementary steps. Ni exhibits a formal oxidation state of +2 for all intermediates.

DFT calculations showed the β-agostic $[Ni(II)\text{-}ethyl]^+$ to adopt an approximately square-planar structure while the $[Ni(II)\text{-}ethyl\text{-}ethene]^+$ adopts a tetrahedral orientation around the Ni(II) center. The Ni metal center is present in a 2+ oxidation state throughout the coordination-insertion cycle and thus exhibits an d^8 electronic configuration. Further, cationic Ni(II) with d^8 configuration is known to prefer a square-planar structural configuration in the presence of strong field ligands like a hydride or alkyl [147, 148]. This is also reflected in the DFT-calculated free energies (Figure 3.3, Supporting Information) that show the β-agostic $[Ni(II)\text{-}ethyl]^+$ to be more stable than the $[Ni(II)\text{-}ethyl\text{-}ethene]^+$ intermediates for exchanged Ni^{2+} cations in AFI [59]. These considerations suggest the β-agostic $[Ni(II)\text{-}ethyl]^+$ to be the most abundant reaction intermediate (MARI) and

under conditions of dilute ethene, equation 3.1 simplifies into a first-order rate law shown by equations 3.2 and 3.3 –

$$\frac{r_{dim}}{[Ni(II)-H-ethene]_o^+} = k_3 K_2 P_{ethene} \quad (3.2)$$

$$\frac{r_{dim}}{[\mathrm{Ni(II)-H-ethene}]_o^+} = k_{app} P_{ethene} \quad (3.3)$$

In order to investigate the influence of Ni site structures on dimerization catalysis, initial ethene dimerization rates (453 K) were measured at dilute ethene pressures (0.05-1 kPa) for Ni-Li-[Al]Beta and Ni-Li-[Zn]Beta samples that respectively contain exchanged Ni^{2+} cations and grafted Ni^{2+} cations, and these data are shown in Figure 3.2. Both Ni-Li-[Al]Beta and Ni-Li-[Zn]Beta show an apparent first order dependence of initial dimerization rates on ethene pressure, suggesting the predominance of β-agostic $[Ni(II)\text{-ethyl}]^+$ intermediates according to the

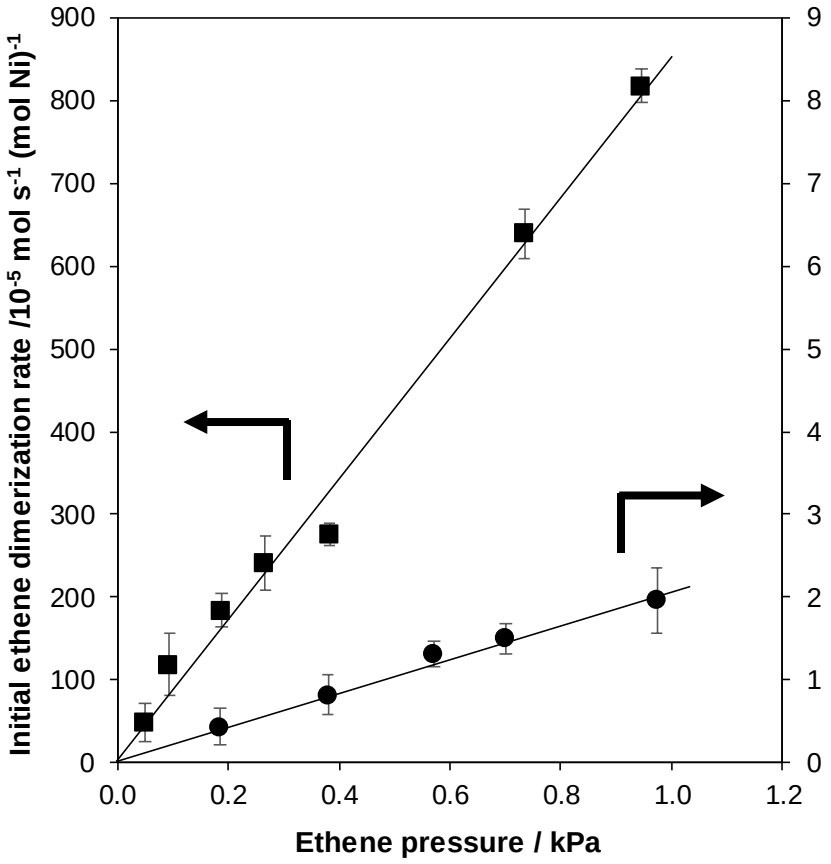

Figure 3.2. Dependence of initial ethene dimerization rates on ethene pressure at 453 K for Ni-Li-[Al]Beta (■) and Ni-Li-[Zn]Beta (●)

mechanism derived rate law (Equations 3.2 and 3.3). A similar first order dependence was also reported by Ng and Creaser [29] for ethene dimerization (323-343 K, 7-40 bar) on Ni-Na-Y zeolite and by Mlinar et al. [32] for propene dimerization (453 K, 1-5 bar) on Ni-X zeolites using a reaction kinetic model. In contrast, Henry et al. [33] reported a second order dependence of ethene consumption rates (393 K, 11.6 – 25.1 bar) on ethene pressure for Ni-exchanged Beta zeolites. This could possibly be a result of the kinetic data analysis procedure, wherein the reaction order was determined using the transient deactivation data (corrected for deactivation) after the ethene conversion had dropped to half of its initial value [33]. Thus, such data considered for the reaction order analysis does not reflect the dimerization turnovers on all Ni sites.

Further, Table 3.2 shows that the apparent first order rate constant for Ni-Li-[Al]Beta is nearly two orders of magnitude higher than that for Ni-Li-[Zn]Beta, which reflects the differences between the ethene adsorption energies or intrinsic dimerization activation enthalpies on the exchanged and the grafted Ni^{2+} cations. The measurement of activation enthalpies on these materials will further clarify the difference in reactivity of the exchanged and grafted Ni^{2+} cations for ethene dimerization.

Table 3.2. Apparent first order dimerization rate constants at 453 K

Sample	First order dimerization rate constant / 10^{-5} mol s^{-1} kPa^{-1} (mol Ni)$^{-1}$
Ni-Li-[Zn]Beta	2.1
Ni-Li-[Al]Beta	860.3

3.4 Conclusions and outlook

Ni site structures such as $NiOH^+$, undercoordinated Ni^{2+} cations on NiO particle surfaces, and exchanged and grafted Ni^{2+} cations have been proposed as the active site precursors for ethene dimerization, with conflicting proposals about their intrinsic reactivities. To clarify the site requirements, Beta zeotypes containing predominantly exchanged Ni^{2+} cations or grafted Ni^{2+} cations were synthesized as control materials, and their Ni site structures were verified by CO infrared, diffuse reflectance UV-vis and X-ray absorption spectroscopies.

Further, the efforts to measure ethene dimerization turnover rates on Ni-containing microporous and mesoporous solids are complicated by temporal changes to the Ni site structures caused by catalyst activation and deactivation. Thus, the measured butene site-time yields were extrapolated to initial time using hyperbolic or exponential deactivation models to determine reaction kinetic data representative of the initial number and structure of the Ni sites as determined by *ex-situ* characterization. Exchanged Ni^{2+} cations exhibited hyperbolic deactivation transients indicating the involvement of more than one site in each deactivation event, while grafted Ni^{2+} cations showed exponential deactivation transients indicative of single-site deactivation. The consumption of alkene dimers (butenes) in secondary reactions was captured by the ethene site-time variation experiments, and the initial ethene dimerization rates were rigorously determined by extrapolation of initial butene site-time yields to zero site-time.

The dimerization turnover rates (per total Ni) on both exchanged and grafted Ni^{2+} cations showed a first order dependence on ethene pressure. This first order dependence together with the prevalence of coordination-insertion mechanism implied the β-agostic $[Ni(II)\text{-ethyl}]^+$ complex to be the most abundant reaction intermediate under these conditions. Exchanged Ni^{2+} cations exhibited an apparent first-order rate constant (453 K) that was nearly two orders of magnitude higher than that for the grafted Ni^{2+} cations, suggesting significant differences in the ethene adsorption enthalpies or the intrinsic reaction enthalpies of dimerization at these sites.

The differences in the intrinsic reactivities of exchanged Ni^{2+}, grafted Ni^{2+} and $NiOH^+$ cations can be conclusively determined by measurement of dimerization activation energies within the same kinetic regime. Unlike exchanged and grafted Ni^{2+} cations, there are no direct probes reported for the characterization of $NiOH^+$ cations, and their development is necessary. Also, given the lack of precise control over Ni speciation during the synthesis of these materials, it would be beneficial to employ techniques such as H_2-D_2 exchange to quantify the fraction of Ni sites that can be transformed into the catalytically active Ni-hydride intermediates [145]. Current literature reports [32, 149] have indicated alkene dimerization rates (per Ni) vary with changing Ni density, and thus quantitative measurements of active Ni sites will enable accurate determination of whether dimerization turnover rates are independent of Ni density.

3.5 Acknowledgements

I would like to thank Elsa Koninckx (Northwestern University) for writing the python code to fit the deactivation models and for being patient with my incessant requests for improvising the same.

3.6 Supporting Information

3.6.1 DFT calculated free energy profile for coordination-insertion mechanism

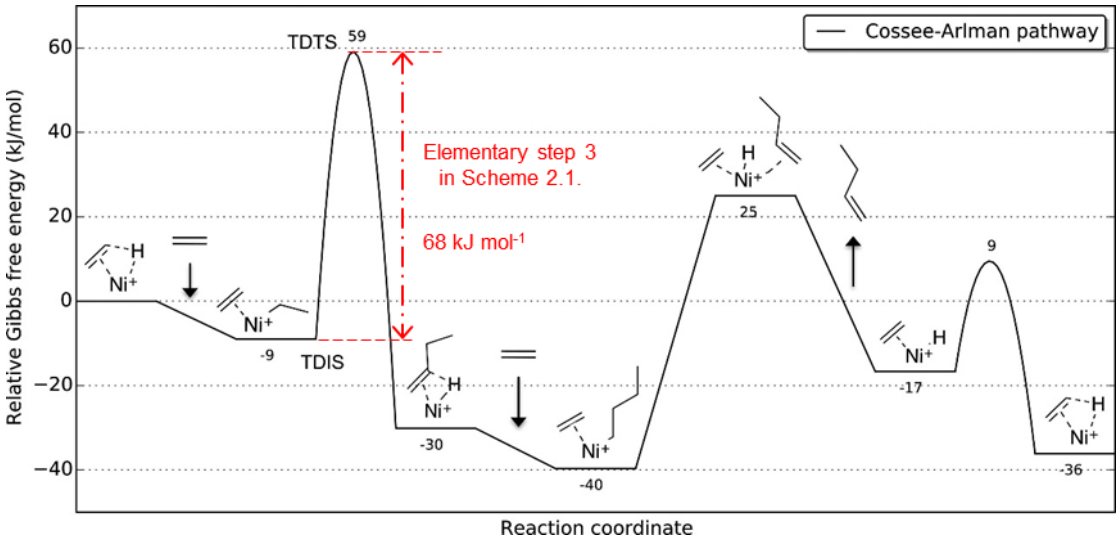

Figure 3.3. Calculated free energy profile (Ni-AFI, 393 K, 1 bar, BEEF-vdW) for ethene dimerization via coordination-insertion mechanism. Adapted with permission from Brogaard and Olsbye [59].

3.6.2 Derivation of deactivation models

3.6.2.1 Multi-site (hyperbolic) deactivation model

The hyperbolic deactivation model was derived using the methods described by John Butt [142]. Consider the following definitions for the terms –

N_o → Number of active sites at time = 0

N_p → Number of sites poisoned

k → Intrinsic deactivation constant

n → Order of deactivation

The rate of poisoning of sites is denoted by equation 3.4, which is related to the number of un-poisoned sites as per equation 3.5 –

$$\frac{dN_p}{dt'} = Rate\ of\ poisoning \tag{3.4}$$

$$\frac{dN_p}{dt'} = k\left(N_o - N_p\right)^n \tag{3.5}$$

Let, f be the fraction of sites active –

$$f = \frac{\left(N_o - N_p\right)}{N_o} \tag{3.6}$$

$$N_p = N_o(1 - f) \tag{3.7}$$

$$\left(N_o - N_p\right) = fN_o \tag{3.8}$$

Using equations 3.7 and 3.8, equation 3.5 can be rewritten as –

$$\frac{df}{dt'} = -k{N_o}^{n-1}f^n \tag{3.9}$$

At time $= 0$, $f = 1$ and if F is the fraction sites active at time t, equation 3.9 is integrated as –

$$\int_1^F \frac{df}{f^n} = -k{N_o}^{n-1}\int_0^t dt' \tag{3.10}$$

$$\frac{F^{1-n} - 1}{1 - n} = -k{N_o}^{n-1}t \tag{3.11}$$

$$F^{1-n} = 1 + (n-1)k{N_o}^{n-1}t \tag{3.12}$$

$$F = \left[1 + (n-1)k{N_o}^{n-1}t\right]^{\left(\frac{1}{1-n}\right)} \tag{3.13}$$

$$F = \frac{1}{\left[1 + (n-1)k{N_o}^{n-1}t\right]^{\left(\frac{1}{n-1}\right)}} \tag{3.14}$$

Considering mean-field kinetics, the fraction of sites active at time t (F) is equal to ratio of site-time yield (Y) at time t to the initial site-time yield (Y_o) –

$$F = \frac{Y}{Y_o} \tag{3.15}$$

$$Y = \frac{Y_o}{\left[1 + (n-1)k{N_o}^{n-1}t\right]^{\left(\frac{1}{n-1}\right)}} \tag{3.16}$$

Here, N_o represents the number of catalytically active sites at initial time at a given temperature and pressure, which can only be estimated accurately by *in-situ* titration of active sites, a difficult feat to be achieved in the case of deactivating catalytic systems. Therefore, an apparent deactivation model expression was derived considering n[th] order decay of the site-time yields (y) to estimate the term $k{N_o}^{n-1}$ in equation 3.16.

$$\frac{dy}{dt'} = -k_d y^n \tag{3.17}$$

At time $= 0$, y $= Y_o$

$$\int_{Y_o}^{Y} \frac{dy}{y^n} = -k_d \int_0^t dt' \tag{3.18}$$

$$\frac{Y^{1-n} - Y_o^{1-n}}{1-n} = -k_d t \tag{3.19}$$

$$Y^{1-n} = Y_o^{1-n} + (n-1)k_d t \tag{3.20}$$

$$Y = [Y_o^{1-n} + (n-1)k_d t]^{\left(\frac{1}{1-n}\right)} \tag{3.21}$$

$$Y = Y_o\left[1 + (n-1)k_d {Y_o}^{-(1-n)}t\right]^{\left(\frac{1}{1-n}\right)} \tag{3.22}$$

$$Y = Y_o\left[1 + (n-1)k_d Y_o^{(n-1)}t\right]^{\left(\frac{1}{1-n}\right)} \tag{3.23}$$

$$Y = \frac{Y_o}{\left[1 + (n-1)k_d {Y_o}^{(n-1)}t\right]^{\left(\frac{1}{n-1}\right)}} \tag{3.24}$$

Comparing equations 3.16 and 3.24 –

$$k{N_o}^{n-1} = k_d {Y_o}^{(n-1)} \tag{3.25}$$

$$k_d = k\left(\frac{N_o}{Y_o}\right)^{n-1} \tag{3.26}$$

Thus, in terms of the apparent deactivation constant (k_d), the site-deactivation phenomenon reflected by equation 3.16 can also be represented by equation 3.26. Thus, the equation 3.27 was used to fit the hyperbolic deactivation transients –

$$Y = \frac{Y_o}{\left[1 + (n-1)k_d {Y_o}^{(n-1)} t\right]^{\left(\frac{1}{n-1}\right)}} \tag{3.27}$$

3.6.2.2 Single-site (exponential) deactivation model

Consider a first order decay of the site-time yields (y) as shown by equation 3.28, where k_d is the apparent deactivation constant

$$\frac{dy}{dt'} = -k_d y \tag{3.28}$$

At time $= 0$, y $= Y_o$

$$\int_{Y_o}^{Y} \frac{dy}{y} = -k_d \int_{0}^{t} dt' \tag{3.29}$$

$$ln\left(\frac{Y}{Y_o}\right) = -k_d t \tag{3.30}$$

$$Y = Y_o e^{-k_d t} \tag{3.31}$$

The equation 3.31 was used to fit the exponential deactivation transients

3.6.3 Mechanism derived rate expression

The coordination-insertion mechanism shown in Scheme 3.1 is rewritten in Scheme 3.2 with the individual rate constants for the steps involved. As discussed in Section 3.3.3, the formation of β-agostic [Ni(II)-(1-butyl)]$^+$ from [Ni(II)-ethyl-ethene]$^+$ (step 3) is kinetically-relevant with the other elementary steps to be quasi-equilibrated.

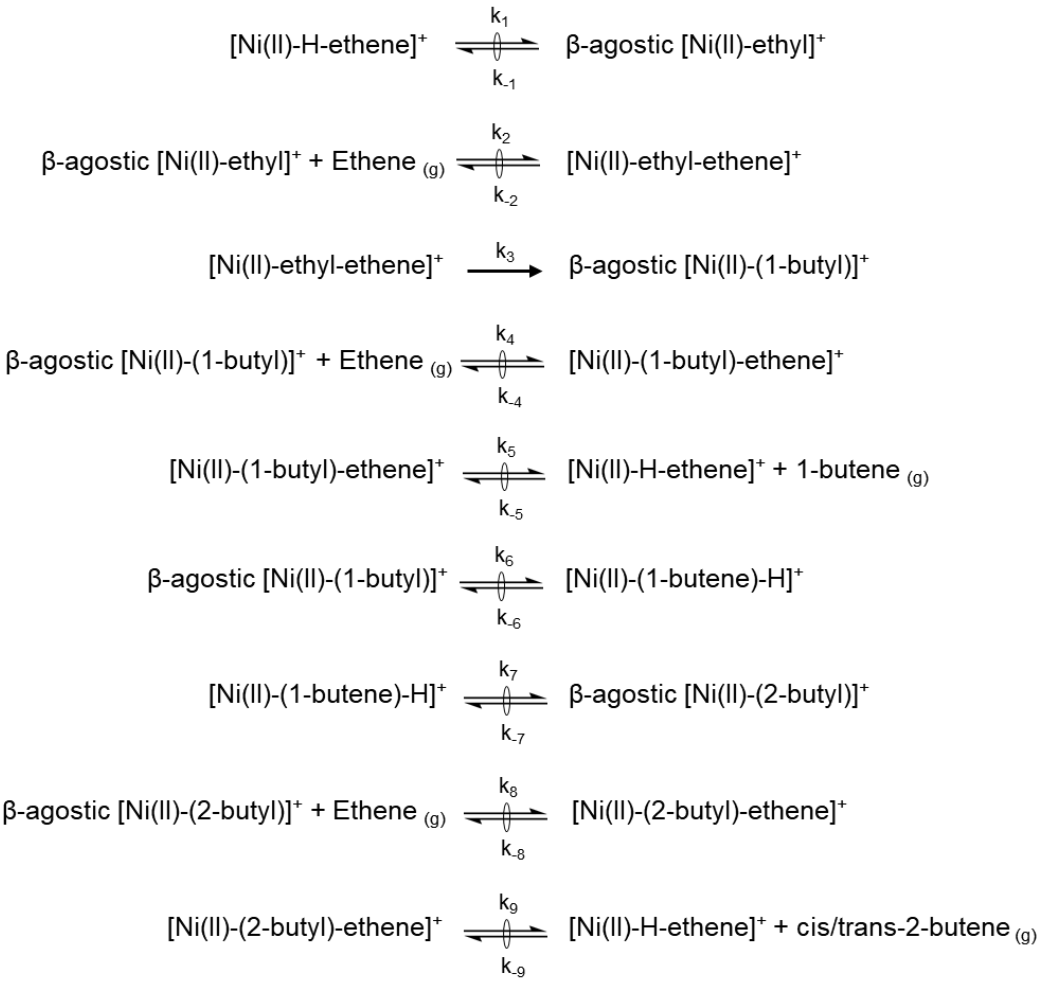

Scheme 3.2. Sequence of elementary steps for the coordination-insertion catalytic cycle with mechanistic assumptions. Ni exhibits a formal oxidation state of +2 for all intermediates.

The surface concentrations of the intermediates and the pressures of the gases involved in the elementary steps shown in Scheme 3.2 are expressed using the following notation for the purpose of mathematical derivation –

[Ni(II)-H-ethene]$^+$ = $[\mathrm{H}-\mathrm{Et}]$

β-agostic [Ni(II)-ethyl]$^+$ = $[\beta\mathrm{AEC}]$

Ethene (g) = P_{Et}

[Ni(II)-ethyl-ethene]$^+$ = $[\mathrm{Ety}-\mathrm{Et}]$

β-agostic [Ni(II)-(1-butyl)]$^+$ = $[1-\beta\mathrm{ABC}]$

[Ni(II)-(1-butyl)-ethene]$^+$ = $[1-\text{Buty}-\text{Et}]$

[Ni(II)-(1-butene)-H]$^+$ = $[\text{Bt}-\text{H}]$

β-agostic [Ni(II)-(2-butyl)]$^+$ = $[2-\beta\text{ABC}]$

[Ni(II)-(2-butyl)-ethene]$^+$ = $[2-\text{Buty}-\text{Et}]$

1-butene (g) = P_{1-but}

cis-2-butene (g) + trans-2-butene (g) = P_{2-but}

Considering the kinetically-relevant step, the rate of dimerization is given by equation 3.32 as shown below –

$$r_{dim} = k_3[\text{Ety}-\text{Et}] \tag{3.32}$$

Pseudo steady-state assumption for [Ni(II)-ethyl-ethene]$^+$ -

$$k_2[\beta\text{AEC}]P_{Et} = (k_{-2}+k_3)[\text{Ety}-\text{Et}] \tag{3.33}$$

$$[\text{Ety}-\text{Et}] = K_2[\beta\text{AEC}]P_{Et} \qquad \ldots\ldots (k_3 \ll k_{-2}) \tag{3.34}$$

Quasi equilibrium for step 1 implies –

$$[\beta\text{AEC}] = K_1[\text{H}-\text{Et}] \tag{3.35}$$

Combining equations 3.32, 3.34 and 3.35 –

$$r_{dim} = k_3K_2K_1[\text{H}-\text{Et}]P_{Et} \tag{3.36}$$

Site balance for the dimerization active sites is given by equation 3.37 as shown below –

$$[\text{H}-\text{Et}]_o = [\text{H}-\text{Et}] + [\beta\text{AEC}] + [\text{Ety}-\text{Et}] + [1-\beta\text{ABC}] + [1-\text{Buty}-\text{Et}] + [\text{Bt}-\text{H}] + [2-\beta\text{ABC}] + [2-\text{Buty}-\text{Et}] \tag{3.37}$$

Quasi equilibrium for step 4 implies –

$$[1 - \beta ABC] = \frac{[1 - \text{Buty} - \text{Et}]}{K_4 P_{Et}} \tag{3.38}$$

Quasi equilibrium for step 5 implies –

$$[1 - \text{Buty} - \text{Et}] = \frac{[\text{H} - \text{Et}]\text{P}_{1-\text{but}}}{\text{K}_5} \tag{3.39}$$

Quasi equilibrium for step 6 implies –

$$[\text{Bt} - \text{H}] = K_6[1 - \beta ABC] \tag{3.40}$$

$$[1 - \beta ABC] = \frac{[\text{Bt} - \text{H}]}{K_6} \tag{3.41}$$

Quasi equilibrium for step 7 implies –

$$[\text{Bt} - \text{H}] = \frac{[2 - \beta ABC]}{K_7} \tag{3.42}$$

Quasi equilibrium for step 8 implies –

$$[2 - \beta ABC] = \frac{[2 - \text{Buty} - \text{Et}]}{K_8 P_{Et}} \tag{3.43}$$

Quasi equilibrium for step 9 implies –

$$[2 - \text{Buty} - \text{Et}] = \frac{[\text{H} - \text{Et}]P_{2-but}}{K_9} \tag{3.44}$$

Combining equations 3.38 and 3.39 gives –

$$[1 - \beta ABC] = \frac{[\mathrm{H} - \mathrm{Et}]P_{1-but}}{K_4 K_5 P_{Et}} \tag{3.45}$$

Combining equations 3.43 and 3.44 gives –

$$[2 - \beta ABC] = \frac{[\mathrm{H} - \mathrm{Et}]P_{2-but}}{K_8 K_9 P_{Et}} \tag{3.46}$$

Combining equations 3.42 and 3.46 gives –

$$[\mathrm{Bt} - \mathrm{H}] = \frac{[\mathrm{H} - \mathrm{Et}]P_{2-but}}{K_7 K_8 K_9 P_{Et}} \tag{3.47}$$

Combining equations 3.41 and 3.47 gives –

$$[1 - \beta ABC] = \frac{[\mathrm{H} - \mathrm{Et}]P_{2-but}}{K_6 K_7 K_8 K_9 P_{Et}} \tag{3.48}$$

Rewriting the site-balance (equation 3.37) using the equations 3.35, 3.34, 3.48, 3.39, 3.47, 3.46 and 3.44 –

$$[\mathrm{H} - \mathrm{Et}]_o = [\mathrm{H} - \mathrm{Et}] + K_1[\mathrm{H} - \mathrm{Et}] + K_2 K_1[\mathrm{H} - \mathrm{Et}]\, P_{Et} + \frac{[\mathrm{H} - \mathrm{Et}]P_{2-but}}{K_6 K_7 K_8 K_9 P_{Et}} + \frac{[\mathrm{H} - \mathrm{Et}]P_{1-but}}{K_5} + \frac{[\mathrm{H} - \mathrm{Et}]P_{2-but}}{K_7 K_8 K_9 P_{Et}} + \frac{[\mathrm{H} - \mathrm{Et}]P_{2-but}}{K_8 K_9 P_{Et}} + \frac{[\mathrm{H} - \mathrm{Et}]P_{2-but}}{K_9} \tag{3.49}$$

Under conditions of differential ethene conversion (< 5%), $P_{2-but}, P_{1-but} \ll P_{Et}$, which simplifies equation 3.49 to equation 3.50 –

$$[\mathrm{H} - \mathrm{Et}]_o = [\mathrm{H} - \mathrm{Et}] + K_1[\mathrm{H} - \mathrm{Et}] + K_2 K_1[\mathrm{H} - \mathrm{Et}]P_{Et} \tag{3.50}$$

Therefore,

$$[\mathrm{H}-\mathrm{Et}] = \frac{[\mathrm{H}-\mathrm{Et}]_o}{1 + K_1 + K_2 K_1 P_{Et}} \tag{3.51}$$

Using equation 3.51 into equation 3.36 –

$$\frac{r_{dim}}{[\mathrm{H}-\mathrm{Et}]_o} = \frac{k_3 K_2 K_1 P_{Et}}{1 + K_1 + K_2 K_1 P_{Et}} \tag{3.52}$$

3.6.4 Effect of site-time on initial C_4 site-time yields

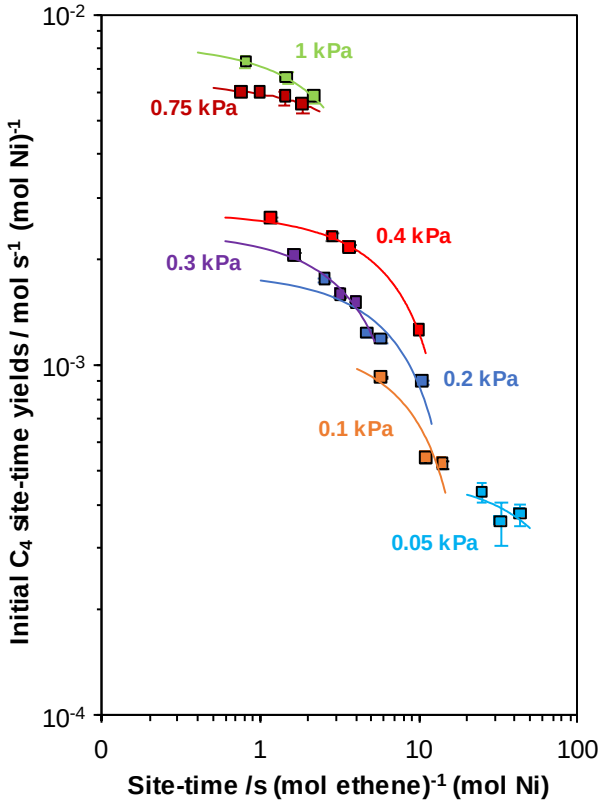

Figure 3.4. Log-log plot of initial butene (C_4) site-time yields (453 K) as a function of ethene site-time for Ni-Li-[Al]Beta at 0.05 (light blue), 0.1 (orange), 0.2 (dark blue), 0.3 (purple), 0.4 (red), 0.75 (dark red) and 1 kPa (light green) ethene. The solid lines show the fitted linear trendlines for extrapolation.

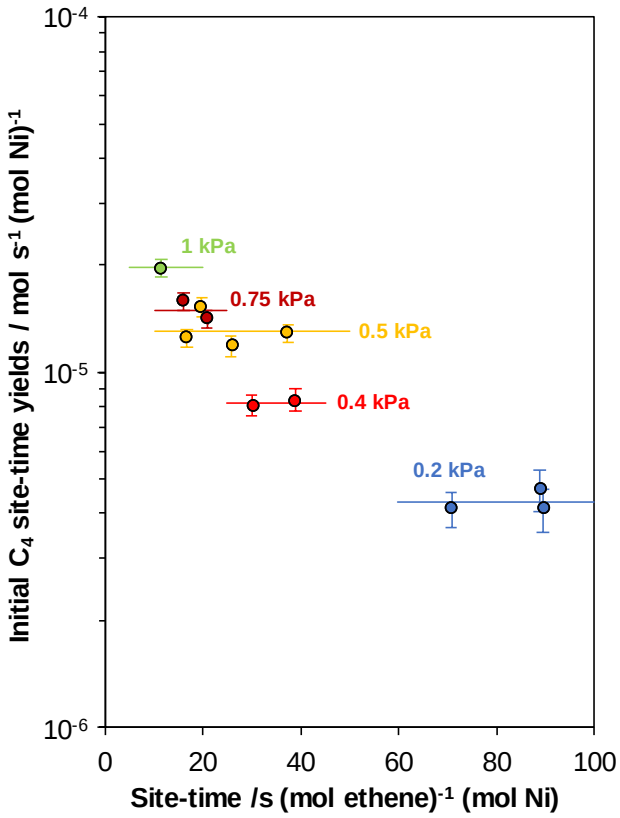

Figure 3.5. Semi-log plot of initial butene (C_4) site-time yields (453 K) as a function of ethene site-time for Ni-Li-[Zn]Beta at 0.2 (dark blue), 0.4 (red), 0.5 (yellow), 0.75 (dark red) and 1 kPa (light green) ethene. The solid lines show the fitted linear trendlines for extrapolation.

3.6.5 Python code to fit deactivation model parameters

The python code below takes an Excel file as input with the columns containing time vs. site-time yield data. The output is a new Excel file with the fitted deactivation model data along with the values for model parameters and the standard deviations within the same.

```
# In[1]:


import pandas as pd
import numpy as np
from scipy.optimize import curve_fit
from scipy import stats

import matplotlib.pyplot as plt
import matplotlib.ticker as mtick
from matplotlib.pyplot import cm
from matplotlib import colors


# First, let's input the data and setup our x (time) and y (species
flow rates) arrays.

# In[2]:


inputexcel = '190408 Ni-Li-Beta Site-time yields compiled.xlsx' #ENTER
EXCEL NAME HERE
inputsheet = '5-86.8 STY measured' #ENTER SHEET NAME HERE

skipbeginpoints = 5; #MAX number of points to possibly skip at
beginning
skipendpoints = 0; #number of points to skip at end

ws = pd.read_excel(inputexcel, sheet_name=inputsheet)
headerstr = list(ws.head(0))
data = np.array(ws)
speciestr = list(data[0])
data = np.delete(data,0,0)
data = np.delete(data,0,0)

data = data.T #Now in format of data = [Ethane data[], Propene data[],
...]

timenp = data[0:2] #x np array
newtime = np.linspace(0,timenp[1,-1], num=len(timenp[1])) #for
printing initial time points - used in graphing
speciesnp = data[2::] #y np array
```

```
#reformat column header list
speciestr = [x for x in speciestr if str(x) != 'nan']
speciestr.insert(0,str(headerstr[2])) #species headers
timestr = headerstr[0:2] #time headers
stystr = headerstr[3] #STY header


# We'll first try to fit using the hyperbolic, mulitsite deactivation
curve. If this doesn't appear to be working (R^2 < 0.97), then we'll
fit it to the exponential decay, single site deactivate curve.

# In[3]:


def funcapp(x, y0, k, n): #apparent catalytic deactivation
    return (y0/((1+(n-1)*k*(y0**(n-1))*x)**(1/(n-1))))

def expdec(x, y0, k): #exponential decay
    return (y0*np.exp(-k*x))


# In[9]:


#the maximum STY for each species
maxvales = np.amax(speciesnp, axis=1)

#initiate arrays and lists to populate
popt = np.empty((0,3), float) #fitted parameters
perr = np.empty((0,3), float) #standard deviate/error of parameters
chisq = [] #X^2 values
pval = [] #p values
rsq = [] #R^2 values
exceptions = [] #list of exceptions from hyperbolic, must use exp
decay

for i, sp in enumerate(speciesnp): #loop through each species
    if maxvales[i] < 1.0e-4: #if largest value is less than 1e-4,
rescale with initial guess to be 1
        scale = maxvales[i]
        maxvales[i] = 1
    else:
        scale = 1

    r_squared = 0.0
    n = 0

    while r_squared < 0.97 and n <= skipbeginpoints: #Try to fit the
hyperbolic apparent function. Remove an additional initial point each
run to gain a better fit.
```

```
        timecrop = np.array(timenp)[::,n:] #crop time points to take
into account skipped points
        spcrop = np.array(speciesnp)[::,n:] #crop STY points to take
into account skipped points

        if skipendpoints != 0:
            timecrop = np.array(timecrop)[::,:-skipendpoints]
            spcrop = np.array(spcrop)[::,:-skipendpoints]/scale
        else:
            spcrop = spcrop/scale

        times = np.array(timecrop[1], dtype=float) #make curve_fit
inputs explicit 1D np float arrays to reduce errors
        rates = np.array(spcrop[i], dtype=float)

        try:
            popti, pcovi = curve_fit(funcapp, times, rates,
p0=(float(rates[0]), 0.0001, 2), bounds=((0,0,
1),(rates[0]*10+0.001,np.inf,5))) #once cropped, use first point as
intial point
            perri = np.sqrt(np.diag(pcovi))

            residuals = spcrop[i]-funcapp(times, *popti) #residuals =
ydata - f(xdata, popt)
            ss_res = np.sum(residuals**2)               # SSres =
SUMi (yi-fi)^2 = SUMi (residualsi)^2
            ss_tot = np.sum((spcrop[i]-np.mean(spcrop[i]))**2) #SStot
= SUMi (yi - ybar)^2
            r_squared = 1 - (ss_res / ss_tot)           #R^2 = 1-
SSres/SStot
            n += 1
        except RuntimeError: #If shape is bad, will not converge and
throw an error. If this happens, we try to remove another point to
reduce initial artifacts
            n += 1

    n = 0
    if r_squared < 0.97: #If fit is still bad, we index to exceptions
list for later
        exceptions.append(i)
        while r_squared < 0.97 and n <= skipbeginpoints: #Try to fit
the exponential decay function. Remove an additional initial point
each run to gain a better fit.
            timecrop = np.array(timenp)[::,n:]
            spcrop = np.array(speciesnp)[::,n:]

            if skipendpoints != 0:
                timecrop = np.array(timecrop)[::,:-skipendpoints]
                spcrop = np.array(spcrop)[::,:-skipendpoints]/scale
            else:
                spcrop = spcrop/scale
```

```
            times = np.array(timecrop[1], dtype=float)
            rates = np.array(spcrop[i], dtype=float)

            popti, pcovi = curve_fit(expdec, times, rates,
p0=(float(rates[0]), 0.0001),
bounds=((0,0),(rates[0]*10+0.001,np.inf)))
            perri = np.sqrt(np.diag(pcovi))

            residuals = spcrop[i]-expdec(times, *popti)
            ss_res = np.sum(residuals**2)
            ss_tot = np.sum((spcrop[i]-np.mean(spcrop[i]))**2)
            r_squared = 1 - (ss_res / ss_tot)
            n += 1

    if i in exceptions: #if exception, use exp decay
        popts = [popti[0]*scale,popti[1]] #rescale fitted parameters
to original scale
        chisqa, pvala = stats.chisquare(expdec(times, *popts),
spcrop[i], ddof=(spcrop.shape[1]-2)) #calculate X^2 and p value, ddof
= # of points fitted - # of parameters fit (y0, k)
        perrs = [perri[0]*scale,perri[1],0.0] #to retain the same
dimensions of popt for hyperbolic and exp decay, we add a 0 for a 1x3
popti and perri always
        popts.append(0.0)

    else: #otherwise, use hyperbolic deactivation
        popts = [popti[0]*scale,popti[1]*scale**(1-popti[2]),popti[2]]
#rescale fitted parameters to original scale,
        perrs = [perri[0]*scale,perri[1]*scale**(1-popti[2]),perri[2]]
##rescale errors to original scale
        chisqa, pvala = stats.chisquare(funcapp(times, *popts),
spcrop[i], ddof=(spcrop.shape[1]-3)) #calculate X^2 and p value, # of
points fitted - # of parameters fit (y0, kd, n)


    popt = np.vstack((popt, popts)) #add to our growing fitten
parameter list
    perr = np.vstack((perr, perrs))
    rsq.append(r_squared)
    chisq.append(chisqa) #add to our growing X and p value list
    pval.append(pvala)


# In[10]:


#Print fitted parameters ----

print('\033[1m'+'Apparent Model Fit'+'\033[0m')

rsqnp = np.array([rsq]) #turn list into array of (11,1) to play nice
with the other arrays
```

```
chisqnp = np.array([chisq])
pvalnp = np.array([pval])

prspeciestr = speciestr.copy()
for i, sp in enumerate(prspeciestr): #mark our species exceptions with
a *
    if i in exceptions:
        prspeciestr[i] = sp + "*"

#combine all output data - parameters
prpopt = np.append(popt, perr, 1)
prpopt = np.append(prpopt, rsqnp.T, 1)
prpopt = np.append(prpopt, chisqnp.T, 1)
prpopt = np.append(prpopt, pvalnp.T, 1)

prpopt = np.vstack((['y0', 'kd', 'n','y0 std dev', 'kd std dev', 'n
std dev', 'r^2 value', 'X^2$ value','p value'], prpopt))

#create data frame (to export to excel)
prspeciestrparam = prspeciestr.copy()
prspeciestrparam.insert(0, 'Parameters')

dfpopt = pd.DataFrame(prpopt.T, columns = [prspeciestrparam])
display(dfpopt)


# In[11]:


#combine all output data - STY
prtime = np.insert(timenp,0,0,1)
data = np.vstack((prtime[0], prtime[1]))

for i, sp in enumerate(speciesnp):
    if i in exceptions:
        run = expdec(np.array(prtime[1], dtype =
float),popt[i,0],popt[i,1])
    else:
        run = funcapp(np.array(prtime[1]), *popt[i])
    data = np.vstack((data, run))

prdata = timestr.copy() + prspeciestr
dfdata = pd.DataFrame(data.T, columns = prdata) #Modeled dataframe
display(dfdata)

prdata2 = timestr.copy() + speciestr
dataexp = np.vstack((timenp,speciesnp))
dfexpdata = pd.DataFrame(dataexp.T, columns = prdata2) #Experimental
dataframe


# In[12]:
```

```
#Export and plot in EXCEL ---
rgbacolors=cm.rainbow(np.linspace(0,1,speciesnp.shape[0]))
hexcolors = [] #split the rainbow into the number of species we have
so we can make pretty plots
for c, color in enumerate(rgbacolors):
    run = colors.to_hex(color)
    hexcolors.append(run) #but excel only likes hex so fine let's
convert everything

outputexcel = inputsheet.replace('measured', 'Modeled.xlsx') #name of
new excel will just add "Modeled" to the old name
outputsheet = 'Site-time Yields Modeled' #name of new sheet

writer = pd.ExcelWriter(outputexcel, engine = 'xlsxwriter',
options={'strings_to_numbers': True})

#write dataframes to excel document
dfdata.to_excel(writer, sheet_name = outputsheet, index=False,
startrow = 1)
dfpopt.to_excel(writer, sheet_name = outputsheet, index=False,
startcol=len(prdata)+1, startrow = 1)
dfexpdata.to_excel(writer, sheet_name = outputsheet, index=False,
startrow = timenp.shape[1]+5)

workbook  = writer.book
worksheet = writer.sheets[outputsheet]

#excel formatting
worksheet.set_column('A:C', 13.5)
worksheet.set_column(len(prdata)+1, len(prdata)+2, 13.5)
format1 = workbook.add_format({'text_wrap': True, 'bold': True,
'align':'center'})
format2 = workbook.add_format({'text_wrap': True, 'bold': True,
'align':'center', 'bottom':True})

#format headers
for col, header in enumerate(prdata):
    worksheet.write(1, col , header , format1)

for col, header in enumerate(prdata):
    worksheet.write(timenp.shape[1]+5, col , header , format1)

for col, header in enumerate(prspeciestrparam):
    worksheet.write(1, col+len(prdata)+1, header , format1)

worksheet.write(1, len(prspeciestrparam)+len(prdata)+1, '' , format1)
worksheet.write(0, 0, 'Modeled Data' , format2)
worksheet.write(timenp.shape[1]+4, 0, 'Experimental Data' , format2)

#create chart
```

```
#categorties: x data | values: data
chart = workbook.add_chart({'type': 'scatter',
                            'subtype': 'smooth_with_markers'})

for i, species in enumerate(speciestr):
    if i == 0: #put conversion on the secondary axis, all other STY go
to the primary axis
        y2 = 1
    else:
        y2 = 0
    chart.add_series({ #Modeled lines
        'name':       'Modeled {}'.format(species),
        'categories': [outputsheet, 2, 1, timenp.shape[1]+2, 1],
#[sheetname, first_row, first_col, last_row, last_col]
        'values':     [outputsheet, 2, i+2, timenp.shape[1]+2, i+2],
        'marker':     {'type': 'none'},
        'line':       {'width': 1.5,
                       'color': '{}'.format(hexcolors[i])},
        'y2_axis': y2
        })

for i, species in enumerate(speciestr):
    if i == 0:
        y2 = 1
    else:
        y2 = 0
    chart.add_series({ #Experimental points
        'name':       '{}'.format(species),
        'categories': [outputsheet, timenp.shape[1]+6, 1,
timenp.shape[1]*2+5, 1],
        'values':     [outputsheet, timenp.shape[1]+6, i+2,
timenp.shape[1]*2+5, i+2],
        'marker':     {'type': 'circle',
                       'size' : 4,
                        'border': {'color': 'black', 'width': 0.5},
                       'fill':   {'color': '{}'.format(hexcolors[i])}
                        },
        'line':   {'none':True},
        'y2_axis': y2
        })

chart.set_x_axis({'name': timestr[1],
                  'name_font': {'size': 10,
                                'bold': False},
                 'major_gridlines': {'visible': False},
                  'min': 0,
                  'max': timenp[1,-1]
                 })
chart.set_y_axis({'name': stystr,
                  'name_font': {'size': 10,
                                'bold':False},
                 'major_gridlines': {'visible': False},
```

```
                })
chart.set_y2_axis({'name': speciestr[0],
                   'name_font': {'size': 10,
                                 'bold': False,
                                'color': '{}'.format(hexcolors[0])},
                'major_gridlines': {'visible': False},
                })

notlist = list(range(0, len(speciestr)-1))
notlist.append(len(speciestr)*2-2)
chart.set_legend({'font': {'size': 9}, 'delete_series': notlist})
chart.set_plotarea({'border': {'color': '#969696', 'width': 1,
'dash_type': 'solid'}})

worksheet.insert_chart(14, len(prdata)+1, chart, {'x_scale': 1.6,
'y_scale': 1.6})

worksheet.merge_range(0, 3, 0, int(len(speciestr)+1), stystr ,
format2)
worksheet.merge_range(timenp.shape[1]+4, 3, timenp.shape[1]+4,
int(len(speciestr)+1), stystr , format2)

writer.save()
writer.close()


# In[13]:


#Plot in python ---------
color=cm.rainbow(np.linspace(0,1,speciesnp.shape[0]))
fig, ax1 = plt.subplots(1, figsize=(10,6))
axes = plt.gca()
axes.set_ylim(bottom=0.) #set rate axis > 0
ax1.set_xlabel(timestr[1])
ax1.set_xlim(0,timenp[1,-1])
ax1.xaxis.set_major_formatter(mtick.FormatStrFormatter('%.1e')) #show
axis numbers in scientific notation
ax1.yaxis.set_major_formatter(mtick.FormatStrFormatter('%.1e'))
ax1.set_ylabel(stystr)
ax1.set_ylim(0,8e-9) #CHANGE THIS TO VIEW WHAT YOU WANT

ax2 = ax1.twinx() #plot conversion on a secondary axis
ax2.set_ylabel(speciestr[0], color = color[0])
ax2.set_ylim(0,26)

for i, sp in enumerate(speciesnp):
    if i == 0:
        ax2.scatter(timenp[1], speciesnp[i],  color=color[i], s=8,
label=speciestr[i]) #plot exp data
        if i in exceptions:
```

```
            ax2.plot(newtime,expdec(np.array(newtime), popt[i,0],
popt[i,1]), color=color[i], label=speciestr[i]+' Model')
        else:
            ax2.plot(newtime,funcapp(np.array(newtime), *popt[i]),
color=color[i], label=speciestr[i]+' Model') #plot fitted line
    else:
        ax1.scatter(timenp[1], speciesnp[i],  color=color[i], s=8,
label=speciestr[i]) #plot exp data
        if i in exceptions:
            ax1.plot(newtime,expdec(np.array(newtime), popt[i,0],
popt[i,1]), color=color[i], label=speciestr[i]+' Model') #plot fitted
line
        else:
            ax1.plot(newtime,funcapp(np.array(newtime), *popt[i]),
color=color[i], label=speciestr[i]+' Model')

ax1.legend(bbox_to_anchor=(1.35,1), loc='upper right', ncol=1)
ax2.legend(bbox_to_anchor=(1.6,1), loc='upper right', ncol=1)

fig.autofmt_xdate()
plt.show()
```

4. REACTION PATHWAYS DURING ETHENE OLIGOMERIZATION ON NICKEL AND ACID SITES IN BETA ZEOLITES

4.1 Introduction

The coordination-insertion mechanism was shown to be the dominant route for ethene dimerization at exchanged Ni^{2+} cations in Beta zeolites in Chapter 2. The coordination-insertion catalytic cycle, however, is required to be initiated by transforming the exchanged Ni^{2+} cations into $[Ni(II)\text{-}H]^+$ intermediates, the mechanism for which is proposed to also form a Brønsted acidic H^+ site in the proximity of the $[Ni(II)\text{-}H]^+$ species [59]. Further, it was shown in Chapter 3 that the first-order rate constant (453 K) for ethene dimerization on the exchanged Ni^{2+} sites is nearly two orders of magnitude higher than that on these Brønsted acid (H^+) sites.

The presence of Brønsted acid (H^+) sites on Ni-containing zeolites and mesoporous aluminosilicates, however, is shown to favor the formation of alkenes heavier than C_4. The Ni cations are reported to catalyze dimerization and co-dimerization pathways of ethene to C_4 and C_6 alkenes, respectively, while the H^+ sites are proposed to predominantly catalyze further oligomerization of C_4 and C_6 alkenes [27, 36, 46]. Also, increasing the number of H^+ sites relative to the Ni sites was observed to favor the formation of branched alkene isomers and that of odd carbon-numbered alkenes [27, 31]. This variation in product composition is attributed to the increase in ethene conversion [31], corresponding to the increase in the relative number of H^+ sites. Also, branched alkene isomers can be formed by secondary stereospecific coordination-insertion events at the Ni sites [113, 149], and thus cannot be solely attributed to the alkene reaction pathways at the H^+ sites. Thus, although the number of H^+ and Ni sites are reported to influence the composition of oligomer products, the mechanistic details of the reaction pathways at these sites are unclear.

Here, we use a control sample of Ni-exchanged Beta zeolite synthesized to contain predominantly exchanged Ni^{2+} cations and virtually no residual H^+ sites but generates one H^+ site per Ni^{2+} cation *in-situ* (453 K), leading to an equimolar density of Ni and H^+ sites. The origins of products from each site type (Ni or H^+) formed during ethene oligomerization at 453 K are probed by determining the parameters of the deactivation models fitted to describe the transient product space-time yields. Further, the composition of the oligomerization products representative of the

initial Ni/H^+ ratio of the catalyst is unambiguously determined by estimating the product selectivities at initial reaction time as a function of ethene conversion. Finally, the reaction pathways in the oligomerization network at the Ni and H^+ sites are systematically probed using the Delplot technique, which distinguishes the primary and secondary products formed. In summary, the site origins and the reaction pathways determined for the formation of oligomerization products clarify the mechanistic details for designing bifunctional catalysts for alkene oligomerization.

4.2 Experimental Methods

4.2.1 Catalyst synthesis and characterization

The Ni-Li-[Al]Beta sample was synthesized using aqueous phase ion-exchange procedures as described in detail in Chapter 2, Section 2.2.1. The elemental composition was determined by atomic absorption spectroscopy (AAS), the Ni speciation was determined by CO infrared spectroscopy (85 K) and the Ni structural geometry was characterized by diffuse reflectance UV-visible (DRUV) spectroscopy and X-ray absorption spectroscopy. The experimental setup and the procedures for these characterization techniques are described in detail in Chapter 2, Section 2.2.2.

4.2.2 Catalytic reaction measurements

Ethene oligomerization reactions were performed in a plug-flow, fixed-bed quartz reactor heated using a resistive three-zone furnace (Series 3210, Applied Test Systems) controlled by Watlow controllers (EZ-Zone Series). The details of the reactor setup and the procedures for preparing the catalysts samples, pretreatment in oxygen mixture and quantification of the feed mixture can be found in Chapter 3, Section 3.2.2. In this chapter, the specific molar flow rates for ethene are expressed in terms of space-time (h (mol ethene)$^{-1}$ g_{cat}), instead of site-time (h (mol ethene)$^{-1}$ site^{-1}), given the bifunctional composition of the catalysts.

The Ni-Li-[Al]Beta catalyst was treated for 4 hours at 803 K (0.0167 K s^{-1}) in a 5% O_2/95% He mixture (16.7 cm^3 g_{cat}^{-1} s^{-1}, 99.999%, Matheson Tri-Gas) and then cooled to the reaction temperature of 453 K. Following this the catalyst was contacted with a flowing stream of 0.4 kPa ethene prepared by mixing ethene (1% C_2H_4, 5% Ar, 94% He, Matheson Tri-Gas, 99.999% purity)

and He (Pure, Matheson Tri-Gas, 99.999% purity). For each experiment, the ethene space-time was held constant and the product space-time yields were measured as a function of reaction time. The ethene space-times were varied in the range 4-149 h (mol ethene)$^{-1}$ g_{cat} to obtain the product site-time yields over a wide conversion range (1-20%). Between subsequent experiments, the Ni-Li-[Al]Beta sample was regenerated in a 5% O_2/95% He mixture (16.7 cm^3 g_{cat}^{-1} s^{-1}, 99.999%, Matheson Tri-Gas) at 803 K (0.0167 K s^{-1}) for 4 hours and control experiments showed that the regenerated samples exhibited the same reactivity as the fresh sample.

The conversion, the product selectivity, product yields and carbon balance were estimated using equations 4.1, 4.2, 4.3, and 4.4 respectively, wherein F is the molar space-time yield (mol s^{-1} g_{cat}^{-1}) and *n* is the number of carbon atoms in a given product (P, n). The product selectivity was evaluated as the ratio of molar flow of carbon in the product to that of the carbon consumed from reactant ethene, and thus it reflects the distribution of carbon from the reactant ethene into the products of varying molar masses. In the case of experiments carried out at low ethene-site times (< 2 h mol s^{-1} g_{cat}^{-1}), the ethene conversions as estimated by equation 4.1 were similar to the error in ethene molar space-times (F_{ethene}, F^0_{ethene}), and thus the ethene conversions were calculated based on the carbon detected in the products and corrected for the carbon balance approximated for the low conversion range, as shown by equation 4.5.

$$Conversion = \frac{F^0_{ethene} - F_{ethene}}{F^0_{ethene}} \tag{4.1}$$

$$Selectivity = \frac{n \times F_{P,n}}{2 \times (F^0_{ethene} - F_{ethene})} \tag{4.2}$$

$$Product\ Yield = \frac{F_{Product}}{F^0_{ethene}} \tag{4.3}$$

$$Carbon\ balance\ (\%) = \frac{\sum nF_{P,n}}{2 \times (F^0_{ethene} - F_{ethene})} \times 100 \tag{4.4}$$

$$Conversion\ (based\ on\ products) = \frac{\sum nF_{P,n}}{2 \times F^0_{ethene}} \times \left(\frac{100}{\%\ Carbon\ balance}\right) \tag{4.5}$$

4.3 Results and Discussion

4.3.1 Active site composition of catalysts

The elemental analysis for Ni-Li-[Al]Beta is reported in Table 2.1 in Chapter 2, which shows a Ni/Al value of 0.26. The diffuse reflectance UV-vis and X-ray absorption spectroscopies indicate Ni to be present in a +2 oxidation state and in a distorted tetrahedral geometry before the reaction and during ethene dimerization (453 K, 0-1 kPa), as discussed in Chapter 2 (Section 2.3.2).

Further, the cationic charge normalized by Al (Table 2.1, Chapter 2) for Ni-Li-[Al]Beta indicates the undetectable residual H^+ sites, consistent with the CO infrared spectra (85 K) (Figure 2.1b, Chapter 2) that does not show a 2174 cm^{-1} feature for H^+ sites. As discussed in Chapter 2, the ethene-assisted activation of Ni^{2+} cations to form $[Ni(II)\text{-}H]^+$ intermediates is proposed to involve the formation of one H^+ site in the proximity of each $[Ni(II)\text{-}H]^+$ species. Also, the ethene-assisted activation of Ni^{2+} cations is rapid at ethene pressures of 0.4 kPa and above as shown in Figure 2.6 (Chapter 2). Thus, considering that each Ni^{2+} cation forms a $[Ni(II)\text{-}H]^+$ species and a proximal H^+ site during activation with ethene at 0.4 kPa, the initial composition of Ni-Li-[Al]Beta sample corresponds to a H^+/Al value of 0.26. Thus, for Ni-Li-[Al]Beta, there exists a 1:1 distribution of Ni and H^+ sites at initial reaction times.

4.3.2 Site origins of oligomerization products

Ethene oligomerization on Ni-Li-[Al]Beta at 453 K, 0.4 kPa ethene and space-times of 1-149 h (mol ethene)$^{-1}$ g_{cat} predominantly formed linear butene isomers (1-butene, cis-2-butene, trans-2-butene) in addition to small amounts (< 5%) of isobutene and propene, while isomers of pentenes and hexenes were also detected at longer space-times (>10 h (mol ethene)$^{-1}$ g_{cat}). Additionally, saturated hydrocarbons such as ethane, n-butane, isobutane and isomers of pentanes, hexanes and heptanes were also observed in small amounts (< 5%) typically at longer space-times. The formation of isobutene indicated the prevalence of alkene isomerization pathways on H^+ sites at all space-times studied. The individual alkane and alkene isomers could not be identified in the case of products heavier than C_4 hydrocarbons and thus the isomers were lumped together as C_5 alkanes, C_5 alkenes, C_6 alkanes, C_6 alkenes, and C_7 alkanes. Isobutane and n-butane were also lumped together as C_4 alkanes.

The transient space-time yields of ethene oligomerization (453 K, 0.4 kPa) products on Ni-Li-[Al]Beta at 1, 4, 10 and 149 h (mol ethene)$^{-1}$ g_{cat} are shown in Figures 4.3-4.6 (Supporting Information). The space-time yields for all products decreased with reaction time, while those for ethane, propene, C_4 alkanes, C_5 alkanes, C_5 alkenes, C_6 alkanes, and C_7 alkanes also exhibited a slight increase during the initial 1 h of reaction time (induction period). To estimate the space-time yields at initial time, deactivation models shown in equations 4.6 and 4.7 (derivations in Section 3.6.2., Chapter 3) were fitted to the decay transients of product space-time yields (Figure 4.3-4.6, Supporting Information) where Y is the space-time yield, k_d is the apparent deactivation constant, n is the apparent deactivation order, and Y_o is the initial space-time yield. The multi-site deactivation model (shown in Equation 4.6) quantitatively described the space-time yields for all products except for C_6 alkenes and C_7 alkanes, which were described by a single-site model (Equation 4.7).

$$\frac{dy}{dt'} = -k_d y^n \ , \qquad Y = \frac{Y_o}{\left[1 + (n-1)k_d {Y_o}^{(n-1)} t\right]^{\left(\frac{1}{n-1}\right)}} \tag{4.6}$$

$$\frac{dy}{dt'} = -k_d y \ , \qquad Y = Y_o e^{-k_d t} \tag{4.7}$$

The apparent deactivation order (n) was determined only for the decay of space-time yields of ethane, propene and C_4 alkenes, as these were detected in all experiments (1, 4, 10, 149 h (mol ethene)$^{-1}$ g_{cat}), so that the values of n shown in Table 4.1 are statistically significant. The space-time yields of ethane exhibited a deactivation order of ~1, suggesting ethane to be formed at an ensemble of sites that undergo single-site deactivation. As discussed before, the site-times yields (per H^+) of C_4 alkenes measured at 453 K on H-[Al]Beta support (Figure 3.1b, Chapter 3) showed an exponential decay, indicating single-site deactivation of H^+ sites at 453 K in the presence of ethene. Taken together, these findings indicate ethane to be formed at the H^+ sites by hydrogenation of ethene [150] with the required H_2 likely being generated *in-situ* [51] via the formation of polyconjugated aliphatic and aromatic compounds, as these compounds were detected on a deactivating Ni-exchanged ZSM-5 catalyst by *in-situ* IR spectroscopy during ethene oligomerization (423-673 K) [141]. Next, propene and C_4 alkenes showed a deactivation order of ~2 (Table 4.1), suggesting they are formed at the same ensemble of sites that undergo a second order deactivation process. As concluded in Chapter 2, the C_4 alkenes are predominantly formed

at Ni sites at 453 K, based on the product selectivities measured on H-[Al]Beta, Ni-H-[Al]Beta and Ni-Li-[Al]Beta (Figure 2.3, Chapter 2). Also, the site-time yields (per Ni) for C_4 alkenes exhibited second-order deactivation (Figure 2.42a, Chapter 2) at 453 K. These results taken together suggest propene to be formed at Ni sites in Ni-Li-[Al]Beta, along with C_4 alkenes. In summary, these findings clarify that ethane and isobutene are formed at H^+ sites, while propene and linear isomers of C_4 alkenes are formed at Ni sites. Next, we analyze the reaction network and identify the reaction pathways (primary, secondary, tertiary, etc.) forming these products using the Delplot technique.

Table 4.1. Apparent deactivation orders for the decay of product space-time yields

Product	**Deactivation order (n)[a]**
Ethane	1.32 ± 0.24
Isobutene	1.31 ± 0.27
Propene	1.91 ± 0.07
Linear C_4 alkenes	1.94 ± 0.22

[a]Determined by using the deactivation model in Equation 4.4

4.3.3 Reaction pathway analysis by Delplot technique

The Delplot technique is a method for quantitative kinetic analysis of reactive systems involving complex pathways [151]. The method determines the 'rank' of each product in the reaction network, such that the first-rank is assigned to primary products, the second-rank to secondary products and so on. This method involves making a plot of yield/(conversion)^(r) vs. conversion, where r is the rank of the Delplot. Accordingly, a first-rank Delplot is a plot of yield/conversion vs. conversion, where the y-intercepts represent the initial rates of formation. Thus, the products exhibiting a non-zero y-intercept have a finite initial formation rate and are primary products, while those with a zero y-intercept have zero initial formation rate and are non-primary products in the reaction network [151]. Also, these characteristics of the first-order Delplot are valid for any reaction order [151]. Further, a second-order Delplot is a plot of yield/$(\text{conversion})^2$ vs. conversion, where the y-intercepts represent the initial formation rate of secondary products. In the case of a second-order Delplot, primary products show a diverging y-

intercept (>> 1), tertiary and higher rank products show a zero y-intercept, while secondary products exhibit a finite intercept with some exceptions in the case of a non-unity reaction order dependence on the primary products. It should be noted that this method does not specify the shape (linear or non-linear) of the curves within the Delplots [151].

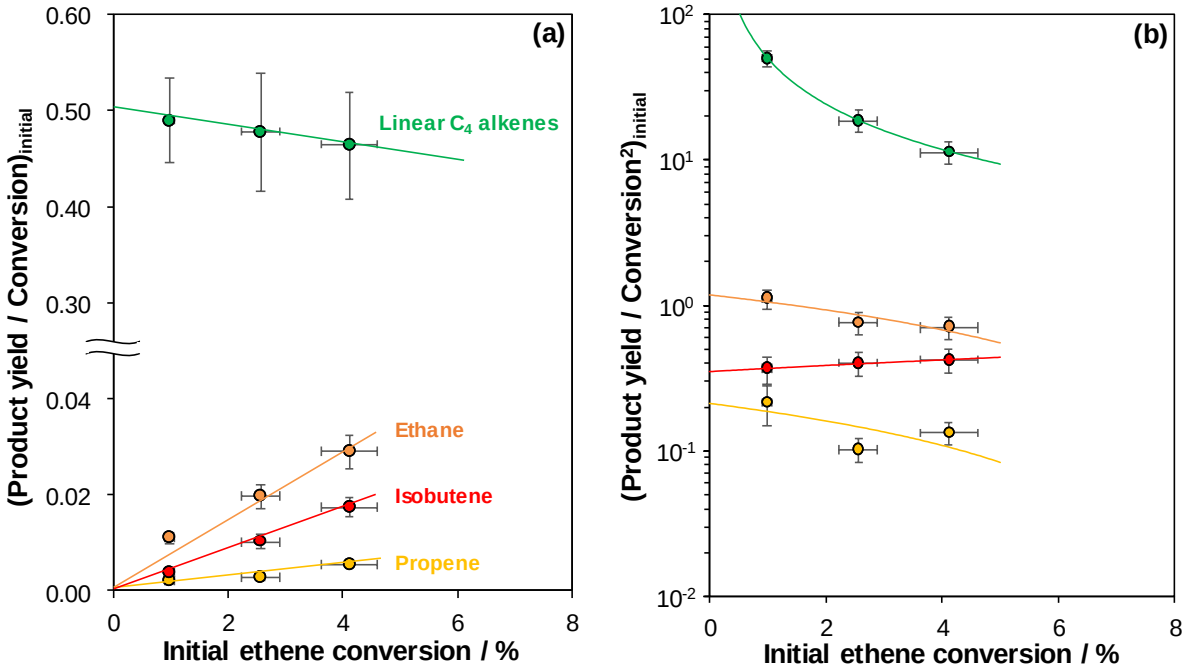

Figure 4.1. (a) First-rank, and (b) semi-log second-rank Delplots for ethene oligomerization network on Ni-Li-[Al]Beta (453 K, 0.4 kPa) involving the products ethane (in orange), propene (in yellow), isobutene (in red) and linear isomers of C_4 alkenes (in green).

Figure 4.1a and b shows the first-rank and second-rank Delplots, respectively for ethene oligomerization products detected on Ni-Li-[Al]Beta (453 K, 0.4 kPa) within differential conversions (< 5%). The differential conversion range was specifically selected to facilitate determination of the y-intercept value, and the estimated product yields (Equation 4.3) were normalized by the carbon balance (Equation 4.4). The first-rank Delplot (Figure 4.1a) showed a finite y-intercept indicative of primary products for linear C_4 alkenes, while a zero y-intercept for ethane, propane, and isobutene indicated these to be non-primary products. Further, the second-rank Delplot (Figure 4.1b) showed finite y-intercepts for ethane, propane, and isobutene, suggesting these to be secondary products. The diverging intercept for linear C_4 alkenes within the second (Figure 4.1b) and third-rank (Figure 4.8, Supporting Information) Delplots and those for

ethane, propane, and isobutene within the third-rank Delplot (Figure 4.8, Supporting Information) further validate identification of the primary and secondary products.

The formation of linear C_4 alkenes as primary products at Ni sites is consistent with the prevalence of the coordination-insertion mechanism at these sites, as discussed in Chapter 2. The formation of isobutene as a secondary product at H^+ sites is consistent with the skeletal isomerization of the linear C_4 alkenes formed as the primary products at the Ni sites, as discussed in Chapters 2 and 3. Since ethane is a secondary product formed at the H^+ sites, its formation is attributed to the hydrogenation of reactant ethene at H^+ sites [150] by H_2 that is generated *in-situ* as a primary product of deep dehydrogenation and aromatization of ethene [51, 141]. The formation of propene as a secondary product at the Ni sites suggests the possibility of cross-metathesis between the reactant ethene and the linear C_4 alkenes that are formed as the primary products. Propene has also been observed for the reaction of ethene (323-723 K) on Ni supported siliceous MCM-41, and has been attributed to the cross-metathesis of ethene and butene [152] at Ni sites, since the propene selectivity increased with increasing temperature above 423 K, along with a concurrent decrease in selectivity towards butene isomers [62]. We further investigate the influence of these reaction pathways on the overall product distribution by evaluating the product selectivities as a function of ethene conversion.

4.3.4 Product selectivities

The product selectivities (Equation 4.2) were determined at initial conversions (Equation 4.1) using the space-time yields extrapolated to initial time (Figure 4.3-4.6, Supporting Information), and the initial conversions were varied by changing the ethene space-times 1-149 h (mol ethene)$^{-1}$ g_{cat} in independent experiments. Figure 4.2 shows the dependence of initial product selectivities on initial ethene conversions for Ni-Li-[Al]Beta at 453 K and 0.4 kPa ethene. These product selectivities reflect a 1:1 composition of Ni and H^+ sites because of the rapid activation of Ni-Li-[Al]Beta at these reaction conditions, as discussed before (Section 4.3.1). At conversions <5%, linear C_4 alkenes were predominantly formed and their selectivity decreased with further increases in conversion, as would be expected for primary products. The selectivities for all other products, which are non-primary, increased with increasing conversion, however, not in a proportion that would commensurate for the decrease in the selectivity to linear C_4 alkenes. This

suggests that at higher conversions (corresponding to higher space-times), linear C_4 alkenes are consumed in non-primary reaction pathways including those that lead to the formation of precursors for catalyst deactivation. This is also supported by the decrease in the carbon balance with increasing ethene conversions (Figure 4.7, Supporting Information), suggesting significant loss of carbon from the feed ethene to the catalyst, which is not detected in the gas phase products. The formation of C_5 alkenes is tentatively ascribed to co-dimerization of ethene and propene, while that of C_4, C_5 and C_6 alkanes is ascribed to the hydrogenation of C_4, C_5 and C_6 alkenes, respectively.

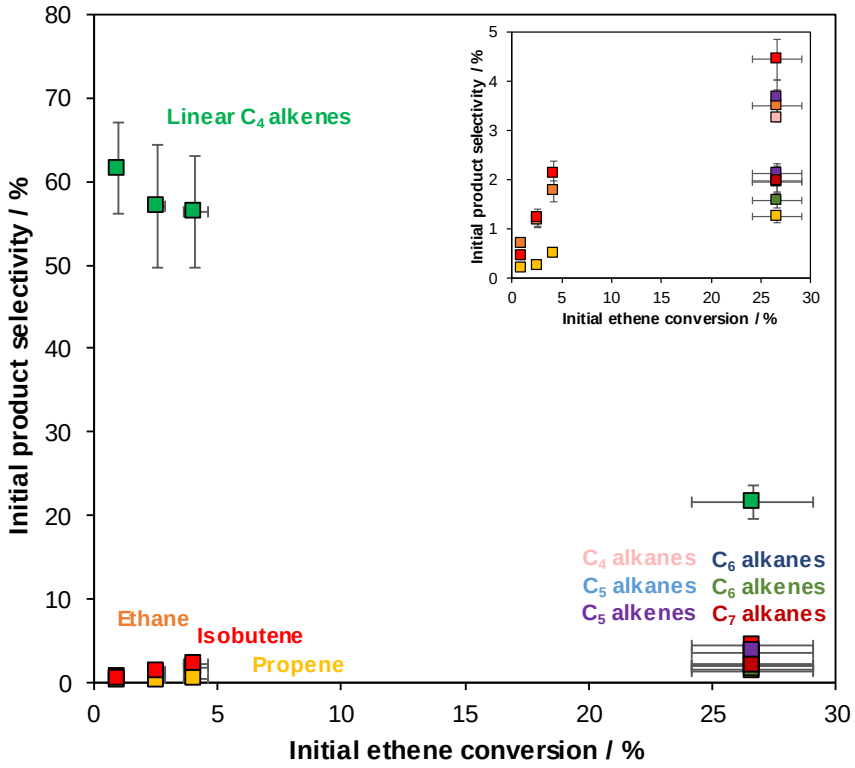

Figure 4.2. Initial product selectivities as a function of initial ethene conversions on Ni-Li-[Al]Beta at 453 K and 0.4 kPa ethene showing the products ethane (in orange), propene (in yellow), C_4 alkanes (in pink), linear C_4 alkenes (in green), isobutene (in red), C_5 alkanes (in light blue), C_5 alkenes (in purple), C_6 alkanes (in dark blue), C_6 alkenes (in dark green), and C_7 alkanes (in dark red). The inset shows magnified results for the products with selectivities less than 5%.

4.4 Conclusions and outlook

The model Ni-Li-[Al]Beta catalyst was used to study the ethene reaction pathways on Ni and H^+ sites. This catalyst generates one H^+ site for every Ni^{2+} cation *in-situ* (453 K, 0.4 kPa ethene) and thus contains a 1:1 composition of Ni and H^+ sites. In order to correlate the reaction

pathways to the known composition of the catalyst, measured product space-time yields were extrapolated to initial time using multi-site and single-site deactivation models. Correlating the measured data using the deactivation models facilitated quantitative determination of the apparent order for the decay of space-time yields with reaction time. The space-time yields (453 K) for ethane and isobutene exhibited a first-order decay similar to that of C_4 alkene site-time yields (453 K, per H^+) on H-[Al]Beta, suggesting their formation pathways to originate at H^+ sites. On the other hand, the space-time yields (453 K) for propene and linear C_4 alkenes exhibited a second-order decay analogous to that of C_4 alkene site-time yields (453 K, per Ni) on Ni-Li-[Al]Beta, suggesting propene to be also formed at Ni sites along with the linear isomers of C_4 alkenes.

The initial product space-time yields estimated for ethane, propene, isobutene and the linear C_4 alkenes within the differential conversion range (<5%) were used to estimate product yields and construct first, second and third-rank Delplots. The first-rank Delplot showed linear C_4 alkenes formed at Ni sites to be primary products. The second-rank Delplot showed ethane and isobutene formed at H^+ sites and propene formed at Ni sites to be secondary products. These findings taken together suggested ethane to be formed at H^+ sites via the hydrogenation of reactant ethene by H_2 generated *in-situ* (453 K), as the primary product. Also, propene formation is proposed to occur at Ni sites via the cross-metathesis of the reactant ethene with linear C_4 alkenes formed as primary products. Finally, these results also corroborate the formation of C_4 linear alkenes as primary products at Ni sites and their secondary skeletal isomerization on H^+ sites to form isobutene, as discussed in Chapters 2 and 3. The mechanistic understanding of the reaction pathways on the Ni^{2+} and H^+ sites will help formulate design principles for Ni-based zeotype catalysts to influence the hydrocarbon chain length and molecular structure of alkene oligomerization products.

The quantitative determination of the apparent order for the decay of product space-time yields, together with Delplot analysis, is a strategy to resolve the complex network of reactions involved in alkene oligomerization. Further efforts are required to extend this strategy for the products heavier than C_4 formed during oligomerization. For Delplot analysis, it is critical that the initial space-time yields of the products are measured within differential conversions (< 5%) and a larger number of experimentally determined data points will allow for linear regression analysis and possible application of the F-test to quantitatively probe the probability of a non-zero intercept

[151]. Moreover, the effect of varying reaction conditions will help determine the interplay between kinetically-controlled isomer selectivity at Ni sites and thermodynamically-governed selectivity at H^+ sites and its consequences for the composition of oligomerization products. Further investigation is also required to assess the influence of varying Ni/H^+ ratio on alkene reaction pathways and thus on the oligomerization product distribution. Furthermore, microkinetic modeling for the oligomerization network coupled with sensitivity analysis of kinetic parameters will allow for identification of variables that have a predominant influence over the oligomerization product composition.

4.5 Supporting Information

4.5.1 Transient product space-time yields

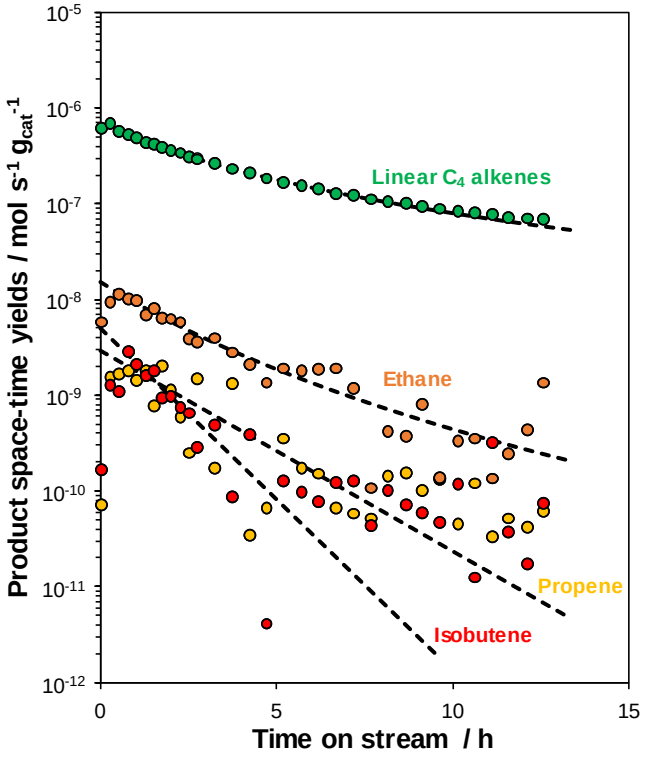

Figure 4.3. Site-time yields measured as a function of reaction time on Ni-Li-[Al]Beta at 453 K, 0.4 kPa ethene and 1 h (mol ethene)$^{-1}$ g_{cat} for the products ethane (in orange), propene (in yellow), linear C_4 alkenes (in green) and isobutene (in red). The black dashed lines show the product site-time yields predicted by the fitted deactivation models.

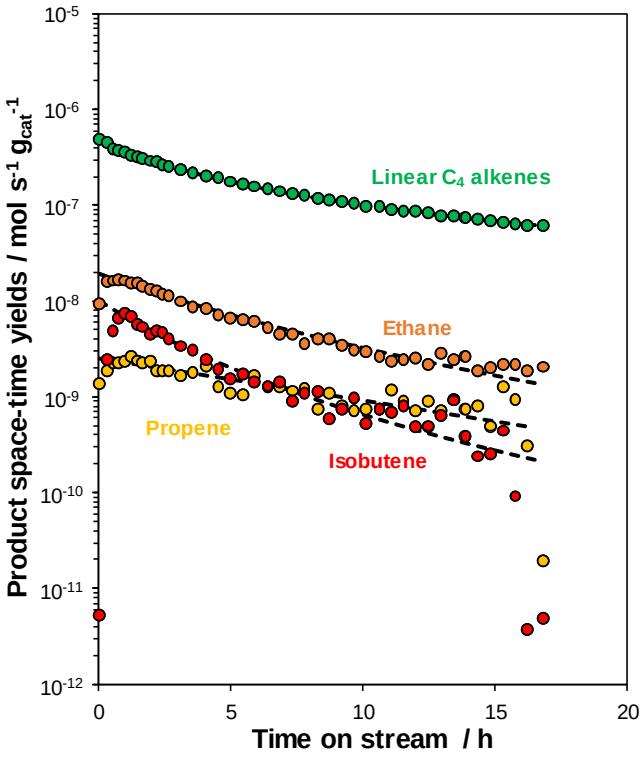

Figure 4.4. Site-time yields measured as a function of reaction time on Ni-Li-[Al]Beta at 453 K, 0.4 kPa ethene and 4 h (mol ethene)$^{-1}$ g_{cat} for the products ethane (in orange), propene (in yellow), linear C_4 alkenes (in green) and isobutene (in red). The black dashed lines show the product site-time yields predicted by the fitted deactivation models.

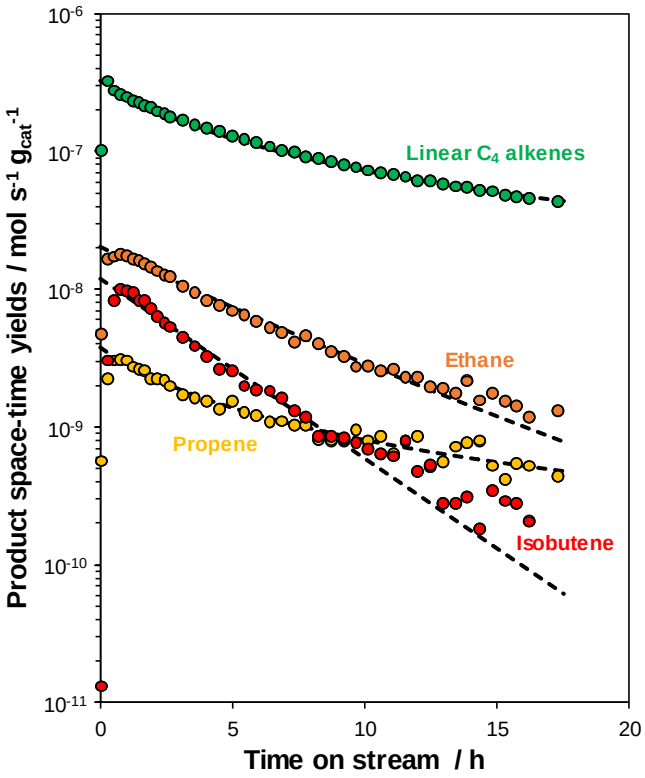

Figure 4.5. Site-time yields measured as a function of reaction time on Ni-Li-[Al]Beta at 453 K, 0.4 kPa ethene and 10 h (mol ethene)$^{-1}$ g_{cat} for the products ethane (in orange), propene (in yellow), linear C_4 alkenes (in green) and isobutene (in red). The black dashed lines show the product site-time yields predicted by the fitted deactivation models.

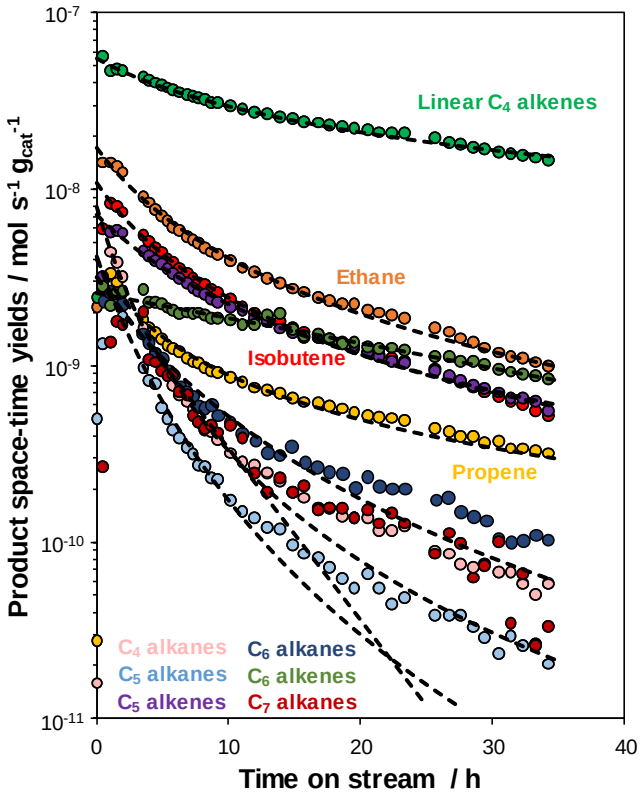

Figure 4.6. Site-time yields measured as a function of reaction time on Ni-Li-[Al]Beta at 453 K, 0.4 kPa ethene and 149 h (mol ethene)$^{-1}$ g_{cat} for the products ethane (in orange), propene (in yellow), C_4 alkanes (in pink), linear C_4 alkenes (in green), isobutene (in red), C_5 alkanes (in light blue), C_5 alkenes (in purple), C_6 alkanes (in dark blue), C_6 alkenes (in dark green), and C_7 alkanes (in dark red). The black dashed lines show the product site-time yields predicted by the fitted deactivation models.

4.5.2 Carbon balance

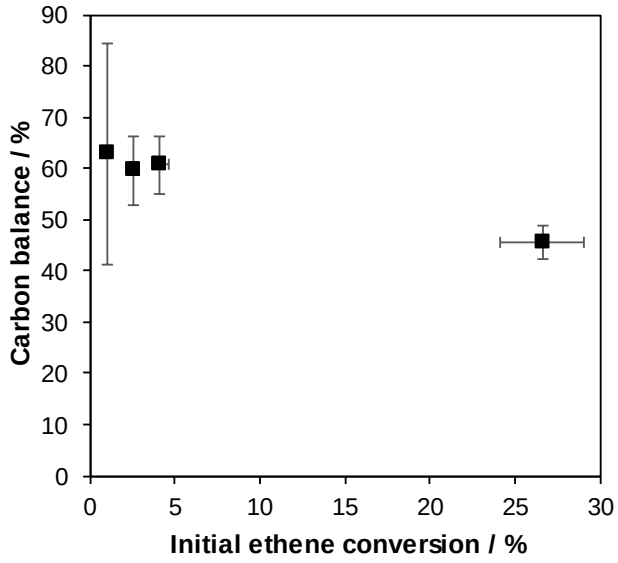

Figure 4.7. Carbon balance as a function of ethene conversion, evaluated for the product space-time yields extrapolated to the initial reaction time.

4.5.3 Third-rank Delplot

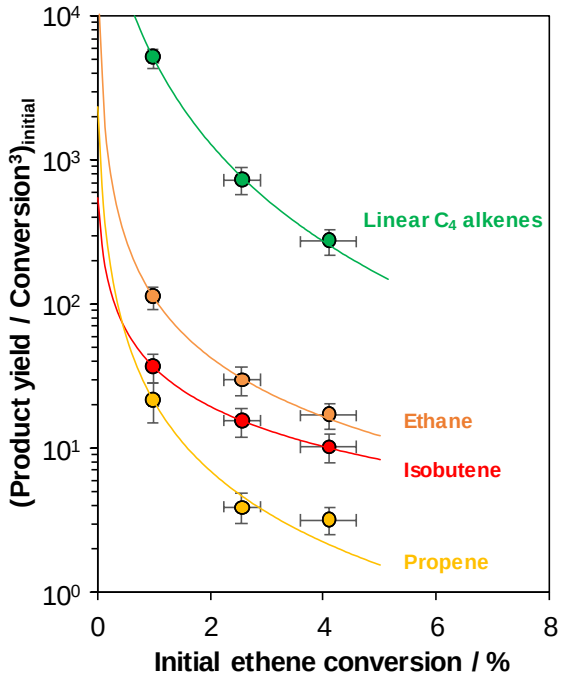

Figure 4.8. Third-rank Delplot for ethene oligomerization network on Ni-Li-[Al]Beta (453 K, 0.4 kPa) involving the products ethane (in orange), propene (in yellow), isobutene (in red) and linear isomers of C_4 alkenes (in green).

A. CHARACTERIZATION OF METAL HYDRIDES BY HYDROGEN-DEUTERIUM ISOTOPIC EXCHANGE TECHNIQUES

A.1 Introduction

Metal hydride intermediates of transition and main group metals catalyze alkane dehydrogenation, alkane metathesis, alkene hydrogenation, alkene metathesis, and alkene oligomerization reactions, which are important chemical pathways to upgrade natural gas liquids (ethane, propane and butane) into intermediate chemicals and transportation fuels. Zn-hydrides [123], Co-hydrides [124] and Ni-hydrides [122] on silica supports, and Ga-hydrides [153, 154] on zeolitic supports are reported to catalyze propane dehydrogenation and propene hydrogenation. Ta-hydrides on silica and W-hydrides on alumina are reported to mediate metathesis of alkanes [155] while Ni-hydrides on zeolites are reported to catalyze dimerization of alkenes [145].

Metal hydrides of main group (Ga) and early-transition metals (W, Ta, Zr) have been detected and verified using IR and reversible H/D exchange experiments, however, the detection of late-transition metal (Fe, Co, Ni) hydrides is challenging given the low intensity of the IR bands for M-H stretching vibrations caused by their low dipole moment [156]. ^{1}H NMR has also been used to detect metal hydrides in homogeneous and heterogeneous catalysts [156], however, it is challenging to employ this technique for heterogeneous systems of late-transition metals wherein hydrides are formed *in-situ* at high temperatures and are often reversibly decomposed under *ex-situ* conditions. In addition to the detection of metal hydrides, their quantification on heterogeneous catalytic materials is required to normalize turnover rate data, which is fundamental to understanding the mechanistic details of the relevant chemical reactions. To the best of my knowledge, there are no reported techniques that allow direct quantification of metal-hydrides of transition metals such as Ni, Co and Zn, and main group elements such as Ga on heterogeneous supports.

Here, methods are studied to quantify metal-hydrides formed on heterogeneous supports via H_2-D_2 isotopic exchange under conditions that do not cause reduction of metal species to their metallic states. Isothermal treatment of Ni-exchanged zeolites and silica-supported single-site Zn, Co and Ga materials with H_2, followed by isothermal titration with D_2 evolves gaseous HD in an amount equivalent to that obtained by isothermal treatment with D_2 followed by H_2, reflecting

reversible H/D exchange. The quantification of gaseous HD formed by these sequential H_2-D_2 exchanges provides an estimate for the number of metal sites that can be transformed into catalytically relevant hydride intermediates.

A.2 Experimental Methods

A.2.1 Material synthesis

The Ni-exchanged Beta zeolites, Ni-H-[Al]Beta and Ni-Li-[Al]Beta were synthesized using the methods described in Chapter 2 (Section 2.2.1).

The single-site Zn/SiO_2 and Co/SiO_2 materials were synthesized by the strong electrostatic adsorption technique [157] using a commercial silica support (Davisil Grade 636, 35-60 mesh, surface area 480 m^2/g). For both materials, 25 g of silica was suspended in 200 mL of deionized water and the pH was adjusted to 11 using ammonium hydroxide solution. For the synthesis of Zn/SiO_2, 5 g of $Zn(NO_3)_2.6H_2O$ (Sigma Aldrich, 99.99%) was dissolved in 50 mL of deionized water with pH adjusted to 11 using ammonium hydroxide and continued addition of ammonium hydroxide until a clear, colorless solution was obtained. This Zn solution was then rapidly added to the silica suspended in basic solution, stirred for at least 10 min and then allowed to settle. The settled solids were recovered by vacuum filtration, rinsed with deionized water multiple times, dried overnight in an oven maintained at 398 K, and treated in flowing dry air at 573 K (0.075 K s^{-1}) for 3 h. The Co/SiO_2 sample was prepared following an identical procedure, wherein 5 g of $Co(NO_3)_2.6H_2O$ (Sigma Aldrich, 99.99%) was dissolved in 50 mL of deionized water, the pH was adjusted to 11 using ammonium hydroxide, and partial precipitation of unknown cobalt species was removed by filtration. This Co solution was then rapidly added to the silica suspended in basic solution stirred for at least 10 min and then allowed to settle. The settled solids were recovered, washed, dried and treated in air using the same procedure as that for Zn/SiO_2.

The Ga/SiO_2 sample was prepared by following a procedure reported by Getsoian et al. [158]. An aqueous solution was prepared by dissolving 3 g of gallium nitrate and 3 g of citric acid in 15 ml of deionized water, and the solution was stirred until all solids were dissolved. The pH of the solution was adjusted to 11 using concentrated ammonium hydroxide solution which was used

to impregnate 20 g of commercial silica. The wet solid was then dried overnight at 383 K and then treated in air at 823 K (0.075 K s^{-1}) for 3 h.

A.2.2 Material characterization

The elemental compositions of catalysts were determined by atomic absorption spectroscopy (AAS) using a Perkin Elmer AAnalyst 300 Atomic Absorption Spectrometer. Samples were prepared by digesting approximately 0.02 g of catalyst in 2.5 g of hydrofluoric acid (48 wt. %, Sigma-Aldrich) overnight, followed by dilution with 50 g of ultrapure water (18.2 MΩ). The solutions were further diluted for Ni, Li and Zn measurements in order to obtain the absorbances in linear calibration range. Calibration standard solutions were prepared for each metal by diluting 1000 ppm AAS standards (Sigma-Aldrich, TraceCERT, +/- 4 ppm), and the instrument was calibrated for each element prior to the measurements. Absorbances were measured in an oxidizing acetylene/air flame for Li, Ni, Co and Zn at wavelengths 670.8, 232.0, 240.7 and 213.9 nm respectively, while in a reducing acetylene/nitrous oxide flame for Si, Al and Ga at wavelengths of 251.6, 308.2 and 294.4 nm, respectively. The Si/Al ratios for zeolite Beta were determined using the Al weight fraction together with the unit cell formula.

The number of H^+ sites on H-[Al]Beta and the residual H^+ sites on Ni-H-[Al]Beta were quantified by NH_3 temperature-programmed desorption (TPD) as described in Chapter 2 (Section 2.6.2.4).

IR spectra were collected in transmission mode using a Nicolet 4700 spectrometer on samples pressed into self-supporting wafers (0.015-0.02 g cm^{-2}) sealed within a custom-built quartz IR cell with CaF_2 windows. Details regarding the experimental setup and cell design can be found elsewhere [80, 81]. At the start of each experiment, the sample wafers were treated in flowing dry air (6.67 cm^3 s^{-1} $(g_{cat})^{-1}$) purified by an FTIR purge gas generator (Parker Balston, <1 ppm CO_2, 200 K H_2O dew point) to 723 K (0.083 K s^{-1}) for 1 h, and then held under dynamic vacuum at 723 K for 1 h. The sample was then cooled to 453 K under dynamic vacuum and exposed to a stream of flowing H_2 (99.999%, Matheson Tri-Gas, 18.5 cm^3 g^{-1} s^{-1}) or to a stream of 5% H_2/95% He mixture (99.999%, Matheson Tri-Gas, 18.5 cm^3 g^{-1} s^{-1}). IR spectra were collected by averaging 64 scans at 2 cm^{-1} resolution, taken relative to an empty cell background reference

(static vacuum at 303 K), in the range 4000 to 650 cm^{-1}. The IR spectra were baseline-corrected and normalized to the combination and overtone modes of zeolite Si-O-Si vibrations (1750-2100 cm^{-1}) for zeolite Beta samples.

Time resolved X-ray absorption spectroscopy (XAS) experiments were performed at the Advanced Photon Source of Argonne National Laboratory using the insertion device beamline (10-ID-B) of the Materials Research Collaborative Access Team (MRCAT) at Sector 10. The incident X-ray beam was measured in an ion chamber filled with N_2 while the transmitted beam was measured in an ion chamber filled with 20% He in N_2 to obtain roughly 70% absorption of the beam after the sample. The energy calibration was done using a Ni metal foil (8333 eV) and for every measurement, a spectrum for Ni metal foil reference was simultaneously collected using a third detector. The beam size was set to 200 x 200 μm and the data was collected in a quick scan mode within the energy range 8730 to 9133 eV. The data was normalized with a 1st-order polynomial subtraction of the pre-edge and 3rd-order polynomial subtraction of the post edge backgrounds using WinXAS 3.2 software. The data was Fourier transformed over the range 2.7-10.5 $Å^{-1}$ and fit using Ni-O scattering pairs, which was simulated using Feff 6 software. Total absorption (μx) due only to the sample and carbon tube reactor was around 1.2-1.3, with a step height ($\Delta\mu x$) of around 0.3-0.9.

In-situ XAS experiments were performed in a custom built fixed-bed reactor consisting of a low X-ray absorbing vitreous carbon tube reactor (10 mm x 4 mm x 200 mm OD x ID x L), heated by an aluminum heater block with 25 mm x 2 mm wide slits on the sides to allow the X-ray beam to pass through the block and the sample. A detailed discussion on the design of the reactor setup and its use to collect *in-situ/operando* XAS can be found in previous publications [159, 160]. The samples were sieved to a size of 180-250 μm, and approximately 8-12 mg of sample was loaded on top of a quartz wool plug supported by a 1/8-inch stainless steel tube inserted from the bottom of the carbon tube. Another quartz wool plug was placed on top of the sample with a thermocouple inserted into it from the top end of the carbon tube. After loading the reactor tube, the sample was flushed with He (139-278 $cm^3\ g^{-1}\ s^{-1}$, 99.999%, Airgas) and XAS scans were collected to align the sample with the beam path. The sample was dehydrated using 1% O_2/99% He mixture (139-278 $cm^3\ g^{-1}\ s^{-1}$, 99.999%, Airgas) at 673 K (non-uniform ramp rate) for 0.5 h before cooling down to the temperature at which H_2 was to be contacted (e.g. 453 K). Then the

sample was purged with He and XAS scan was collected for the sample in the dehydrated state. Next, the sample was contacted with a 3.5% H_2/96.5% He mixture (42-83 $cm^3\ g^{-1}\ s^{-1}$, 99.999%, Airgas) and XAS scans were collected as a function of time until no changes were observed in the collected spectra.

A.2.3 Sequential H_2-D_2 exchange

The H_2-D_2 sequential exchange experiments were carried out in a Micromeritics Autochem II 2920 Chemisorption analyzer connected in-line to a Residual Gas Analyzer (Model 200, Stanford Research Systems). The zeolite-based samples were pelleted and sieved to a particle size between 180-250 μm, while the silica-based samples were used without sieving. Approximately 0.050-0.100 g of each sample were loaded into a quartz U-tube reactor by supporting between two quartz wool plugs. The zeolite-based and silica-based samples were treated in flowing dry air (8.3-16.7 $cm^3\ s^{-1}\ g_{cat}^{-1}$, 99.999% UHP, Matheson Tri-Gas) at 803 K (0.0167 K s^{-1}) for 5 h, and 773 K for 1 h, respectively, followed by cooling to the desired H_2-D_2 exchange temperature and subsequent flushing with Ar for 0.5 h. For each experiment, the signals for m/z of 2 (H_2), 3 (HD), 4 (D_2), 20 (Ar^{2+}) and 40 (Ar^{+}) were recorded following the treatment. The sample was first held in a flowing 5% H_2/95% Ar mixture (4.2-5.5 $cm^3\ s^{-1}\ g_{cat}^{-1}$) for 1-2 h at a given isothermal temperature, and then the flow was switched to a 5% D_2/95% Ar mixture (4.2-5.5 $cm^3\ s^{-1}\ g_{cat}^{-1}$), and again held for 1-2 h or until the HD signal dropped to the baseline value. This was followed by a reverse switch to flow the 5% H_2/95% Ar mixture for 1-2 h, or until the HD signal reached its baseline value. This procedure of sequentially switching the flow between H_2 and D_2 was repeated at least 4 times, and the HD response after every switch was quantified using a response factor relative to an Ar internal standard (m/z = 20), obtained by equilibrating H_2/D_2 mixtures (in Ar) of different composition over a 1% Pt/Al_2O_3 sample at 673 K. The 1% Pt/Al_2O_3 sample was prepared by using a procedure reported elsewhere [82] and was treated in flowing 5% H_2/95% Ar (5.5 $cm^3\ s^{-1}\ g_{cat}^{-1}$, 99.999% UHP, Matheson Tri-Gas) at 673 K (0.0167 K s^{-1}) for 1 h before equilibrating the isotopic mixtures of H_2/D_2 at 673 K.

For each sample, the moles of HD formed were identical during the switch in the flow from H_2 to D_2 and during the reverse switch from D_2 to H_2, which were averaged to determine the moles of HD formed at a given temperature. The amount of HD generated was corrected for background

contributions by performing identical H_2-D_2 switching experiments at each temperature in a blank reactor.

A.3 Results and Discussion

A.3.1 Ni-hydride quantification for Ni-exchanged Beta zeolites

The moles of HD quantified by H_2-D_2 exchange at 453 K on the Ni-exchanged samples, Ni-Li-[Al]Beta, Ni-H-[Al]Beta and on their support materials, Li-[Al]Beta and H-[Al]Beta are shown in Table A.1. The Ni-Li-[Al]Beta sample showed approximately one HD formed per Ni^{2+} cation, and Ni cations remained in the 2+ oxidation state under these conditions of H_2-D_2 exchange as indicated by *in-situ* XANES (Figure A.3 and Table A.4). This result is consistent with H/D exchange at $[Ni(II)\text{-}H]^+$ or $[Ni(II)\text{-}D]^+$ intermediates, initially formed by heterolytic dissociative adsorption of H_2 at exchanged Ni^{2+} cations along with generation of a H^+ site at a proximal framework Al center, as shown in Scheme A.1. The Li-[Al]Beta and H-[Al]Beta supports showed negligible HD formation (per mol Al, Table A.1), relative to Ni-Li-[Al]Beta, indicating that residual Li^+ cations and H^+ sites present on the sample or formed *in situ* upon dissociative H_2 adsorption have lower H/D exchange rates and do not contribute to measured HD formation at 453 K. IR studies [161, 162] on Zn-exchanged MFI zeolites have shown analogous heterolytic dissociation of dihydrogen on a Zn^{2+} cation to form a $[Zn(II)\text{-}H]^+$ intermediate (1936 cm^{-1}) and a Brønsted acid site (3612 cm^{-1}).

Table A.1. HD quantification on zeolite Beta samples at 453 K.

Sample	Ni/Al	H^+/Al[a]	Li^+/Al	Cationic charge / Al[b]	Mol HD / mol Al	Mol HD / mol Ni
Ni-Li-[Al]Beta	0.26	n.d.	0.50	1.02	0.24	0.94
Li-[Al]Beta	0	n.d.	1.01	1.01	0.02	-
Ni-H-[Al]Beta	0.20	0.25	0	0.65	0.61	3.06
H-[Al]Beta	0	0.65	0	0.65	0.01	-

[a]measured by NH_3 TPD
[b]estimated by assuming a 1:1 stoichiometry for H^+ and Li^+ and a 2:1 stoichiometry for Ni^{2+}
n.d.: not determined

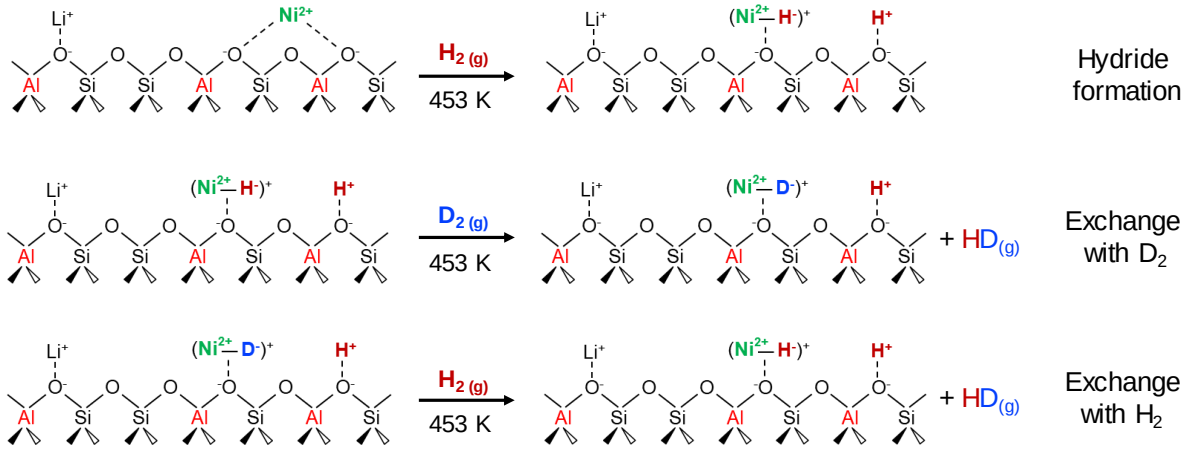

Scheme A.1. Formation of [Ni(II)-H]$^+$ from exchanged Ni^{2+} cations followed by sequential H/D exchange with gaseous D_2 and H_2

The Ni-H-[Al]Beta sample showed higher amounts of HD formed (per Ni) than the Ni-Li-[Al]Beta sample, and the moles of HD formed (per Al) corresponded to the total cationic charge (Table A.1) unlike the case for Ni-Li-[Al]Beta. This finding would be consistent with H/D exchange at [Ni(II)-H]$^+$ intermediates along with H/D exchange at the proximal H^+ sites generated by dissociative adsorption of H_2 and at the residual H^+ sites initially present on Ni-H-[Al]Beta. H/D exchange at all H^+ sites on Ni-H-[Al]Beta may be attributed to the spillover of H_2/D_2 from Ni^{2+} sites, because the H-[Al]Beta support showed negligible HD formation at 453 K. The presence of metals such as Ga and Zn has been reported to lower the onset temperature for measurable H/D exchange at H^+ sites on zeolite Beta [153]. The onset temperatures for H/D exchange at H^+ sites estimated by extrapolating the Arrhenius plots [153] for H-Beta, Ga-impregnated H-Beta and Zn-impregnated H-Beta are 455 K, 417 K and 370 K, respectively. Accordingly, the presence of Ni^{2+} cations may enhance the rate of H/D exchange (at 453 K) on residual H^+ sites of Ni-H-[Al]Beta by spillover mechanisms. On the other hand, the amount of HD formed (per Al) on Ni-Li-[Al]Beta is similar to the Ni/Al ratio and would be expected to be twice the Ni/Al ratio in the case of H/D exchange at the proximal H^+ sites generated by dissociative H_2 adsorption and at the [Ni(II)-H]$^+$ sites themselves. It is currently unclear why H_2/D_2 spillover would be observed for Ni-H-[Al]Beta and not in the case of Ni-Li-[Al]Beta and is tentatively attributed to the differences in electronic properties of Ni^{2+} cations in the presence of H^+ and Li^+ cations [163]. Further investigations are

required, including repeat measurements at different space times and H_2-D_2 exchange experiments on a suite of Ni-exchanged Beta zeolites with varying Ni/H^+ ratio.

A.3.2 Attempts to detect Ni-hydride on Ni-exchanged Beta zeolites

The $[Ni(II)\text{-}H]^+$ intermediate is a terminal Ni-hydride, and such terminal Ni-hydrides are reported to be detected in the range 1690-2000 cm^{-1} for various homogeneous Ni-complexes [164]. In order to obtain direct evidence for $[Ni(II)\text{-}H]^+$ intermediates, *in-situ* (453 K, 1 bar H_2) transmission IR experiments were performed on the Ni-Li-[Al]Beta sample and the Li-[Al]Beta support, and the spectra are shown in Figure A.1. In the presence of H_2, both the Ni-Li-[Al]Beta sample and the Li-[Al]Beta support showed features for adsorbed water in the 1635 cm^{-1} peak for the deformation vibration [165], and the broad features at 3703 and 3570 cm^{-1} for decoupled OH stretching vibrations [166], suggesting water contamination into the IR cell perhaps from the H_2 source. No other IR features were observed for Ni-Li-[Al]Beta that could be attributed to the formation of $[Ni(II)\text{-}H]^+$ intermediates. It is possible that the intensity of the IR features for the terminal hydrides, $[Ni(II)\text{-}H]^+$, could be below detection [164] because of the low dipole moment of the Ni-H stretching vibration [156]. Further infrared studies are required using the DRIFTS mode which would exhibit relatively lower intensity for the zeolite framework vibrations and use of a cold-trap (ethanol + dry-ice or liquid N_2) is recommended to condense moisture from H_2 source gas.

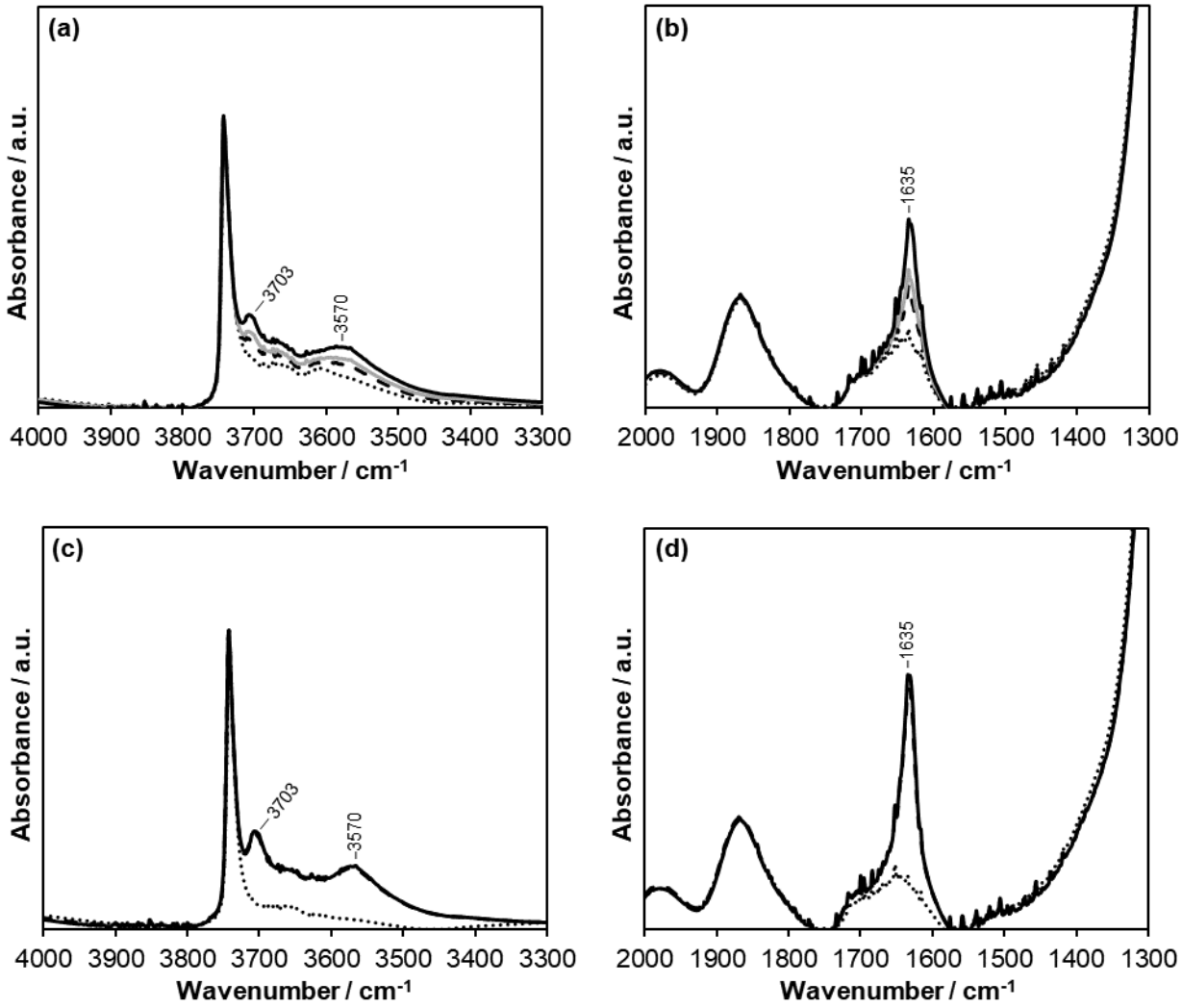

Figure A.1. Infrared spectra for (a) Ni-Li-Beta in OH region, (b) Ni-Li-[Al]Beta in CH region, (c) Li-[Al]Beta in OH region, and (d) Li-[Al]Beta in CH region; collected at 453 K under vacuum (dotted line), Helium (dashed line), 5 kPa H_2 in Argon (solid grey line), and 1 bar H_2 (solid black line)

Further, the structural geometry of the $[Ni^{2+}(II)\text{-}H]^+$ site was probed by X-ray absorption spectroscopy, and Figure A.2 shows the EXAFS region while Table 2 shows the calculated parameters. The Ni-Li-[Al]Beta sample shows identical Ni-O coordination number and Ni-O bond distance when it was dehydrated and when it was held under H_2 at 453 K, wherein $[Ni(II)\text{-}H]^+$ intermediates are formed. This indicates that isolated Ni^{2+} cations and $[Ni(II)\text{-}H]^+$ intermediates have similar geometry. Ni-H bonds could not be probed by EXAFS because H is a light scattering atom.

Table A.2. EXAFS fitting results for Ni-Li-[Al]Beta sample

Sample, condition	Coordination number (Ni-O)	Distance (Å)
Ni-Li-[Al]Beta, dehydrated (453 K, Helium)	4.3	2.00
Ni-Li-[Al]Beta, under H_2 (453 K, 3.5 kPa H_2)	4.3	2.01
Bulk NiO, dehydrated (ambient, Helium)	6.0	2.07

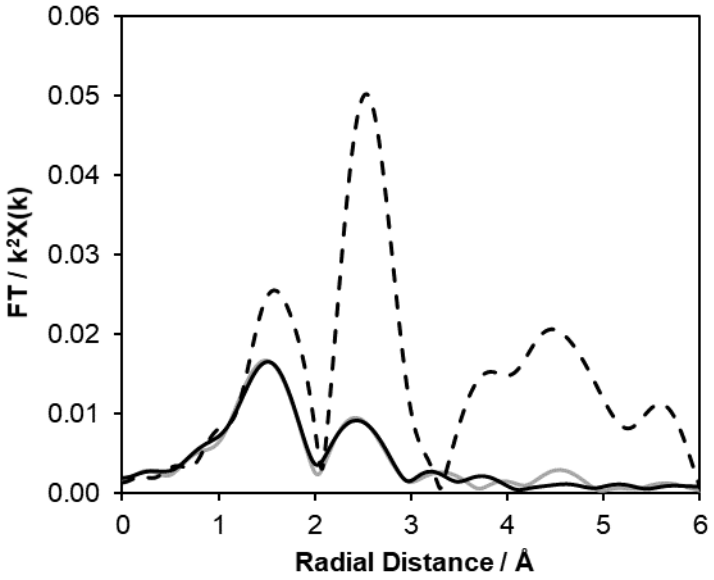

Figure A.2. EXAFS for Ni-Li-[Al]Beta sample after dehydration (453 K, Helium) (grey solid line), in presence of hydrogen (453 K, 3.5 kPa H_2) (black solid line), and for bulk NiO (reference material) (dashed line)

A.3.3 Metal-hydride quantification for single-site silica-supported catalysts

Isothermal H_2-D_2 exchange experiments were carried out on single-site silica-supported catalysts containing Zn^{2+}, Co^{2+} and Ga^{3+} cations at 473, 523 and 723 K. The amount of HD formed was normalized per metal atom, and the results are shown in Table A.3. Under these conditions of H_2-D_2 exchange, Zn^{2+}, Co^{2+} and Ga^{3+} cations are respectively present in 2+, 2+ and 3+ oxidation states because H_2 treatments up to 773 K do not cause their reduction to metallic states as probed by X-ray absorption spectroscopy [123, 167, 168]. Thus, the formation of HD on these samples

represents H/D exchange at cationic metal hydrides/deuterides formed by dissociated adsorption of H_2 or D_2, requiring rupture of metal-support (M-O) covalent bonds [123, 124, 158]. In the case of all three samples, Zn/SiO_2, Co/SiO_2 and Ga/SiO_2, the amount of HD quantified increased with temperature, suggesting that the formation of metal-hydrides is favored at higher temperatures.

Table A.3. HD quantification for metal (M) single-site silica-supported samples

Sample	M loading (wt. %)	H_2-D_2 exchange temperature (K)	Mol HD / mol M
Zn/SiO_2	4.0	523	0.34 ± 0.02
		723	0.70 ± 0.09
Co/SiO_2	3.1	523	0.26 ± 0.02
		723	0.54 ± 0.03
Ga/SiO_2	2.6	473	0.29 ± 0.02
		723	2.53 ± 0.07

Overall, the results presented here demonstrate the utility of sequential H_2-D_2 titration to quantify the fraction of metal sites that can form catalytically relevant metal-hydride intermediates. It should be noted that these H_2-D_2 experiments were carried out using 5 kPa H_2 and D_2, and thus the amount of HD quantified may reflect only a fraction of the metal-hydride sites under the exchange conditions studied. Further work is needed to probe the effects of H_2 coverage and to accurately assess the contributions from the support silanol and Brønsted acid sites due to possible H_2/D_2 spillover from the metal cations.

A.4 Acknowledgments

I acknowledge Arunima Saxena for her assistance with H_2-D_2 isotopic exchange experiments and for helpful intellectual discussions. I would also like to acknowledge Nicole Libretto for her help conducting the X-ray absorption experiments and for analyzing the XANES and EXAFS data. I am also thankful to Casey Jones and Trevor Lardinois for their efforts and sleepless time spent at the beamline for X-ray absorption experiments.

A.5 Supporting Information

Figure A.4. shows the Ni K-edge XANES spectra for Ni-Li-[Al]Beta sample collected after dehydration and during the *in-situ* treatment with H_2 (3.5 kPa) at 453 K, and Table A.3. lists the measured pre-edge and edge energy values along with the Ni oxidation states.

Table A.4. XANES results for Ni-Li-[Al]Beta sample

Sample, condition	Pre-edge energy (keV)	Edge energy (keV)	Ni oxidation state
Ni-Li-[Al]Beta, dehydrated (453 K, Helium)	8.3333	8.3386	+2
Ni-Li-[Al]Beta, under H_2 (453 K, 3.5 kPa H_2)	8.3333	8.3391	+2
Bulk NiO, dehydrated (ambient, Helium)	8.3332	8.3410	+2

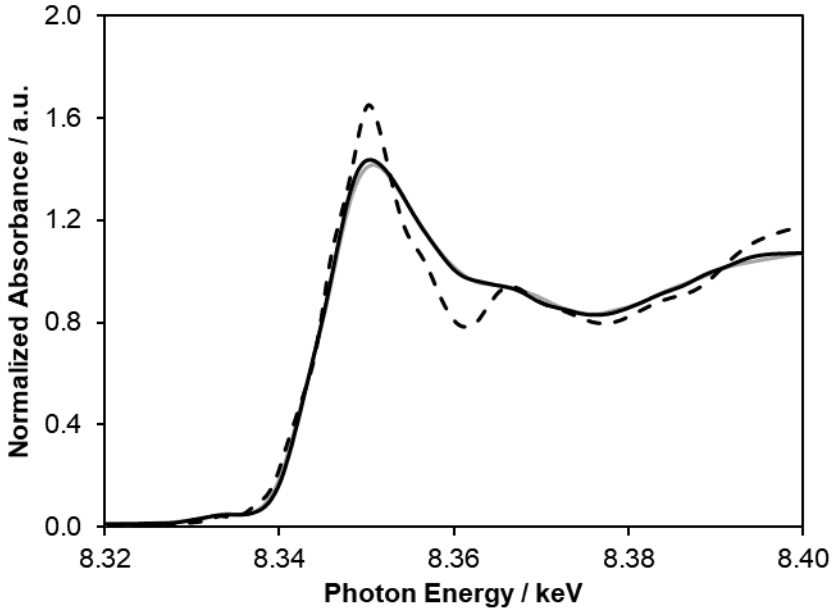

Figure A.3. Ni K-edge XANES spectra for Ni-Li-[Al]Beta sample after dehydration (453 K, Helium) (grey solid line), in presence of hydrogen (453 K, 3.5 kPa H2) (black solid line), and for bulk NiO (reference material) (dashed line)

REFERENCES

[1] C.T. O'Connor, M. Kojima, Alkene oligomerization, Catal. Today, 6 (1990) 329-349.

[2] J. Skupinska, Oligomerization of alpha olefins to higher olefins, Chem. Rev., 91 (1991) 613-648.

[3] D.S. McGuinness, Olefin Oligomerization via Metallacycles: Dimerization, Trimerization, Tetramerization, and Beyond, Chem. Rev., 111 (2011) 2321-2341.

[4] B.L. Small, Discovery and Development of Pyridine-bis(imine) and Related Catalysts for Olefin Polymerization and Oligomerization, Acc. Chem. Res., 48 (2015) 2599-2611.

[5] C.P. Nicholas, Applications of light olefin oligomerization to the production of fuels and chemicals, App. Catal., A, 543 (2017) 82-97.

[6] F. Speiser, P. Braunstein, L. Saussine, Catalytic ethylene dimerization and oligomerization: recent developments with nickel complexes containing P,N-chelating ligands., Acc. Chem. Res., 38 (2005) 784-793.

[7] A. Kermagoret, P. Braunstein, Mono- and Dinuclear Nickel Complexes with Phosphino-, Phosphinito-, and Phosphonitopyridine Ligands: Synthesis, Structures, and Catalytic Oligomerization of Ethylene, Organometallics, 27 (2008) 88-99.

[8] S. Forget, H. Olivier-Bourbigou, D. Delcroix, Homogeneous and Heterogeneous Nickel-Catalyzed Olefin Oligomerization: Experimental Investigation for a Common Mechanistic Proposition and Catalyst Optimization, ChemCatChem, 9 (2017) 2408-2417.

[9] W. Keim, Nickel: An Element with Wide Application in Industrial Homogeneous Catalysis, Angew. Chem. Int. Ed. Engl., 29 (1990) 235-244.

[10] P. Braunstein, F. Naud, Hemilability of hybrid ligands and the coordination chemistry of oxazoline-based systems, Angew. Chem. Int. Ed., 40 (2001) 680-699.

[11] U. Rosenthal, B.H. Müller, N. Peulecke, S. Peitz, A. Wöhl, W. Müller, H. Olivier-Bourbigou, L. Magna, P.W.N.M. van Leeuwen, M.J.L. Tschan, M. Hapke, N. Weding, K. Kral, Oligomerization, Cyclooligomerization, Dimerization, in: Applied Homogeneous Catalysis with Organometallic Compounds, Wiley-VCH Verlag GmbH & Co. KGaA, 2017, pp. 307-410.

[12] Y. Chauvin, J. Gaillard, D.V. Quang, J. Andrews, IFP Dimersol process for dimerization of C3 and C4 olefinic cuts, Chemistry & Industry, (1974) 375-378.

[13] D. Vogt, Other Biphasic Concepts: Sections 7.1–7.2, in: Aqueous-Phase Organometallic Catalysis, Wiley-VCH Verlag GmbH & Co. KGaA, 2005, pp. 637-654.

[14] A. Forestière, H. Olivier-Bourbigou, L. Saussine, Oligomerization of Monoolefins by Homogeneous Catalysts, Oil & Gas Science and Technology - Rev. IFP, 64 (2009) 649-667.

[15] W. Keim, F.H. Kowaldt, R. Goddard, C. Krüger, Novel Coordination of (Benzoylmethylene)triphenylphosphorane in a Nickel Oligomerization Catalyst, Angew. Chem. Int. Ed. Engl., 17 (1978) 466-467.

[16] W. Keim, R.P. Schulz, Chelate control in the nickel-complex catalysed homogeneous oligomerization of ethylene, J. Mol. Catal., 92 (1994) 21-33.

[17] W. Keim, A. Behr, B. Gruber, B. Hoffmann, F.H. Kowaldt, U. Kuerschner, B. Limbaecker, F.P. Sistig, Reactions of chelate ylides with nickel (0) complexes, Organometallics, 5 (1986) 2356-2359.

[18] R.H. Grubbs, A. Miyashita, Metallacyclopentanes as catalysts for the linear and cyclodimerization of olefins, J. Am. Chem. Soc., 100 (1978) 7416-7418.

[19] R.H. Grubbs, A. Miyashita, The metallacyclopentane–olefin interchange reaction, J. Chem. Soc., Chem. Commun., (1977) 864-865.

[20] S.A. Svejda, M. Brookhart, Ethylene Oligomerization and Propylene Dimerization Using Cationic (α-Diimine)nickel(II) Catalysts, Organometallics, 18 (1999) 65-74.

[21] R.L. Espinoza, C.J. Korf, C.P. Nicolaides, R. Snel, Catalytic Oligomerization of Ethene over Nickel-Exchanged Amorphous Silica-Alumina: Effect of the Reaction Conditions and Modelling of the Reaction, App. Catal., 29 (1987) 175-184.

[22] J. Heveling, C.P. Nicolaides, M.S. Scurrell, Catalysts and conditions for the highly efficient, selective and stable heterogeneous oligomerisation of ethylene, App. Catal., A, 173 (1998) 1-9.

[23] R.L. Espinoza, C.P. Nicolaides, C.J. Korf, R. Snel, Catalytic oligomerization of ethene over nickel-exchanged amorphous silica-alumina; Effect of the nickel concentration, App. Catal., 31 (1987) 259-266.

[24] J. Heveling, A. van der Beek, M. de Pender, Oligomerization of ethene over nickel-exchanged zeolite y into a diesel-range product, App. Catal., 42 (1988) 325-336.

[25] A.K. Ghosh, L. Kevan, Electron spin resonance studies of ethylene dimerization catalyzed by nickel species on Y zeolites, J. Phys. Chem., 94 (1990) 3117-3121.

[26] L. Bonneviot, D. Olivier, M. Che, Dimerization of olefins with nickel-surface complexes in X-type zeolite or on silica, J. Mol. Catal., 21 (1983) 415-430.

[27] M. Lallemand, O.A. Rusu, E. Dumitriu, A. Finiels, F. Fajula, V. Hulea, NiMCM-36 and NiMCM-22 catalysts for the ethylene oligomerization: Effect of zeolite texture and nickel cations/acid sites ratio, App. Catal., A, 338 (2008) 37-43.

[28] M. Lallemand, A. Finiels, F. Fajula, V. Hulea, Catalytic oligomerization of ethylene over Ni-containing dealuminated Y zeolites, App. Catal., A, 301 (2006) 196-201.

[29] F.T.T. Ng, D.C. Creaser, Ethylene Dimerization: Kinetics and Selectivity for 1-Butene, in: J.S. Kevin, C.S. Emerson (Eds.) Stud. Surf. Sci. Catal., Elsevier, 1992, pp. 123-131.

[30] I.V. Elev, The Role of Ni^{+} Ions in the activity of NiCaY Zeolite catalysts for Ethylene Dimerization, J. Catal., 89 (1984) 470-477.

[31] A. Martínez, M.A. Arribas, P. Concepción, S. Moussa, New bifunctional Ni–H-Beta catalysts for the heterogeneous oligomerization of ethylene, App. Catal., A, 467 (2013) 509-518.

[32] A.N. Mlinar, G.B. Baur, G.G. Bong, A.B. Getsoian, A.T. Bell, Propene oligomerization over Ni-exchanged Na-X zeolites, J. Catal., 296 (2012) 156-164.

[33] R. Henry, M. Komurcu, Y. Ganjkhanlou, R.Y. Brogaard, L. Lu, K.J. Jens, G. Berlier, U. Olsbye, Ethene oligomerization on nickel microporous and mesoporous-supported catalysts: Investigation of the active sites, Catal. Today, 299 (2018) 154-163.

[34] M. Hartmann, A. Pöppl, L. Kevan, Ethylene Dimerization and Butene Isomerization in Nickel-Containing MCM-41 and AlMCM-41 Mesoporous Molecular Sieves: An Electron Spin Resonance and Gas Chromatography Study, J. Phys. Chem., 100 (1996) 9906-9910.

[35] M. Lallemand, A. Finiels, F. Fajula, V. Hulea, Ethylene oligomerization over Ni-containing mesostructured catalysts with MCM-41, MCM-48 and SBA-15 topologies, Stud. Surf. Sci. Catal., 170 (2007) 1863-1869.

[36] V. Hulea, F. Fajula, Ni-exchanged AlMCM-41 - An efficient bifunctional catalyst for ethylene oligomerization, J. Catal., 225 (2004) 213-222.

[37] M. Lallemand, O.A. Rusu, E. Dumitriu, A. Finiels, F. Fajula, V. Hulea, Ni-MCM-36 and Ni-MCM-22 catalysts for the ethylene oligomerization, in: P.M. Antoine Gédéon, B. Florence (Eds.) Stud. Surf. Sci. Catal., Elsevier, 2008, pp. 1139-1142.

[38] R.D. Andrei, M.I. Popa, F. Fajula, V. Hulea, Heterogeneous oligomerization of ethylene over highly active and stable Ni-AlSBA-15 mesoporous catalysts, J. Catal., 323 (2015) 76-84.

[39] S. Lin, L. Shi, H. Zhang, N. Zhang, X. Yi, A. Zheng, X. Li, Tuning the pore structure of plug-containing Al-SBA-15 by post-treatment and its selectivity for C16 olefin in ethylene oligomerization, Microporous Mesoporous Mater., 184 (2014) 151-161.

[40] A.N. Mlinar, S. Shylesh, O.C. Ho, A.T. Bell, Propene oligomerization using Alkali metal- and nickel-exchanged mesoporous aluminosilicate catalysts, ACS Catal., 4 (2014) 337-343.

[41] I. Agirrezabal-Telleria, E. Iglesia, Stabilization of active, selective, and regenerable Ni-based dimerization catalysts by condensation of ethene withinordered mesopores, J. Catal., 352 (2017) 505-514.

[42] Q. Zhang, I.G. Dalla Lana, An analysis of mass transfer and kinetics during ethylene oligomerization over nickel/sulfated alumina catalyst in a slurry reactor, Chem. Eng. Sci., 52 (1997) 4187-4195.

[43] Q. Zhang, M. Kantcheva, I.G. Dalla Lana, Oligomerization of Ethylene in a Slurry Reactor Using a Nickel/Sulfated Alumina Catalyst, Ind. Eng. Chem. Res., 36 (1997) 3433-3438.

[44] A.A. Davydov, M. Kantcheva, M.L. Chepotko, FTIR Spectroscopic Study on Nickel(II)-Exchanged Sulfated Alumina: Nature of the Active Sites in the Catalytic Oligomerization of Ethene., Catal. Lett., 83 (2002) 97-108.

[45] C. O'Connor, M. Kojima, Alkene oligomerization, Catal. Today, 6 (1990) 329-349.

[46] A. Finiels, F. Fajula, V. Hulea, Nickel-based solid catalysts for ethylene oligomerization - a review, Catal. Sci. Technol., 4 (2014) 2412-2426.

[47] E.D. Metzger, C.K. Brozek, R.J. Comito, M. Dincă, Selective Dimerization of Ethylene to 1-Butene with a Porous Catalyst, ACS Central Science, 2 (2016) 148-153.

[48] J. Krzystek, J.-H. Park, M.W. Meisel, M.A. Hitchman, H. Stratemeier, L.-C. Brunel, J. Telser, EPR spectra from "EPR-Silent" species: High-frequency and high-field EPR spectroscopy of pseudotetrahedral complexes of nickel (II), Inorganic chemistry, 41 (2002) 4478-4487.

[49] M. Lallemand, A. Finiels, F. Fajula, V. Hulea, Nature of the Active Sites in Ethylene Oligomerization Catalyzed by Ni-Containing Molecular Sieves: Chemical and IR Spectral Investigation, J. Phys. Chem. C, 113 (2009) 20360-20364.

[50] M. Tanaka, A. Itadani, Y. Kuroda, M. Iwamoto, Effect of Pore Size and Nickel Content of Ni-MCM-41 on Catalytic Activity for Ethene Dimerization and Local Structures of Nickel Ions, J. Phys. Chem. C, 116 (2012) 5664-5672.

[51] S. Moussa, P. Concepción, M.A. Arribas, A. Martínez, Nature of Active Nickel Sites and Initiation Mechanism for Ethylene Oligomerization on Heterogeneous Ni-beta Catalysts, ACS Catal., 8 (2018) 3903-3912.

[52] F.T.T. Ng, D.C. Creaser, Ethylene dimerization over modified nickel exchanged Y-zeolite, App. Catal., A, 119 (1994) 327-339.

[53] S.A. Svejda, L.K. Johnson, M. Brookhart, Low-Temperature Spectroscopic Observation of Chain Growth and Migratory Insertion Barriers in (α-Diimine)Ni(II) Olefin Polymerization Catalysts, J. Am. Chem. Soc., 121 (1999) 10634-10635.

[54] J.A. Suttil, D.S. McGuinness, Mechanism of Ethylene Dimerization Catalyzed by Ti(OR′)4/AlR3, Organometallics, 31 (2012) 7004-7010.

[55] R. Robinson, D.S. McGuinness, B.F. Yates, The Mechanism of Ethylene Dimerization with the Ti(OR′)4/AlR3 Catalytic System: DFT Studies Comparing Metallacycle and Cossee Proposals, ACS Catal., 3 (2013) 3006-3015.

[56] K. Toch, J.W. Thybaut, G.B. Marin, Ethene oligomerization on Ni-SiO2-Al2O3: Experimental investigation and Single-Event MicroKinetic modeling, App. Catal., A, 489 (2015) 292-304.

[57] F.X. Cai, C. Lepetit, M. Kermarec, D. Olivier, Dimerization of ethylene into 1-butene over supported tailor-made nickel catalysts, J. Mol. Catal., 43 (1987) 93-116.

[58] E.D. Metzger, R.J. Comito, C.H. Hendon, M. Dincă, Mechanism of Single-Site Molecule-Like Catalytic Ethylene Dimerization in Ni-MFU-4l, J. Am. Chem. Soc., 139 (2017) 757-762.

[59] R.Y. Brogaard, U. Olsbye, Ethene Oligomerization in Ni-Containing Zeolites: Theoretical Discrimination of Reaction Mechanisms, ACS Catal., 6 (2016) 1205-1214.

[60] S.D. Ittel, L.K. Johnson, M. Brookhart, Late-Metal Catalysts for Ethylene Homo- and Copolymerization, Chem. Rev., 100 (2000) 1169-1204.

[61] M.L. Sarazen, E. Doskocil, E. Iglesia, Effects of Void Environment and Acid Strength on Alkene Oligomerization Selectivity, ACS Catal., 6 (2016) 7059-7070.

[62] L. Alvarado Perea, T. Wolff, P. Veit, L. Hilfert, F.T. Edelmann, C. Hamel, A. Seidel-Morgenstern, Alumino-mesostructured Ni catalysts for the direct conversion of ethene to propene, J. Catal., 305 (2013) 154-168.

[63] F.E. Shephard, J.J. Rooney, C. Kemball, The polymerization of propylene on silica-alumina, J. Catal., 1 (1962) 379-388.

[64] H. Pines, The chemistry of catalytic hydrocarbon conversions, Academic Press, New York, 1981.

[65] M. Lallemand, A. Finiels, F. Fajula, V. Hulea, Continuous stirred tank reactor for ethylene oligomerization catalyzed by NiMCM-41, Chem. Eng. J., 172 (2011) 1078-1082.

[66] E.E. Stangland, Shale Gas Implications for C_2-C_3 Olefin Production: Incumbent and Future Technology, Annu Rev Chem Biomol Eng, 9 (2018) 341-364.

[67] P.C.A. Bruijnincx, B.M. Weckhuysen, Shale Gas Revolution: An Opportunity for the Production of Biobased Chemicals?, Angew. Chem. Int. Ed., 52 (2013) 11980-11987.

[68] P. Cossee, On the reaction mechanism of the ethylene polymerization with heterogeneous ziegler-natta catalysts, Tetrahedron Lett., 1 (1960) 12-16.

[69] P. Cossee, Ziegler-Natta catalysis I. Mechanism of polymerization of α-olefins with Ziegler-Natta catalysts, J. Catal., 3 (1964) 80-88.

[70] E.J. Arlman, P. Cossee, Ziegler-Natta catalysis III. Stereospecific polymerization of propene with the catalyst system $TiCl_3$-$AlEt_3$, J. Catal., 3 (1964) 99-104.

[71] J. Skupinska, Oligomerization of α-Olefins to Higher Oligomers, Chem. Rev., 91 (1991) 613-648.

[72] G.J.P. Britovsek, V.C. Gibson, D.F. Wass, The Search for New-Generation Olefin Polymerization Catalysts: Life beyond Metallocenes, Angew. Chem. Int. Ed., 38 (1999) 428-447.

[73] M.A. Escobar, O.S. Trofymchuk, B.E. Rodriguez, C. Lopez-Lira, R. Tapia, C. Daniliuc, H. Berke, F.M. Nachtigall, L.S. Santos, R.S. Rojas, Lewis Acid Enhanced Ethene Dimerization and Alkene Isomerization—ESI-MS Identification of the Catalytically Active Pyridyldimethoxybenzimidazole Nickel(II) Hydride Species, ACS Catal., 5 (2015) 7338-7342.

[74] P. Kuhn, D. Semeril, D. Matt, M.J. Chetcuti, P. Lutz, Structure-reactivity relationships in SHOP-type complexes: tunable catalysts for the oligomerisation and polymerisation of ethylene, Dalton Transactions, (2007) 515-528.

[75] M. Hartmann, A. Pöppl, L. Kevan, Ethylene dimerization in nickel containing MCM-41 and AlMCM-41 studied by electron spin resonance and gas chromatography, Stud. Surf. Sci. Catal., Volume 101 (1996) 801-809.

[76] K. Toch, J.W. Thybaut, M.A. Arribas, A. Martínez, G.B. Marin, Steering linear 1-alkene, propene or gasoline yields in ethene oligomerization via the interplay between nickel and acid sites, Chem. Eng. Sci., 173 (2017) 49-59.

[77] T. Takewaki, L.W. Beck, M.E. Davis, Zincosilicate CIT-6: A Precursor to a Family of *BEA-Type Molecular Sieves, J. Phys. Chem. B, 103 (1999) 2674-2679.

[78] M. Yonemitsu, Y. Tanaka, M. Iwamoto, Metal Ion-Planted MCM-41. 1. Planting of Manganese(II) Ion into MCM-41 by a Newly Developed Template-Ion Exchange Method, Chem. Mater., 9 (1997) 2679-2681.

[79] K. Ikeda, Y. Kawamura, T. Yamamoto, M. Iwamoto, Effectiveness of the template-ion exchange method for appearance of catalytic activity of Ni–MCM-41 for the ethene to propene reaction, Catal. Commun., 9 (2008) 106-110.

[80] V.J. Cybulskis, J.W. Harris, Y. Zvinevich, F.H. Ribeiro, R. Gounder, A transmission infrared cell design for temperature-controlled adsorption and reactivity studies on heterogeneous catalysts, Rev. Sci. Instrum., 87 (2016) 103-101.

[81] J.W. Harris, M.J. Cordon, J.R. Di Iorio, J.C. Vega-Vila, F.H. Ribeiro, R. Gounder, Titration and quantification of open and closed Lewis acid sites in Sn-Beta zeolites that catalyze glucose isomerization, J. Catal., 335 (2016) 141-154.

[82] J.H. Pazmiño, M. Shekhar, W. Damion Williams, M. Cem Akatay, J.T. Miller, W. Nicholas Delgass, F.H. Ribeiro, Metallic Pt as active sites for the water–gas shift reaction on alkali-promoted supported catalysts, J. Catal., 286 (2012) 279-286.

[83] G.H. Kuehl, H.K.C. Timken, Acid sites in zeolite Beta: effects of ammonium exchange and steaming, Microporous Mesoporous Mater., 35 (2000) 521-532.

[84] E. Bourgeat-Lami, P. Massiani, F. Di Renzo, P. Espiau, F. Fajula, T. Des Courières, Study of the state of aluminium in zeolite-β, App. Catal., 72 (1991) 139-152.

[85] G.L. Woolery, G.H. Kuehl, H.C. Timken, A.W. Chester, J.C. Vartuli, On the nature of framework Brønsted and Lewis acid sites in ZSM-5, Zeolites, 19 (1997) 288-296.

[86] J. Dědeček, Z. Sobalík, B. Wichterlová, Siting and Distribution of Framework Aluminium Atoms in Silicon-Rich Zeolites and Impact on Catalysis, Cat. Rev., 54 (2012) 135-223.

[87] A. Abraham, S.-H. Lee, C.-H. Shin, S. Bong Hong, R. Prins, J.A. van Bokhoven, Influence of framework silicon to aluminium ratio on aluminium coordination and distribution in zeolite Beta investigated by ^{27}Al MAS and ^{27}Al MQ MAS NMR, Phys. Chem. Chem. Phys., 6 (2004) 3031-3036.

[88] M. Orazov, M.E. Davis, Catalysis by framework zinc in silica-based molecular sieves, Chem. Sci., 7 (2016) 2264-2274.

[89] S. Mintova, V. Valtchev, T. Onfroy, C. Marichal, H. Knözinger, T. Bein, Variation of the Si/Al ratio in nanosized zeolite Beta crystals, Microporous Mesoporous Mater., 90 (2006) 237-245.

[90] K. Hadjiivanov, A. Penkova, M.A. Centeno, FTIR indication of CO interaction with O^{2-} ions: A new adsorption form in the gap between chemi- and physisorbed CO, Catal. Commun., 8 (2007) 1715-1718.

[91] M. Maache, A. Janin, J.C. Lavalley, J.F. Joly, E. Benazzi, Acidity of zeolites Beta dealuminated by acid leaching: An FTi.r. study using different probe molecules (pyridine, carbon monoxide), Zeolites, 13 (1993) 419-426.

[92] A. Zecchina, D. Scarano, S. Bordiga, G. Spoto, C. Lamberti, Surface structures of oxides and halides and their relationships to catalytic properties, in: Advances in Catalysis, Academic Press, New York, 2001, pp. 265.

[93] M. Mihaylov, K. Hadjiivanov, H. Knözinger, Formation of $Ni(CO)_4$ during the Interaction between CO and Silica-Supported Nickel Catalyst: an FTIR Spectroscopic Study, Catal. Lett., 76 (2001) 59-63.

[94] H.A. Aleksandrov, V.R. Zdravkova, M.Y. Mihaylov, P.S. Petkov, G.N. Vayssilov, K.I. Hadjiivanov, Precise Identification of the Infrared Bands of the Polycarbonyl Complexes on Ni–MOR Zeolite by $^{12}C^{16}O$–$^{13}C^{18}O$ Coadsorption and Computational Modeling, J. Phys. Chem. C, 116 (2012) 22823-22831.

[95] A. Penkova, S. Dzwigaj, R. Kefirov, K. Hadjiivanov, M. Che, Effect of the preparation method on the state of nickel ions in BEA zeolites. a study by fourier transform infrared spectroscopy of adsorbed CO and NO, temperature-programmed reduction, and X-ray diffraction, J. Phys. Chem. C, 111 (2007) 8623-8631.

[96] M. Mihaylov, K. Hadjiivanov, FTIR Study of CO and NO Adsorption and Coadsorption on Ni-ZSM-5 and Ni/SiO2, Langmuir, 18 (2002) 4376-4383.

[97] K. Hadjiivanov, H. Knözinger, M. Mihaylov, FTIR study of CO adsorption on Ni-ZSM-5, J. Phys. Chem. B, 106 (2002) 2618-2624.

[98] Y. Ganjkhanlou, E. Groppo, S. Bordiga, M.A. Volkova, G. Berlier, Incorporation of Ni into HZSM-5 zeolites: Effects of zeolite morphology and incorporation procedure, Microporous Mesoporous Mater., 229 (2016) 76-82.

[99] H. Knozinger, S. Huber, IR spectroscopy of small and weakly interacting molecular probes for acidic and basic zeolites, J. Chem. Soc., Faraday Trans., 94 (1998) 2047-2059.

[100] K. Góra-Marek, A. Glanowska, J. Datka, Quantitative IR studies of the concentration of different nickel sites in NiZSM-5 zeolites, Microporous Mesoporous Mater., 158 (2012) 162-169.

[101] E. Stolper, Water in silicate glasses: An infrared spectroscopic study, Contrib. Mineral. Petrol., 81 (1982) 1-17.

[102] D. Li, A. Nishijima, D.E. Morris, Zeolite-Supported Ni and Mo Catalysts for Hydrotreatments: I. Catalytic Activity and Spectroscopy, J. Catal., 182 (1999) 339-348.

[103] C.J. Ballhausen, Introduction to ligand field theory, McGraw-Hill, New York, 1962.

[104] C.K. Jørgensen, Comparative Crystal Field Studies. 2. Nickel (II) and Copper (II) Complexes With Poyldentate Ligands and the Behaviour of the Residual places For Co-ordination, Acta Chem. Scand., 10 (1956) 887-910.

[105] C.K. Jørgensen, L.H. Smith, G. Hanshoff, H. Prydz, Comparative Crystal Field Studies of some Ligands and the Lowest Singlet State of Paramagnetic Nickel(II) Complexes, Acta Chem. Scand., 9 (1955) 1362-1377.

[106] A.B.P. Lever, Inorganic electronic spectroscopy, 2nd ed., Elsevier, Amsterdam, 1984.

[107] R. Baran, A. Śrębowata, I.I. Kamińska, D. Łomot, S. Dzwigaj, Catalytic activity of HAlBEA and Ni_xHAlBEA zeolites in hydrogen-assisted dehydrochlorination of 1,2-dichloroethane into vinyl chloride monomer, Microporous Mesoporous Mater., 180 (2013) 209-218.

[108] A. Śrębowata, R. Baran, D. Łomot, D. Lisovytskiy, T. Onfroy, S. Dzwigaj, Remarkable effect of postsynthesis preparation procedures on catalytic properties of Ni-loaded BEA zeolites in hydrodechlorination of 1,2-dichloroethane, Appl. Catal., B, 147 (2014) 208-220.

[109] M.A. Zanjanchi, A. Ebrahimian, A complementary spectroscopic study on the nickel-containing zeolite Y modified by solid-state dealumination, Mater. Chem. Phys., 110 (2008) 228-233.

[110] C. Lepetit, M. Che, Discussion on the coordination of Ni^{2+} ions to lattice oxygens in calcined faujasite-type zeolites followed by diffuse reflectance spectroscopy, J. Phys. Chem., 100 (1996) 3137-3143.

[111] D. Olivier, L. Bonneviot, F. Cai, M. Che, P. Gihr, M. Kermarec, C. Lepetitpourcelot, B. Morin, Preparation, Characterization and Reactivity of complex Ni(I) ions supported on Silica, Bull. Soc. Chim. Fr., (1985) 370-380.

[112] K. Klier, M. Rálek, Spectra of zynthetic zeolites containing transition metal ions—II. Ni^{2+} ions in type a linde molecular sieves, J. Phys. Chem. Solids, 29 (1968) 951-957.

[113] R.J. Comito, E.D. Metzger, Z. Wu, G. Zhang, C.H. Hendon, J.T. Miller, M. Dincă, Selective Dimerization of Propylene with Ni-MFU-4 l, Organometallics, 36 (2017) 1681-1683.

[114] K.P. Bryliakov, A.A. Antonov, Recent progress of transition metal based catalysts for the selective dimerization of ethylene, J. Organomet. Chem., 867 (2018) 55-61.

[115] M. Sanati, C. Hornell, S.G. Jaras, The oligomerization of alkenes by heterogeneous catalysts, in: Catalysis, The Royal Society of Chemistry, Cambridge, 1999, pp. 236.

[116] J. Datka, Transformations of butenes on dehydroxylated Y zeolites studied by infrared spectroscopy, J. Chem. Soc., Faraday Trans. 1, 77 (1981) 2633-2643.

[117] L.M. Kustov, V.Y. Borovkov, V.B. Kazansky, Study of Ethylene Oligomerization on Bronsted and lewis Acidic Sites of Zeolites Using Diffuse Reflectance IR Spectroscopy, Stud. Surf. Sci. Catal., 18 (1984) 241-247.

[118] S.J. Miller, Olefin Oligomerization Over High Silica Zeolites, Stud. Surf. Sci. Catal., 38 (1988) 187-197.

[119] R.J. Quann, L.A. Green, S.A. Tabak, F.J. Krambeck, Chemistry of olefin oligomerization over ZSM-5 catalyst, Ind. Eng. Chem. Res., 27 (1988) 565-570.

[120] A. Feller, J.-O. Barth, A. Guzman, I. Zuazo, J.A. Lercher, Deactivation pathways in zeolite-catalyzed isobutane/butene alkylation, J. Catal., 220 (2003) 192-206.

[121] M.A. Deimund, J. Labinger, M.E. Davis, Nickel-Exchanged Zincosilicate Catalysts for the Oligomerization of Propylene, ACS Catal., 4 (2014) 4189-4195.

[122] G. Zhang, C. Yang, J.T. Miller, Tetrahedral Nickel(II) Phosphosilicate Single-Site Selective Propane Dehydrogenation Catalyst, ChemCatChem, 10 (2018) 961-964.

[123] N.M. Schweitzer, B. Hu, U. Das, H. Kim, J. Greeley, L.A. Curtiss, P.C. Stair, J.T. Miller, A.S. Hock, Propylene Hydrogenation and Propane Dehydrogenation by a Single-Site Zn^{2+} on Silica Catalyst, ACS Catal., 4 (2014) 1091-1098.

[124] D.P. Estes, G. Siddiqi, F. Allouche, K.V. Kovtunov, O.V. Safonova, A.L. Trigub, I.V. Koptyug, C. Copéret, C–H Activation on Co,O Sites: Isolated Surface Sites versus Molecular Analogs, J. Am. Chem. Soc., 138 (2016) 14987-14997.

[125] R. Bermejo-Deval, M. Orazov, R. Gounder, S.-J. Hwang, M.E. Davis, Active Sites in Sn-Beta for Glucose Isomerization to Fructose and Epimerization to Mannose, ACS Catal., 4 (2014) 2288-2297.

[126] S. Mintova, N. Barrier, Database of Zeolite Structures, in, 2018.

[127] S.A. Bates, W.N. Delgass, F.H. Ribeiro, J.T. Miller, R. Gounder, Methods for NH_3 titration of Brønsted acid sites in Cu-zeolites that catalyze the selective catalytic reduction of NO_x with NH_3, J. Catal., 312 (2014) 26-36.

[128] J.R. Di Iorio, S.A. Bates, A.A. Verma, W.N. Delgass, F.H. Ribeiro, J.T. Miller, R. Gounder, The Dynamic Nature of Brønsted Acid Sites in Cu–Zeolites During NO_x Selective Catalytic Reduction: Quantification by Gas-Phase Ammonia Titration, Top. Catal., 58 (2015) 424-434.

[129] T. Takewaki, L. Beck, M. Davis, Synthesis of CIT-6, a zincosilicate with the *BEA topology, Top. Catal., 9 (1999) 35-42.

[130] M. Dusselier, P. Van Wouwe, A. Dewaele, P.A. Jacobs, B.F. Sels, Shape-selective zeolite catalysis for bioplastics production, Science, 349 (2015) 78-80.

[131] B. Bonelli, E. Garrone, B. Fubini, B. Onida, M. Rodríguez Delgado, C. Otero Areán, Two distinguishable lithium sites in the zeolite Li-ZSM-5 as revealed by adsorption of CO: an infrared spectroscopic and thermodynamic characterisation, Phys. Chem. Chem. Phys., 5 (2003) 2900-2905.

[132] Coblentz Society Inc, Carbon Monoxide, Evaluated Infrared Reference Spectra, in: NIST Chemistry WebBook, NIST Standard Reference Database Number 69, Eds. P.J. Linstrom and W.G. Mallard, National Institute of Standards and Technology, Gaithersburg MD, 20899.

[133] E. Parry, An infrared study of pyridine adsorbed on acidic solids. Characterization of surface acidity, J. Catal., 2 (1963) 371-379.

[134] P. Pichat, M. Mathieu, B. Imelik, Etude par Spectrometrie Infrarouge de l'Adsorption de la Pyridine, Bull. Soc. Chim. Fr, 8 (1969) 2611.

[135] G. Connell, J.A. Dumesic, Acidic properties of binary oxide catalysts, J. Catal., 101 (1986) 103-113.

[136] J.W. Ward, The nature of active sites on zeolites, J. Catal., 10 (1968) 34-46.

[137] M.R. Basila, T.R. Kantner, K.H. Rhee, The Nature of the Acidic Sites on a Silica-Alumina. Characterization by Infrared Spectroscopic Studies of Trimethylamine and Pyridine Chemisorption[1], J. Phys. Chem., 68 (1964) 3197-3207.

[138] K. Iyoki, K. Itabashi, W. Chaikittisilp, S.P. Elangovan, T. Wakihara, S. Kohara, T. Okubo, Broadening the applicable scope of seed-directed, organic structure-directing agent-free synthesis of zeolite to zincosilicate components: A case of VET-type zincosilicate zeolites, Chem. Mater., 26 (2014) 1957-1966.

[139] P.E. Liley, G.H. Thomson, D.G. Friend, E. Buck, Perry's Chemical Engineers' Handbook, 7th ed., McGraw-Hill Professional, New York, 1997.

[140] C. Costa, J.M. Lopes, F. Lemos, F. Ramôa Ribeiro, Activity–acidity relationship in zeolite Y: Part 1. Transformation of light olefins, Journal of Molecular Catalysis A: Chemical, 144 (1999) 207-220.

[141] Y. Ganjkhanlou, G. Berlier, E. Groppo, E. Borfecchia, S. Bordiga, In Situ Investigation of the Deactivation Mechanism in Ni-ZSM5 During Ethylene Oligomerization, Top. Catal., 60 (2017) 1664-1672.

[142] J. Butt, Activation, deactivation, and poisoning of catalysts, Elsevier, San Diego, 2012.

[143] R.M. Hanson, Introduction to molecular thermodynamics, University Science Books, Sausalito, 2008.

[144] S. Moussa, M.A. Arribas, P. Concepción, A. Martínez, Heterogeneous oligomerization of ethylene to liquids on bifunctional Ni-based catalysts: The influence of support properties on nickel speciation and catalytic performance, Catal. Today, 277 (2016) 78-88.

[145] R. Joshi, G. Zhang, J.T. Miller, R. Gounder, Evidence for the Coordination–Insertion Mechanism of Ethene Dimerization at Nickel Cations Exchanged onto Beta Molecular Sieves, ACS Catal., 8 (2018) 11407-11422.

[146] L. Fan, A. Krzywicki, A. Somogyvari, T. Ziegler, Theoretical Study of Ethylene Oligomerization by an Organometallic Nickel Catalyst, Inorganic Chemistry, 35 (1996) 4003-4006.

[147] H.B. Gray, C.J. Ballhausen, A Molecular Orbital Theory for Square Planar Metal Complexes, J. Am. Chem. Soc., 85 (1963) 260-265.

[148] H.B. Gray, Molecular orbital theory for transition metal complexes, Journal of Chemical Education, 41 (1964) 2.

[149] A.N. Mlinar, O.C. Ho, G.G. Bong, A.T. Bell, The Effect of Noncatalytic Cations on the Activity and Selectivity of Nickel-Exchanged X Zeolites for Propene Oligomerization, ChemCatChem, 5 (2013) 3139-3147.

[150] R. Gounder, E. Iglesia, Catalytic hydrogenation of alkenes on acidic zeolites: Mechanistic connections to monomolecular alkane dehydrogenation reactions, J. Catal., 277 (2011) 36-45.

[151] N.A. Bhore, M.T. Klein, K.B. Bischoff, The delplot technique: a new method for reaction pathway analysis, Ind. Eng. Chem. Res., 29 (1990) 313-316.

[152] M. Iwamoto, One step formation of propene from ethene or ethanol through metathesis on nickel ion-loaded silica, Molecules, 16 (2011) 7844-7863.

[153] A.A. Gabrienko, S.S. Arzumanov, A.V. Toktarev, I.G. Danilova, D. Freude, A.G. Stepanov, H/D exchange of molecular hydrogen with Brønsted acid sites of Zn- and Ga-modified zeolite BEA, Phys. Chem. Chem. Phys., 12 (2010) 5149-5155.

[154] E.A. Pidko, E.J.M. Hensen, R.A. van Santen, Dehydrogenation of Light Alkanes over Isolated Gallyl Ions in Ga/ZSM-5 Zeolites, J. Phys. Chem. C, 111 (2007) 13068-13075.

[155] J.-M. Basset, C. Coperet, D. Soulivong, M. Taoufik, J.T. Cazat, Metathesis of alkanes and related reactions, Acc. Chem. Res., 43 (2009) 323-334.

[156] C. Copéret, D.P. Estes, K. Larmier, K. Searles, Isolated Surface Hydrides: Formation, Structure, and Reactivity, Chem. Rev., 116 (2016) 8463-8505.

[157] J.R. Regalbuto, Electrostatic Adsorption, in: K.P. De Jong (Ed.) Synthesis of solid catalysts, John Wiley & Sons, 2009, pp. 33-57.

[158] A.B. Getsoian, U. Das, J. Camacho-Bunquin, G. Zhang, J.R. Gallagher, B. Hu, S. Cheah, J.A. Schaidle, D.A. Ruddy, J.E. Hensley, T.R. Krause, L.A. Curtiss, J.T. Miller, A.S. Hock, Organometallic model complexes elucidate the active gallium species in alkane dehydrogenation catalysts based on ligand effects in Ga K-edge XANES, Catal. Sci. Technol., 6 (2016) 6339-6353.

[159] V.F. Kispersky, A.J. Kropf, F.H. Ribeiro, J.T. Miller, Low absorption vitreous carbon reactors for operandoXAS: a case study on Cu/Zeolites for selective catalytic reduction of NOx by NH3, Phys. Chem. Chem. Phys., 14 (2012) 2229-2238.

[160] S.A. Bates, A.A. Verma, C. Paolucci, A.A. Parekh, T. Anggara, A. Yezerets, W.F. Schneider, J.T. Miller, W.N. Delgass, F.H. Ribeiro, Identification of the active Cu site in standard selective catalytic reduction with ammonia on Cu-SSZ-13, J. Catal., 312 (2014) 87-97.

[161] V.B. Kazansky, A.I. Serykh, Unusual localization of zinc cations in MFI zeolites modified by different ways of preparation, Phys. Chem. Chem. Phys., 6 (2004) 3760-3764.

[162] V.B. Kazansky, A.I. Serykh, B.G. Anderson, R.A. van Santen, The Sites of Molecular and Dissociative Hydrogen Adsorption in High-Silica Zeolites Modified with Zinc Ions. III DRIFT Study of H2 Adsorption by the Zeolites with Different Zinc Content and Si/Al Ratios in the Framework, Catal. Lett., 88 (2003) 211-217.

[163] A. Ehrmaier, S. Peitz, M. Sanchez-Sanchez, R. Bermejo de Val, J. Lercher, On the role of co-cations in nickel exchanged LTA zeolite for butene dimerization, Microporous Mesoporous Mater., (2019).

[164] N.A. Eberhardt, H. Guan, Nickel Hydride Complexes, Chem. Rev., 116 (2016) 8373-8426.

[165] A. Jentys, G. Warecka, M. Derewinski, J.A. Lercher, Adsorption of water on ZSM 5 zeolites, J. Phys. Chem., 93 (1989) 4837-4843.

[166] I.A. Beta, H. Bohlig, B. Hunger, Structure of adsorption complexes of water in zeolites of different types studied by infrared spectroscopy and inelastic neutron scattering, Phys. Chem. Chem. Phys., 6 (2004) 1975-1981.

[167] B. Hu, A. “Bean” Getsoian, N.M. Schweitzer, U. Das, H. Kim, J. Niklas, O. Poluektov, L.A. Curtiss, P.C. Stair, J.T. Miller, A.S. Hock, Selective propane dehydrogenation with single-site CoII on SiO2 by a non-redox mechanism, J. Catal., 322 (2015) 24-37.

[168] V.J. Cybulskis, S.U. Pradhan, J.J. Lovón-Quintana, A.S. Hock, B. Hu, G. Zhang, W.N. Delgass, F.H. Ribeiro, J.T. Miller, The Nature of the Isolated Gallium Active Center for Propane Dehydrogenation on Ga/SiO2, Catal. Lett., 147 (2017) 1252-1262.